



Thèse

2019

Open Access

This version of the publication is provided by the author(s) and made available in accordance with the copyright holder(s).

The black hole spin in coalescing binary black holes and high-mass X-ray binaries

Qin, Ying

How to cite

QIN, Ying. The black hole spin in coalescing binary black holes and high-mass X-ray binaries. 2019. doi: 10.13097/archive-ouverte/unige:121527

This publication URL: <https://archive-ouverte.unige.ch//unige:121527>

Publication DOI: [10.13097/archive-ouverte/unige:121527](https://doi.org/10.13097/archive-ouverte/unige:121527)

The black hole spin in coalescing binary black holes and high-mass X-ray binaries

THÈSE

présentée à la Faculté des sciences de l'Université de Genève
pour obtenir le grade de Docteur ès sciences,
mention astronomie et astrophysique

par

Ying Qin

de

CHINE

Thèse N° 5348

GENÈVE

Observatoire Astronomique de l'Université de Genève

2019

Résumé

Les trous noirs de masses stellaires se forment par l'effondrement gravitationnel d'étoiles massives ($\geq 20 M_{\odot}$) lorsque ces étoiles ont épuisé leur carburant nucléaire en leur centre. Actuellement, 10 fusions de trous noirs binaires ont été détectées par l'Advanced Laser Interferometer Gravitational-Wave Observatory (AdLIGO). Une nouvelle fenêtre a ainsi été ouverte pour l'étude directe des trous noirs. L'objectif de cette thèse est d'étudier la structure interne et l'évolution binaire, en particulier l'évolution du moment cinétique, des précurseurs des trous noirs, en tenant compte des vents stellaires, de la rotation différentielle, des interactions de marée avec le compagnon, et des transferts de masse par débordement du lobe de Roche de l'étoile donneuse. Les différents aspects du travail sont présentés comme suit. Le Chapitre 1 contient une brève introduction, couvrant le mélange des éléments chimiques et le transport du moment cinétique, l'évolution des étoiles massives appartenant aux systèmes binaires rapprochés et des précurseurs des trous noirs binaires.

Le Chapitre 2 décrit en détails le calcul du coefficient de marée E_2 . Les expressions généralement utilisées pour E_2 sont valables uniquement pour des étoiles de séquence principale d'âge zéro et métallicité solaire. Dans ce chapitre, le calcul de E_2 est décrit pour différents stades évolutifs et différentes métallicités, en particulier pour les étoiles riches en hydrogène et celles riches en hélium.

Le Chapitre 3 introduit le spin du trou noir secondaire lors de la fusion de trous noirs. Différents canaux de formation de trous noirs binaires ont été proposés depuis la première détection d'ondes gravitationnelles (GW150914) par AdLIGO. Le précurseur direct de cette paire de trous noirs est un système binaire rapproché composé d'un trou noir et d'une étoile d'hélium, ce qui est compatible avec le scénario classique d'évolution enveloppe commune, aussi bien qu'avec le scénario d'évolution homogène de binaires massives rapprochées. Le spin du trou noir primaire lors de l'évolution avec enveloppe commune est négligeable, et c'est donc celui du trou noir secondaire qui domine le spin effectif χ_{eff} mesuré lors de la fusion des trous noirs. Nous obtenons que les forces de marées ne deviennent significatives que lorsque les périodes orbitales sont plus courtes que 2 jours. Lors de l'effondrement du cœur, les étoiles d'hélium produisent un trou noir dont le spin peut varier entre 0 et la valeur critique. Nous montrons que la distribution bimodale des spins de trous noirs secondaires obtenus dans des études récentes est essentiellement due à des simplifications excessives. Avec notre approche, nous obtenons une anti-corrélation entre le temps de fusion des

deux trous noirs et le spin effectif χ_{eff} .

Le Chapitre 4 concerne l'origine du spin des trous noirs appartenant des systme binaires massifs rayons X (HMXBs). Nous avons explor deux scnarios possibles pour expliquer le spin lev de ces trous noirs: le scnario de transfert de masse durant la squence principale (Case-A MT), ainsi que le scnario d'volution homogne. Nous obtenons que les deux scnarios sont viables condition que le transport interne de moment cintique dans le progniteur du trou noir aprs la squence principale soit suffisamment faible (i.e. faible couplage coeur-enveloppe). Le premier scnario ne reproduit pas seulement le spin du trou noir, mais aussi les masses des deux compagnons et leur priode orbitale finale. En revanche, le second scnario prdit des priodes orbitales trop longues. De plus, nos rsultats indiquent que le compagnon stellaire d'un HMXB form selon le premier scnario possde un excs d'azote en surface, ce qui peut tre test par des observations futures.

Le Chapitre 5 tudie les conditions pour l'volution homogne. Bien que ce scnario soit invoqu comme canal de formation pour les trous noirs binaires, les conditions pour une telle volution sont peu connues. Dans ce travail, nous cherchons dterminer quelles masses initiales et quelles vitesses de rotations permettent une volution homogne. Cette partie du travail est encore en cours.

Le Chapitre 6 rsume le contenu de la presente thse, et explore les pistes futures ouvertes par le dveloppement des dtecteurs d'ondes gravitationnelles. c Current survey shows that most massive stars are in close binary systems. Stellar-mass black holes (BHs) are formed from the gravitational collapse of massive stars ($\geq 20 M_{\odot}$) after they exhaust the nuclear fuel at their centers. To date, 10 pairs of binary BH mergers have been detected by the Advanced Laser Interferometer Gravitational-Wave Observatory (AdLIGO). Now a new window has been opened to directly study BHs. In this thesis, my work is focused on detailed stellar structure and binary evolution, especially tracking the evolution of angular momentum of the BH progenitor star by taking into account the stellar winds, differential rotation, tidal interaction with its companion, and mass transfer through Roche-lobe overflow of donor star. Main studies in this thesis are presented as follows. Chapter 1 shows a brief introduction, which contains chemical mixing and angular momentum transport, massive stars in close binaries, as well as progenitors of merging stellar-mass BHs.

Chapter 2 describes the detailed calculation of tidal torque coefficient (E_2). Since the widely used expressions for E_2 are valid only for zero-age main sequence (ZAMS) stellar models at solar metallicity. In this part, I describe the detailed calculation of the tidal coefficient E_2 for different evolutionary stages of the stars at different metallicities. New E_2 coefficients have been obtained for both H-rich and He-rich stars. We provided new prescriptions for the tidal coefficient E_2 for both H-rich and the He-rich stars.

Chapter 3 introduces the spin of the second-born BH in coalescing binary BHs. Various binary black hole formation channels have been proposed since the first gravitational wave event GW150914 was discovered by the

AdLIGO. The immediate progenitor of the binary BH is a close binary system composed of a BH and a helium star, which can be the outcome of the classical isolated binary evolution through the common envelope, or alternatively of the massive close binary evolution through chemically homogeneous channel.

We argued that the natal spin of the first-born black hole through the common envelope scenario is negligible ($\lesssim 0.1$), and therefore the second-born BH's spin dominates the measured effective spin, χ_{eff} , from gravitational wave events of double BH mergers. We found that tides can be only important when orbital periods are shorter than 2 days. Upon core collapse, the helium star produces a BH (the second-born black hole in the system) with a spin that can span the entire range from zero to maximally spinning. We showed that the bimodal distribution of the spin of the second-born BH obtained in recent papers is mainly due to oversimplifying assumptions. We found an anti-correlation between the merging timescale of the two black holes, T_{merger} , and the effective spin χ_{eff} .

Chapter 4 presents the origin of BH spin in HMXBs. We explored two possible scenarios to explain the high spins of BHs in the HMXBs, formation in binaries that undergo mass transfer during the main sequence (Case-A MT), alternatively formation in very close binaries undergoing CHE. We found that the two scenarios are able to produce high-spin BHs if internal angular momentum transport inside the BH progenitor star after its main-sequence evolution is not efficient (i.e., weak coupling between the stellar core and its envelope). The former scenario (i.e., Case-A MT) can not only reproduce consistent results for currently high BH spin, but also provides a good fit for the masses of the two components, as well as the final orbital periods. The other scenario (i.e., CHE) predicts orbital periods that are too large for all three sources. Furthermore, we predicted that the stellar companions of HMXBs formed through the Case-A MT have enhanced nitrogen surface abundances, which can be tested by future observations.

Chapter 5 shows the condition of the chemically homogeneous evolution. The CHE has been considered one of the main formation channels for double BHs, however, the conditions for massive stars evolving chemically homogeneously are still poorly understood. In this work, we study the CHE by investigating different physics processes and various initial conditions (initial masses and initial rotation rates). This work is still in preparation.

Chapter 6 presents a summary of this thesis and a short prospect with a focus on the currently operating GW detectors and others that are underway.

Acknowledgements

First of all, I would like to appreciate the contributions from many people who have helped me make this thesis real, especially my two supervisors, Prof. Tassos Fragos and Prof. Georges Meynet.

Tassos is the person who for the first time leads me to the field of astrophysics. At the beginning of my PhD study, I was not well prepared to carry out my PhD project because I did not have enough background on the topic of PhD program. At the very beginning of my PhD project, Tassos prepared me with some small projects that led me to gradually master some basic knowledge of detailed binary evolution. Although I was a bit slower when compared with other PhD students, Tassos was so patient and always supportive throughout my PhD study. I enjoyed working with Tassos for his scientific advice, availability and patience.

As my co-supervisor, Georges also contributed so much time and many efforts to my PhD project. Georges is very patient and glad to answer any questions I would ask, which is of great importance to broaden my horizon and build up my confidence. Georges is an easy-going person and your lovely smile is embedded in my mind. I feel so lucky to have such precious chance to work with him.

In addition to my two supervisors, I would like to thank some advanced researchers from the stellar group, such as André Maeder, Patrick Eggenberger, Sylvia Ekström, Cyril Georgy, Fabio Barblan, Corinne Charbonnel, Laurent Eyer, Nami Mowlavi, Berry Holl, Buldgen Gaël, Gözde Saral and so on. I would also thank Lionel Haemmerlé who helped me with the translation of this thesis resume into French. I also enjoyed the coffee break time with some PhD students at Geneva Observatory, especially Mads Sørensen, Arthur Choplin, and Lingsong Ge.

In the stellar group, I enjoyed the time I had together with Thibaut Dumont, Sébastien Martinet, and Camilla Pezzotti. In the binary group led by my supervisor Prof. Tassos Fragos, I would also love to thank Simone Bavera, Devina Misra, and Emmanouil Zapartas who helped me with my thesis presentation and job interview. At the beginning of my PhD study, I followed the courses, *Des étoiles aux galaxies : propriétés observables et diagnostics spectroscopiques* given by Prof. Daniel Schaerer, *Structure et évolution des galaxies* given by Prof. Daniel Pfenniger, and *Structure interne des étoiles* presented by Prof. Georges Meynet. All of your contributions helped me accumulate more knowledge related to my PhD project and widen my horizon. In addition, I would like to thank Pascal Oesch as my “contact” person outside of my group throughout my PhD study. All of the people at

the Geneva Observatory are so friendly and I love the atmosphere. More specifically, I would like to thank Livia Schnell-Schnyder and Myriam Burgener Frick who both helped me with all kinds of relevant paperwork.

For people outside of Geneva Observatory, I wish to thank Prof. Vicky Kalogera who hosted me for two visits to Northwestern University. Furthermore, I would like to thank my co-authors, such as Jeff Andrews, Mads Sørensen, Hanfeng Song, and especially Pablo Marchant as one of my main collaborators. Pablo Marchant is a diligent researcher who put a lot of efforts into our project. I really appreciate your contributions.

Last but not least, I would like to say thanks to my parents, brothers and my sister, who gave me continuous supports during my study abroad. In addition, I really appreciate the help from Huanyuan Shan, Xi Zhang, as well as their little girl nuomin Shan, as I was treated as part of their family when I first came to Geneva without any relatives and close friends.

Contents

1	Introduction	1
1.1	Chemical Mixing and Angular Momentum Transport	3
1.1.1	Eddington-Sweet circulation	4
1.1.2	Taylor-Spruit dynamo	5
1.2	Massive Stars in Binary Systems	8
1.3	Main Physics of Close Binaries	10
1.3.1	Tidal forces	10
1.3.2	Mass transfer	12
1.4	X-Ray Binaries	18
1.4.1	High-mass X-Ray Binaries	20
1.4.2	Low-mass X-Ray Binaries and Intermediate-mass X-Ray Binaries	20
1.4.3	Measurements of BH spins	26
1.5	Progenitors of Merging Stellar-Mass Black Holes	35
1.5.1	Observational results of the first GW event: GW150914	35
1.5.2	Formation channels of merging stellar-mass black holes	36
1.6	This Thesis	44
1.6.1	Calculation of tidal coefficient E_2	44
1.6.2	The spin of the second-born black hole in coalescing binary black holes	44
1.6.3	On the origin of the black hole spin in High-mass X-ray Binaries	44
1.6.4	On the conditions of CHE	45
2	Calculation of tidal torque coefficient E_2	46
2.1	Introduction of the tidal torque coefficient	46
2.2	Expression of the tidal torque coefficient	47
2.3	Solution for X and Y	48

2.3.1	Boundary conditions for X	48
2.3.2	Boundary conditions for Y	48
2.4	Results of E_2	49
2.5	Conclusion	51
3	The spin of the second-born black hole in coalescing binary black holes	55
3.1	Introduction	55
3.2	The spin of the first-born BH in the classical isolated binary evolution channel	58
3.3	Tidal interaction in binary systems	62
3.3.1	Equilibrium tides	62
3.3.2	Dynamical tides	62
3.4	Testing the efficiency of the tides in WR-BH binary systems	64
3.5	Rotation of the second-born black hole	67
3.5.1	Dependence of orbital evolution and He-star rotation on different binary properties	68
3.5.2	Mass loss enhanced by rotation	76
3.5.3	Systems with mass transfer	76
3.5.4	The Darwin instability	76
3.5.5	The long gamma ray bursts	77
3.6	Merging timescales and comparisons with observed merging systems	77
3.7	Discussion	83
3.8	Conclusions	85
4	On the Origin of Black Hole Spin in High-mass X-Ray Binaries	88
4.1	Introduction	88
4.2	Methods	90
4.3	Results	91
4.3.1	Spin of BHs formed by the Case-A MT or the CHE	91
4.3.2	Impact of the initial orbital period and primary mass on the various outcomes	94
4.3.3	Enhancements of the nitrogen surface abundance via the Case-A MT channel	97
4.4	Comparison with observations	97
4.5	Conclusions	99

5	On the Conditions of Chemically Homogeneous Evolution	102
5.1	Introduction	102
5.2	Comparison of non-rotating models	103
5.3	Comparison of the CHE for rotating models	103
5.3.1	MESA models	104
5.3.2	GENEVA models	105
5.4	Main results and discussions	106
5.5	Appendix: Convergence test of Eddington-Sweet Circulation	107
6	Conclusion and Prospect	114
6.1	Conclusion	114
6.1.1	The spin of the second-born BH in coalescing binary BHs	114
6.1.2	The BH spin of the High-Mass X-Ray Binaries	116
6.1.3	On the Conditions of Chemically Homogeneous Evolution	116
6.2	Prospect	117

Chapter 1

Introduction

Stars with masses larger than 8 times that of our Sun are massive stars. They burn their nuclear fuel much faster than low-mass stars, and at the end of the evolution they may produce one of the most spectacular phenomena that can be observed in the sky: supernova (SN) explosions. They are the progenitors of compact objects (COs), neutron stars (NSs) and black holes (BHs). Massive stars have also been considered to be progenitors of long gamma ray bursts. They have a significant impact on their surrounding environment via strong stellar winds throughout the whole evolution and violent explosion at the end of their lives. They are the most important sources of ionizing photons and the main producers of chemical elements.

When rotation is high enough, it may induce a very strong internal mixing of the chemical elements inside the star, making it to evolve homogeneously (Maeder, 1987). When massive stars are larger than about $20 M_{\odot}$ (M_{\odot} is the mass of our Sun), they exhaust their nuclear fuel in the center and then collapse to form stellar-mass BHs (e.g., Fryer, 1999; Heger et al., 2003; Georgy et al., 2009; Belczynski et al., 2010; Sukhbold et al., 2016). Astrophysical BHs can be fully described by two parameters: their mass, M , and spin angular momentum (AM) \vec{J} . Since the light can not escape from the BH's intense gravitational pull, it is impossible to directly study their properties. X-ray binaries (XRBs) are a class of binary stellar systems containing either a NS or a BH, accreting material from a non-compact companion (donor) star. XRBs are considered to be an ideal environment to indirectly measure BH's properties (Reynolds, 2014; McClintock, Narayan, & Steiner, 2014; Miller & Miller, 2015).

XRBs are often divided into High-mass X-ray Binaries (HMXBs) and Low-mass X-ray (LMXBs) according to the mass of the donor star. While in LMXBs the donor star overfills its Roche lobe, transferring mass to the compact object (CO) through the first Lagrangian point, HMXBs are most often wind-fed systems, where the CO is capturing and accreting part of the strong stellar wind of its massive donor star.

Up to a few years ago, XRBs have been the only astrophysical systems where one could study stellar-mass BHs. However, since the first gravitational wave (GW) event GW150914 was discovered by the Advanced Laser Interferometer Gravitational-Wave Observatory (AdLIGO), a completely new window has been opened to directly

study the properties of BHs and their formation processes.

Theoretically, a lot of progress that is related to massive stellar evolution and detailed binary evolution has been made. More specifically, some important physics, such as, magnetic field and differential rotation inside the star, tidal interaction and mass transfer (MT), has been implemented into the detailed 1D binary evolution codes, for example, Modules for Experiments in Stellar Astrophysics (**MESA**), which is the main tool for our current studies here.

In this introduction, I briefly introduce in §1.1 chemical mixing and angular momentum transport. I then present the current results of observations for massive stars in binary systems in §1.2. In §1.3, main physics of close binaries are briefly shown. Furthermore, I give an introduction of X-ray binaries in §1.4. Then in §1.5, I briefly describe progenitors of merging stellar-mass BHs. Finally, a short summary of this thesis is presented in §1.6.

1.1 Chemical Mixing and Angular Momentum Transport

The evolutionary histories of rotating stars can be significantly changed when compared to those of non-rotating stars. When a star rotates, it will be deformed and can not simultaneously be in thermal and hydrostatic equilibrium (von Zeipel, 1924a). Rotation induce various kinds of instabilities, i.e, meridional (Eddington-Sweet) circulation, Solberg-Høiland instability, Goldreich–Schubert–Fricke instability, secular as well as dynamical shear mixing. The variations as a function of the enclosed mass of the angular velocity, of the specific angular momentum and of various diffusion coefficients are shown in Fig. 1.1 for a rotating ($V_{eq} = 200 \text{ km/s}$) $15 M_{\odot}$ model at $Z = 0.02$ when half of the hydrogen has been transformed into helium in the centre. In the radiative layers, the chemical mixing is mainly determined by the Eddington-Sweet circulation.

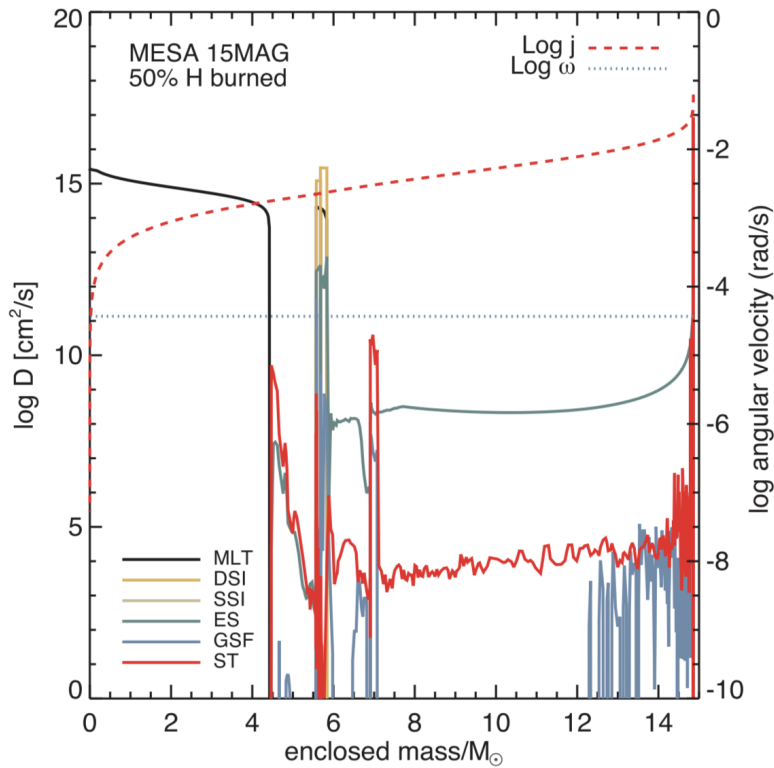


Figure 1.1: Solid lines: Various diffusion coefficients for convection (MLT), Eddington–Sweet (ES) circulation, magnetic torques by ST dynamo (also called TS dynamo that is used later throughout this thesis), dynamical shear instability (DSI), secular shear instability (SSI) and Goldreich–Schubert–Fricke (GSF) instability. Specific AM j (red dashed line) and the angular velocity ω (blue dotted line) are also plotted. This figure is from Paxton et al. (2013).

Chemical mixing due to rotational induced instabilities is treated and implemented (Heger, Langer, & Woosley, 2000) in **MESA** by solving a diffusion equation,

$$\left(\frac{\partial X_n}{\partial t}\right)_m = \left(\frac{\partial}{\partial m}\right)_t \left[(4\pi r^2 \rho)^2 D \left(\frac{\partial X_n}{\partial m}\right)_t \right] + \left(\frac{\partial X_n}{\partial t}\right)_{nuc}, \quad (1.1)$$

where X_n is the mass fraction of species n , and the second term on the right-hand side represents nuclear reaction. D is the diffusion coefficient defined below, which contains non-rotating contribution from convection and semi-convection, as well as rotationally induced instabilities reduced by a factor f_c ($f_c = 0.046$) that was introduced by Pinsonneault, Kawaler, Sofia, & Demarque (1989) for reproducing the surface abundance ${}^7\text{Li}$ of our Sun. Chaboyer & Zahn (1992) found a similar value ($f_c = 1/30$) for the combined impact of shear and meridional circulation.

$$D = D_{conv} + D_{sem} + f_c \times (D_{DSI} + D_{SHI} + D_{SSI} + D_{ES} + D_{GSF})^1, \quad (1.2)$$

In order to describe the sensitivity of rotationally induced mixing to μ gradients ($\nabla\mu$), a parameter f_μ multiplies the μ gradients $f_\mu \nabla\mu$. The boundary condition at the centre and at the surface are

$$\left(\frac{\partial X_n}{\partial m}\right)_t \Big|_{m=0} = \left(\frac{\partial X_n}{\partial m}\right)_t \Big|_{m=M(t)} = 0. \quad (1.3)$$

Similar to chemical mixing, transport of AM is also treated (Endal & Sofia, 1978; Pinsonneault, Kawaler, Sofia, & Demarque, 1989) as a diffusive process,

$$\left(\frac{\partial \omega}{\partial t}\right)_m = \frac{1}{i} \left(\frac{\partial}{\partial m}\right)_t \left[(4\pi r^2 \rho)^2 i \nu \left(\frac{\partial \omega}{\partial m}\right)_t \right] - \frac{2\omega}{r} \left(\frac{\partial r}{\partial t}\right)_m \left(\frac{1}{2} \frac{d \ln i}{d \ln r}\right), \quad (1.4)$$

where i is the specific AM of one shell, and ν is the turbulent viscosity that is defined as

$$\nu = D_{conv} + D_{sem} + D_{DSI} + D_{SHI} + D_{SSI} + D_{ES} + D_{GSF}^2. \quad (1.5)$$

The last term in Eq. 1.4 is the advection that accounts for contraction or expansion. In radiative layers of a star, a seed magnetic field can be amplified by differential rotation, which is called Tayler-Spruit (TS) dynamo (Spruit, 1999, 2002).

Since detailed implementation was described in Heger, Langer, & Woosley (2000), here I focus on introducing the two rotationally induced effects that are closely relevant to my work, namely the Eddington-Sweet circulation and the TS dynamo. A detailed description of chemical mixing and AM transport is presented in §5.

1.1.1 Eddington-Sweet circulation

The Eddington-Sweet circulation was first found by von Zeipel (von Zeipel, 1924a,b) and then further investigated by Baker & Kippenhahn (1959). The circulation velocity estimated by Kippenhahn (1974) is given as

$$v_e \equiv \frac{\nabla_{ad}}{\delta(\nabla_{ad} - \nabla)} \frac{\omega^2 r^3 l}{(Gm)^2} \left[\frac{2(\varepsilon_n + \varepsilon_\nu) r^2}{l} - \frac{2r^2}{m} - \frac{3}{4\pi\rho r} \right],$$

¹ D_{conv} and D_{sem} are coefficients for convection and semiconvection, D_{DSI} : dynamical shear instability, D_{SHI} : Solberg-Høiland instability, D_{SSI} : secular shear instability, D_{GSF} : Goldreich-Schubert-Fricke instability.

²When the TS dynamo is included, D_{TS} (TS term), is only included for the AM transport.

where l is luminosity, ε_n is the energy released by contraction, and ε_ν is the energy per gram and second due to neutrino emission. Eddington-Sweet circulation is suppressed due to the presence of mean molecular weight μ gradient (Mestel, 1952, 1953) and the corresponding velocity is written as (Heger & Langer, 2000)

$$v_\mu \equiv \frac{H_p}{\tau_{KH}^*} \frac{\varphi f_\mu \nabla_\mu}{\delta(\nabla - \nabla_{ad})}, \quad (1.6)$$

where $\tau_{KH}^* \equiv \frac{Gm^2}{r(l-m\varepsilon_\mu)}$ is the local Kelvin-Helmholtz timescale, f_μ represents the sensitivity of the rotationally induced mixing to μ gradient, i.e., ∇_μ is replaced by $f_\mu \nabla_\mu$ (a value of $f_\mu = 0.1$ has been suggested in Brott et al. 2011). Combining the two velocities above results in the effective velocity (Endal & Sofia, 1978).

$$v_{ES} \equiv \max\{|v_e| - |v_\mu|, 0\}. \quad (1.7)$$

The diffusion coefficient D_{ES} is then calculated as the product of the v_{ES} and a corresponding length scale $H_{\mu,ES}$. This is assumed to be the minimum of the extent d_{inst} of the instability and the velocity scale height,

$$H_{\mu,ES} = \left| \frac{dr}{d \ln v_{ES}} \right|, \quad (1.8)$$

$$D_{ES} \equiv \min\{d_{inst}, H_{\mu,ES}\} v_{ES}, \quad (1.9)$$

where d_{inst} is the instability height for the Eddington-Sweet circulation.

1.1.2 Tayler-Spruit dynamo

AM transport is one of the main longstanding problems in stellar astrophysics. In general, when the star leaves Main Sequence (MS), the envelope expands and slows down, the inner core contracts and spins up. The differential rotation can induce various instabilities which are responsible for AM transport. One of the main instabilities produced in the radiative zones is the TS dynamo that strongly couples the stellar core and its envelope and hence plays a key role in the AM transport.

A few observations for measuring internal stellar rotation rates at different evolutionary stage are available. On the one hand, efficient AM transport similar to TS dynamo seems to be needed to reproduce the flat rotation profile of our Sun (Howe, 2009) as well as the observed slow rotation rate of White Dwarfs (WDs) and NSs (Heger, Woosley, & Spruit, 2005; Suijs et al., 2008). However the TS dynamo cannot reproduce the asteroseismic constraints for sub-giants and red giants (Gehan et al., 2018).

The TS dynamo has been criticized by Zahn, Brun, & Mathis (2007) that concluded that this mechanism was unable to amplify a seed magnetic field. On the other hand, the mechanism was confirmed to be present in numerical simulations made by Braithwaite (2006). The question of the reality of this dynamo mechanism remains so far an

open question. We can however just say that at the moment it appears as a better approach than other theories in the sense that, as indicated above, it provides a solution to the solid body rotation of the Sun and allows to produce not too fast rotating COs.

TS dynamo has been widely used in the stellar evolution community. Fig. 1.2 shows a comparison of rotating models with and without TS dynamo in **MESA**. We can see that during the MS phase the TS dynamo has a small impact on the distribution of the specific AM. However, when the star leaves MS, the stellar core loses a large amount of AM through TS dynamo that is shown in the right panel of Fig. 1.2.

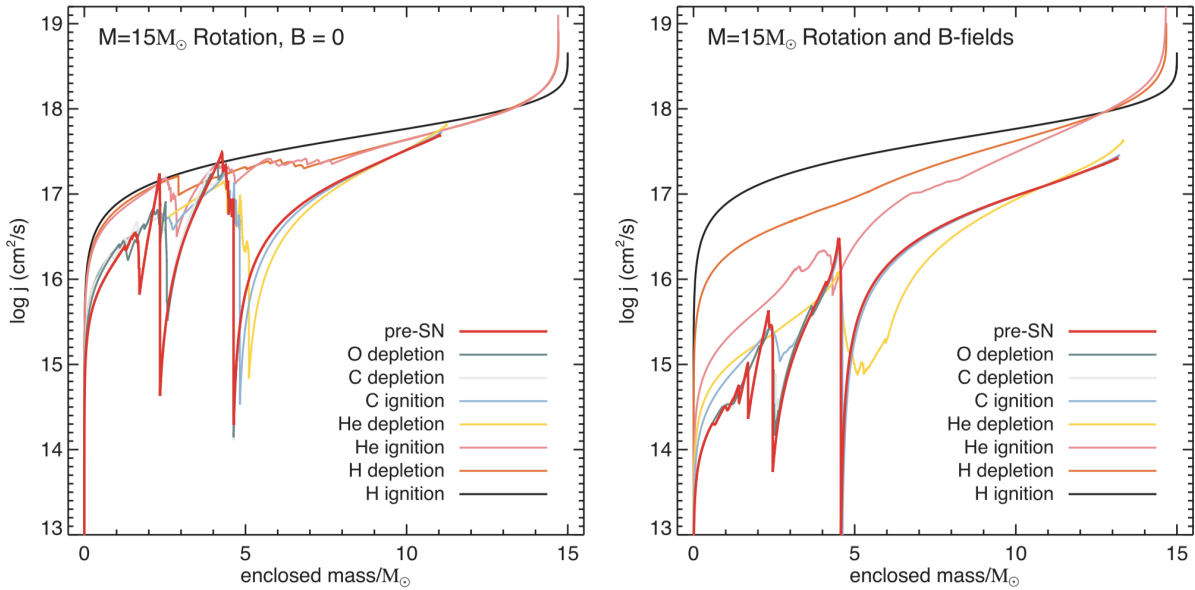


Figure 1.2: Specific angular momentum distribution at various stages in a $15 M_{\odot}$ model with rotation. For comparison, internal magnetic field is included in left panel, and in the right panel no internal magnetic field is taken into account. The initial velocity $v_{init} = 200$ km/s. These figures are from Paxton et al. (2013).

In addition, TS dynamo has also been implemented in **GENEVA** code. Fig. 1.3 shows a comparison between with and without TS dynamo³. It has been found that the results of **GENEVA** code are consistent with those of **MESA** code on the condition that TS dynamo is included.

³No TS dynamo refers to the model in which internal magnetic field is not included.

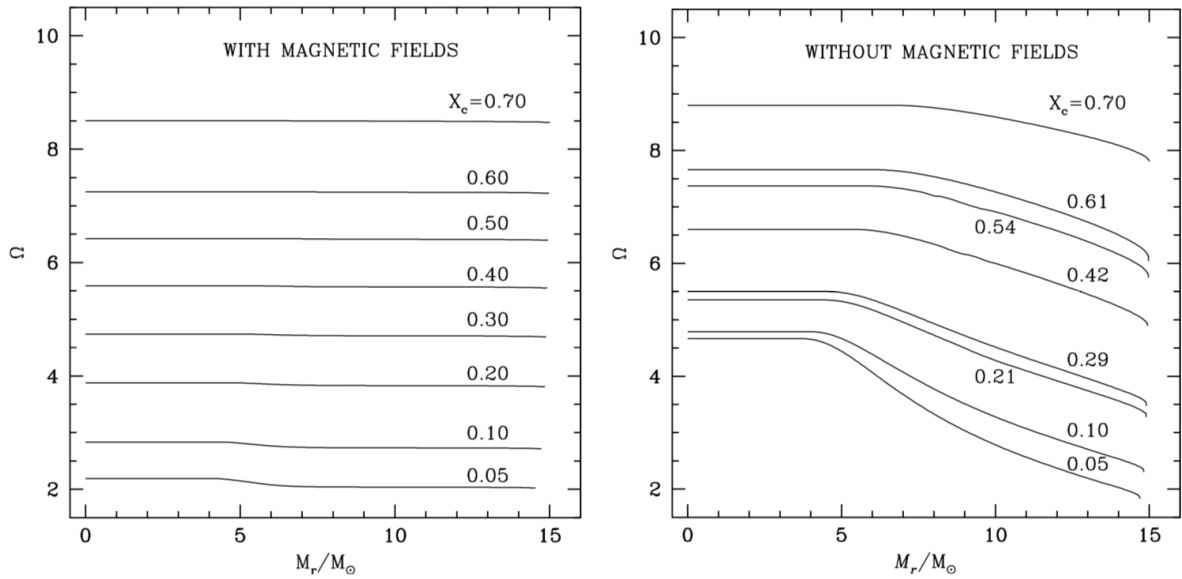


Figure 1.3: Internal distribution of angular velocity as a function of the Lagrangian mass for $15 M_\odot$ with magnetic field (left panel) and without magnetic field (right panel), at various stages indicated by the central hydrogen X_c during the MS phase. The initial velocity $v_{init} = 300$ km/s. This figure is from Maeder & Meynet (2005).

1.2 Massive Stars in Binary Systems

Binary stars are systems in which two stars orbit around the centre of their masses. Binary stars have been considered to be of great importance as they allow in case of eclipsing systems, the determination of the masses of the two components.

the important properties (for example, their masses) of two components to be determined. Fig. 1.4 shows that over $\sim 70\%$ of observed O-type stars in the Milky Way are in close binary systems (Sana et al., 2012), which will be likely to undergo various interactions, i.e., merger (red, $\sim 24\%$), accretion (Orange, $\sim 14\%$), and envelope stripping (yellow, $\sim 33\%$). Similar results have also been found in the Large Magellanic Cloud (Almeida et al., 2017).

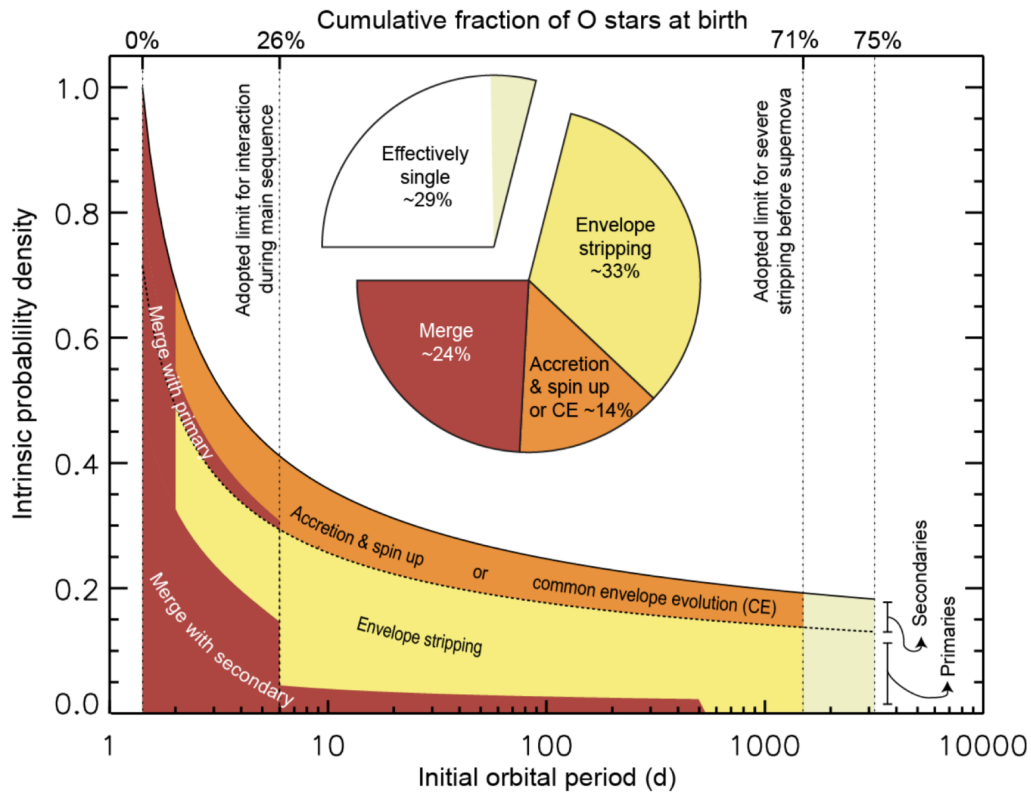


Figure 1.4: Schematic diagram of relative importance for various binary interaction processes with best-fit and intrinsic distribution functions. All percentages are shown in terms of the fraction for all stars born as O-type stars. The solid line represent the best-fit intrinsic distribution of orbital periods, and the dotted lines separate the contributions from O-type primary and secondary stars. The coloured areas show the various fractions of binary systems that are expected to merge (red), undergo stripping (yellow), or accretion & spin up or common envelope (CE) phase. The pie chart represents the fraction of stars born as O-type stars that are single (white, 29%), and others with different binary interactions (71% combined). This figure is from Sana et al. (2012).

The most massive overcontact binary system VFTS352 was found by the VLT-FLAMES Tarantula Survey (Evans et al., 2008). The two $30 M_{\odot}$ stars have an orbital period of around 1.1 days, which are undergoing overcontact phase. Therefore, they will be expected to merger. The interaction of such system is beautifully illustrated (Almeida et al., 2015) in Fig. 1.5.



Figure 1.5: An artist impression of VFTS352, the most massive overcontact binaries known to date (Almeida et al., 2015). Credit: ESO/L. Calçada.

To date theoretical simulations of detailed binary evolution, which mainly contains the physics of different binary interactions (i.e., MT through Roche-lobe overflow, tidal interaction, and overcontact phase), have been already included in **MESA** for further test.

1.3 Main Physics of Close Binaries

As an open source and powerful tool, **MESA** provides a great opportunity to test various physical processes inside the star and interactions between the two components in binary systems. In this section, I briefly introduce the main physical effects occurring in close binary evolution, tidal interaction and mass transfer (MT).

1.3.1 Tidal forces

The existence of tides on the surface of Earth is well known, especially for people who live near an ocean (see Fig. 1.6). However, tidal phenomena are not only limited to the oceans, but can occur in other systems whenever a gravitational field is present. A differential force on an object that has a non-zero size is defined as a tidal force (Carroll & Ostlie, 2006).

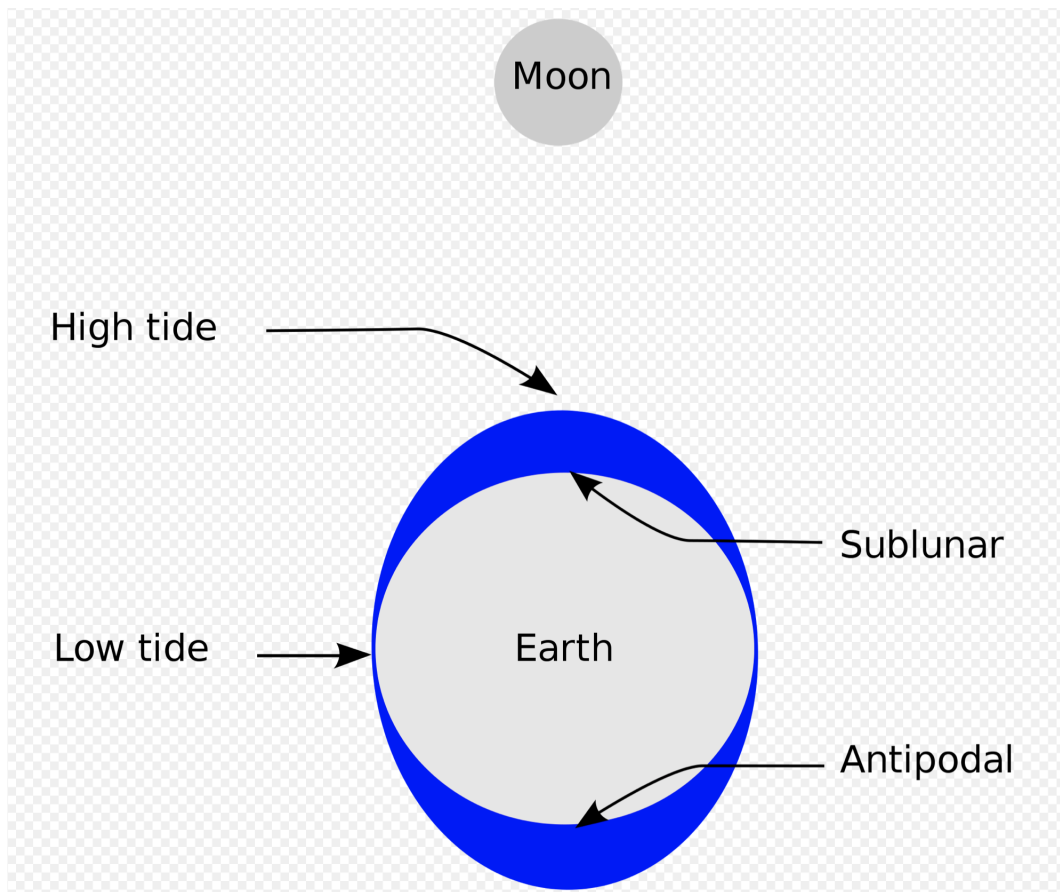


Figure 1.6: Schematic representation of tides on the surface of Earth, showing (exaggerated) high tides at the sublunar point and its antipode. Credit: Wikipedia.

Tides in binary systems are strongly dependent on the separation in comparison with the sizes of the two components. In the Earth-Moon system, AM transfer from Earth's spin to their orbit leads to a lengthening of

the day. The process of deformation due to tidal dissipation involves fluid dynamics and we refer readers to more details in Ogilvie (2014). Tides tend to equalize the spin and orbital angular velocity through an exchange of AM between the spin and orbital angular momentum reservoirs and dissipation of energy.

For a star in a binary system, the tides play a critical role in the evolution throughout its whole life. The theory of the tides for stars in a close binary was first studied by Zahn (1975). To a first approximation (the stellar wind mass loss and the gravitational waves are weak and negligible), two stars in a close binary system conserves their AM while evolving to a state that has a minimum kinetic energy, where two spins are aligned to the direction of orbital AM, the orbit is circular, and two stars rotate in synchronization with the orbit motion. The pace for reaching this final phase depends on the dissipation processes of the tidal kinetic energy.

Two main mechanisms (Zahn, 1975) for this dissipation have been widely accepted. For stars with an outer convection zone, turbulent dissipation (or convective damping) on the equilibrium tides is dominant. For stars with an outer radiative zone, the major dissipative mechanism is radiative damping process operating on the dynamical tides.

In **MESA**, the implementation of tidal interaction is based on the model of Hut (1981) and the differential rotation is included for both stars. The synchronization timescale for each component is

$$\frac{1}{T_{\text{sync},j}} = \frac{3}{(q_j r_{g,j}^2)^2} \left(\frac{k}{T}\right)_j \left(\frac{R_j}{a}\right)^6 \quad \text{and} \quad \frac{d\omega_{i,j}}{dt} = \frac{n - \omega_{i,j}}{T_{\text{sync},j}}, \quad (1.10)$$

where $j = 1, 2$ refers to the index of two stars, $\omega_{i,j}$ is the angular frequency of the shell i at the surface. q is the mass ratio of the two components, $r_{g,j}^2$ is the dimensionless gyration radius of each star. $\left(\frac{k}{T}\right)_j$ is a coupling parameter, which depends on the different mechanisms of the tidal interaction, i.e., dynamical tides and equilibrium tides. Dynamical tides for stars with radiative envelopes and convective core are responsible for the dissipation processes of the tidal kinetic energy. For the calculation of $\Delta\omega_{i,j}$ in each step, the $T_{\text{sync},j}$ and the orbital angular frequency n are assumed to be constant to compute the $\Delta\omega_{i,j}$ (Detmers, Langer, Podsiadlowski, & Izzard, 2008).

1.3.2 Mass transfer

In a binary system with a circular orbit, it is convenient to describe this system in a co-rotating frame. In this non-inertial frame, both centrifugal force and gravity can be described together by a potential. A representation of equipotential contours of a binary system is shown in Fig. 1.7. The Roche potential has 5 Lagrangian points where surface net force is zero.

When a star evolves, it gradually expands to overflow its Roche lobe, the material on its surface flows into its companion via the first Lagrangian point L_1 , which is referred as MT via Roche-lobe overflow.

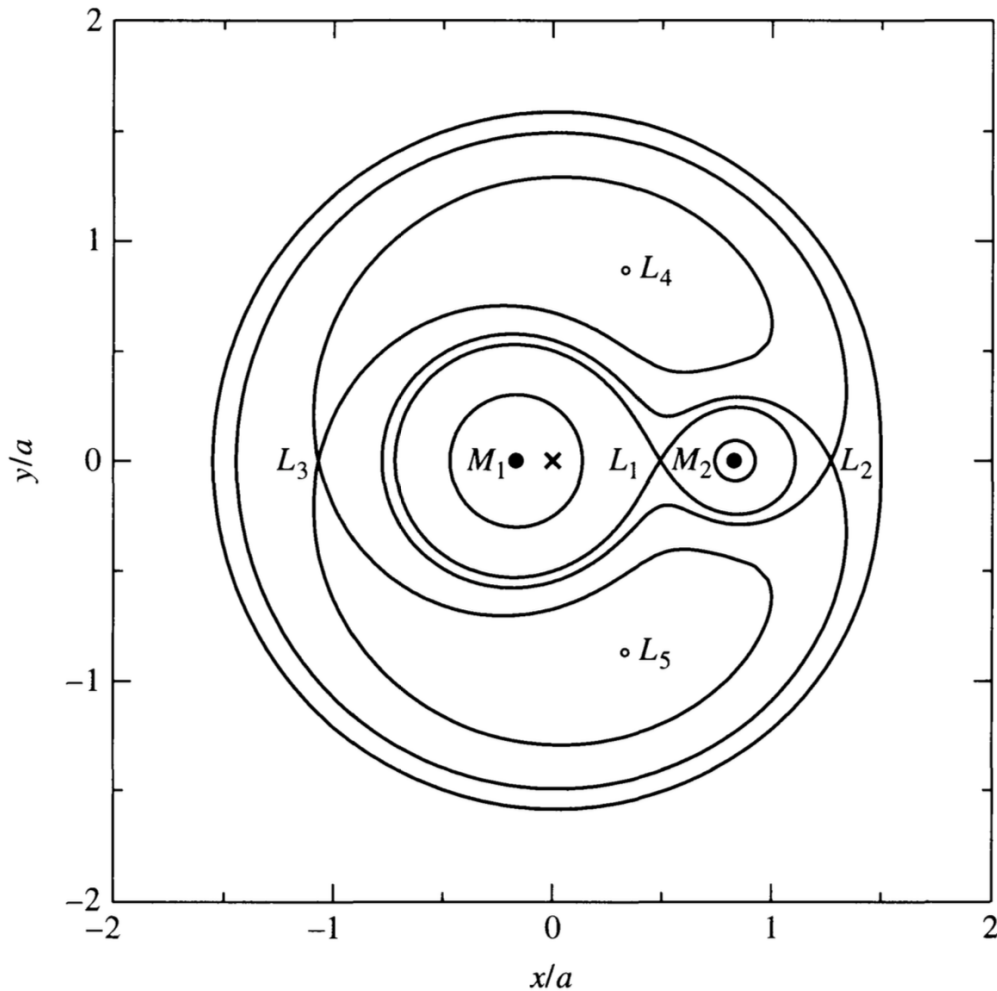


Figure 1.7: Equipotentials of a binary system ($M_1 = 0.85 M_\odot$, $M_2 = 0.17 M_\odot$, and separation $a = 0.718 R_\odot$). Both axes are units of a , cross symbol "x" represents the system's center of mass at the origin. Equipotential curves (in units of $G(M_1 + M_2)/a$) from top toward the center of mass are, -1.875, -1.768, -1.583, -1.583, -1.768 (the "dumbbell"), -1.875 (the Roche lobe), and -3 (the spheres). Five Lagrangian points are marked in the figure. This figure is from Carroll & Ostlie (2006).

The Roche lobe plays a critical role in the description of close binary evolution. Understanding the Roche lobe overflow needs a 3D simulation, however this process is commonly modeled in 1D stellar evolution code. An equivalent radius of the Roche lobe is defined as a radius of a sphere with the same volume, $V_L = \frac{4}{3}\pi R_{RL}^3$. A fitting formula for the Roche lobe radius R_L that is accurate up to better than 1 % for the entire range of mass ratio,

$$R_{L,j} = a \frac{0.49q_j^{2/3}}{0.6q_j^{2/3} + \ln(1 + q_j^{1/3})}, \quad (1.11)$$

where j is the index for each star. MT starts to occur when the radius of the star overflows its Roche lobe.

In the following, I show the stability of MT in terms of mass-radius relationship (Soberman, Phinney, & van den Heuvel, 1997), introduce three main cases of MT, and close by comparing two MT schemes implemented in **MESA**, i.e., explicit and implicit methods.

Stability of mass transfer

As the star loses its mass in a duration shorter than the kelvin-Helmholtz timescale, it leaves the thermal equilibrium. In order to reach such equilibrium, the star naturally adjusts itself by either expanding or contracting on two different timescales, i.e., dynamical timescale and thermal timescale. The stability of MT is evaluated by comparing power-law fits of the donor star's radius to its mass and the radius of star's Roche lobe to the mass, i.e., mass-radius relationship (Soberman, Phinney, & van den Heuvel, 1997), namely

$$R \sim M^\zeta \quad (1.12)$$

, then the exponents for the radius of donor star and its Roche lobe become

$$\zeta_{\text{eq}} = \left(\frac{\partial \ln R_{\text{donor}}}{\partial \ln M_{\text{donor}}} \right)_{\text{eq}}, \quad (1.13)$$

$$\zeta_{\text{ad}} = \left(\frac{\partial \ln R_{\text{donor}}}{\partial \ln M_{\text{donor}}} \right)_{\text{ad}}, \quad (1.14)$$

$$\zeta_{\text{RLOF}} = \left(\frac{\partial \ln R_{\text{RLOF}}}{\partial \ln M_{\text{donor}}} \right)_{\text{RLOF}}. \quad (1.15)$$

ζ_{eq} refers to the response of the donor to its mass loss for the star still in thermal equilibrium. When the donor star loses mass on a timescale shorter than thermal timescale, the corresponding response is given by ζ_{ad} . ζ_{RLOF} indicates the dependency of the Roche lobe radius on MT. The instability criterion of MT is given as follows:

- $\zeta_{\text{eq}} > \zeta_{\text{RLOF}}$: MT is stable, and the donor star remains inside its Roche lobe by transferring mass in thermal equilibrium.

- $\zeta_{\text{ad}} > \zeta_{\text{RLOF}} > \zeta_{\text{eq}}$: MT is still stable. The donor keeps stay inside its Roche lobe, but transfers mass on a thermal timescale.
- $\zeta_{\text{eq}} > \zeta_{\text{RLOF}}$: MT is dynamically unstable. The donor will leave hydrostatic equilibrium and the binary will undergo a CE or contact phase.

Main cases of mass transfer

Based on the variation of the radius of the donor star, MT was classified in three cases (Kippenhahn & Weigert, 1967), i.e., Case A, Case B and Case C. Fig. 1.8 shows an example of a $5 M_{\odot}$ star undergoing three cases of MT.

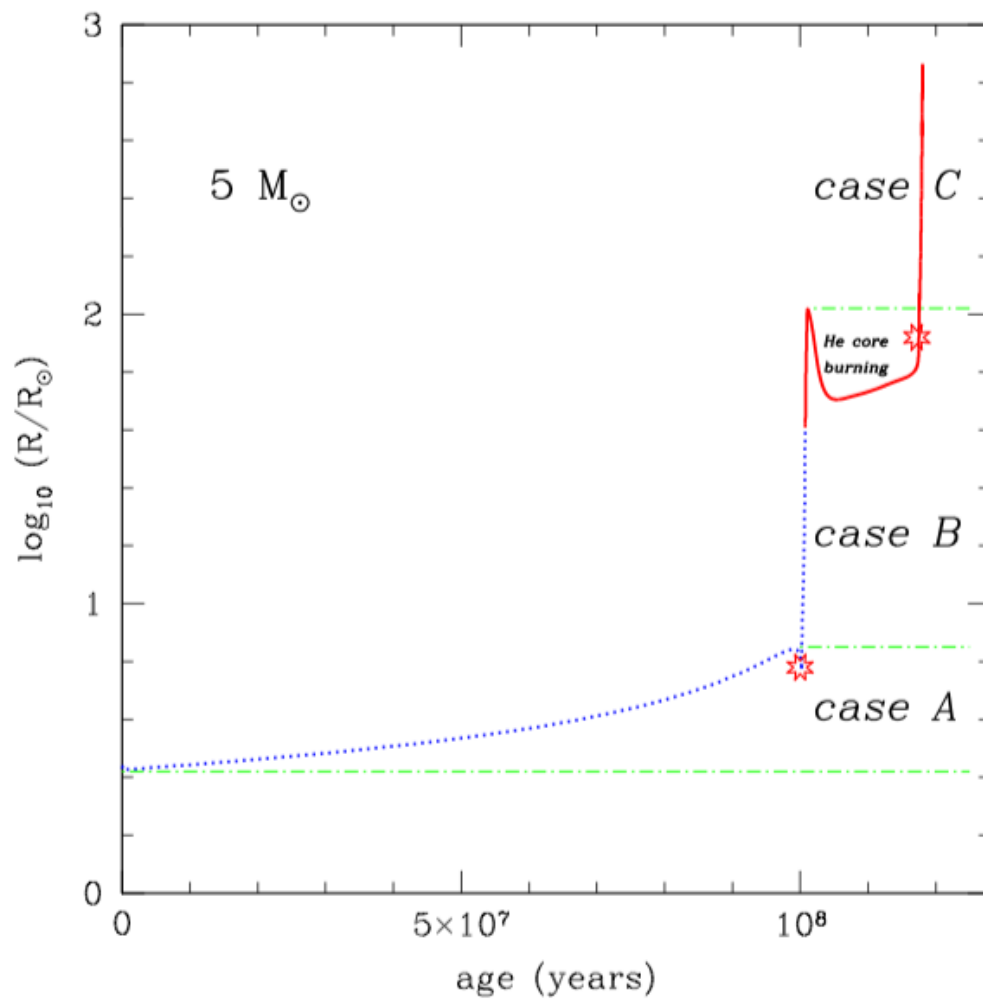


Figure 1.8: Evolution of the radius for a single star at $5 M_{\odot}$. Three phases of MT are marked with corresponding texts (Case A, Case B and Case C). This figure is from Ivanova (2015).

- Case A: The donor star fills its Roche lobe when it is burning hydrogen in the core.

- Case B: MT occurs after central hydrogen burning, but before ignition of central helium burning.
- Case C: MT starts after exhaustion of central helium burning.

Mass transfer from RLOF

There are two possible mechanisms for MT between stars in a binary system, i.e., stellar wind accretion and Roche lobe overflow. The first one occurs when part of the stellar wind from the more massive star is captured by the CO (accretor) in the binary, while the other one refers to MT via the first Lagrangian point L_1 . Here the later one is introduced with two methods for calculating MT rate, i.e., explicit method and implicit method. The explicit method starts with \dot{M}_{RLOF} that is set at the beginning of the step, while for implicit one, a guess for \dot{M}_{RLOF} is initialized and multiple iterations will be made until the required tolerance is reached (Paxton et al., 2015).

- Explicit MT: two schemes, Ritter scheme and Kolb scheme, are described (Paxton et al., 2015) as follows.

– Ritter scheme

In this scheme, stars have extended atmospheres, so MT can take place through the first Lagrangian point (L_1) point even when $R_{\text{donor}} < R_{\text{RLOF}}$ (Ritter, 1988). The MT rate is given below.

$$\dot{M}_{\text{RLOF}} = -\dot{M}_0 \exp\left(\frac{R_{\text{donor}} - R_{\text{RLOF}}}{H_{P,\text{donor}}/\gamma(q_2)}\right), \quad (1.16)$$

where $q_2 = M_2/M_1$, $H_{P,\text{donor}}$ is the pressure scale height at the photosphere of the donor star, and

$$\dot{M}_0 = \frac{2\pi}{\exp(1/2)} F_1(q_2) \frac{R_{\text{RLOF}}^3}{GM_{\text{donor}}} \left(\frac{k_B T_{\text{eff}}}{m_p \mu_{\text{ph}}}\right)^{3/2} \rho_{\text{ph}}, \quad (1.17)$$

where m_p is the proton mass, k_B is the Boltzmann constant, T_{eff} is the effective temperature of the donor star, and ρ_{ph} as well as μ_{ph} is the density and mean molecular weight at the donor star's photosphere, respectively. In addition, the two fitting expressions are given as follows:

$$F_1(q_2) = 1.23 + 0.5 \log q_2, 0.5 \lesssim q_2 \lesssim 10, \quad (1.18)$$

and

$$\gamma(q_2) = \begin{cases} 0.954 + 0.025 \log q_2 - 0.038(\log q_2)^2, & 0.04 \lesssim q_2 \lesssim 1 \\ 0.954 + 0.039 \log q_2 + 0.114(\log q_2)^2, & 1.0 \leq q_2 \lesssim 20 \end{cases} \quad (1.19)$$

At the boundary of the range, $F_1(q_2)$ or $\gamma(q_2)$ are evaluated by the edges of their respective ranges (Paxton et al., 2015).

– Kolb scheme

In this improved approach, the donor star is not necessarily constrained inside its Roche lobe, and the MT rate is given derived on detailed structure of the outer layers of the donor as well as binary parameters. Hence this approach is referred as the optically thick regime. For this case $R_{\text{donor}} > R_{\text{RLOF}}$, Kolb & Ritter (1990) extended the Ritter scheme in order to calculate the MT rate \dot{M}_{RLOF} as

$$\dot{M}_{\text{RLOF}} = -\dot{M}_0 - 2\pi F_1(q_2) \frac{R_{\text{RLOF}}^3}{GM_{\text{donor}}} \times \int_{P_{\text{ph}}}^{P_{\text{RLOF}}} \Gamma_1^{1/2} \left(\frac{2}{\Gamma_1 + 1} \right)^{(\Gamma_1+1)/(2\Gamma_1-2)} \left(\frac{k_B T}{m_p \mu} \right)^{1/2} dP, \quad (1.20)$$

where Γ_1 is the first adiabatic exponent, R_{PH} and P_{RLOF} are the pressure at the photosphere and the radius when $r_1 = R_{\text{RLOF}}$, respectively.

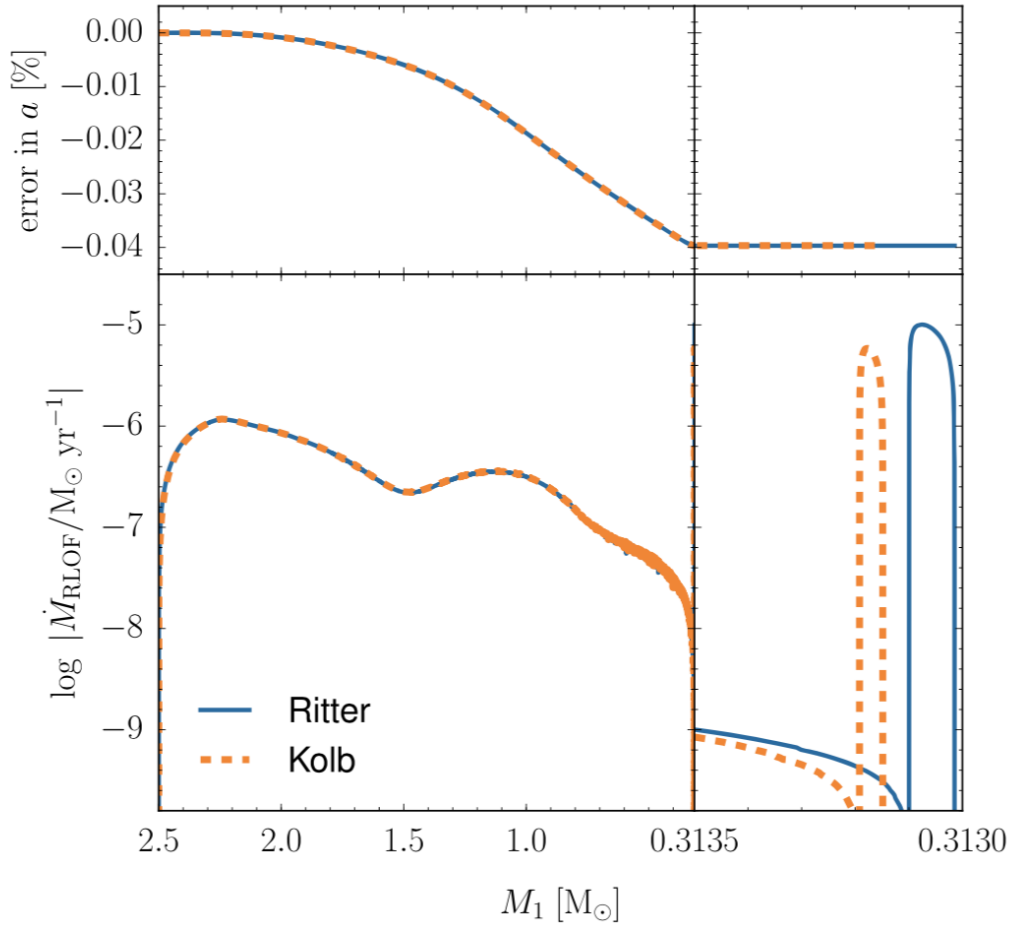


Figure 1.9: Here is the comparison between Ritter and Kolb MT scheme for a $2.5 M_{\odot}$ and $1.4 M_{\odot}$ point mass star. Upper panel: the difference between analytical solution and computed model form **MESA**. Bottom panel: evolution of MT rate of the two schemes. This figure is from Paxton et al. (2015).

In Fig. 1.9, a binary system was run by using the Ritter and Kolb implicit MT scheme. It is clearly shown

that the two schemes can produce a very similar result .

- Implicit MT

In the implicit scheme, **MESA** provides a bisection-based root solve to satisfy $|f(\dot{M}_{\text{donor}})| < \xi$ (Paxton et al., 2015) at the end of each step, where the tolerance ξ is defined as

$$f(\dot{M}_{\text{RLOF}}) = \frac{\dot{M}_{\text{end}} - \dot{M}_{\text{RLOF}}}{\dot{M}_{\text{end}}}, \quad (1.21)$$

where \dot{M}_{end} is the MT rate computed at the end of each iteration. In addition, **MESA** provides an alternative implicit method that allows the donor star to adjust MT rate until $R_{\text{RLOF}} = R_L$ within the tolerance given by

$$f(\dot{M}_{\text{RLOF}}) = \frac{2(R_1 - R_{\text{RLOF}})}{R_{\text{RLOF}}} + \xi. \quad (1.22)$$

In this case, when \dot{M}_{RLOF} decreases below some threshold and $f(\dot{M}_{\text{RLOF}}) < -\xi$, the binary system is assumed to detach and \dot{M}_{RLOF} is then set to zero (Paxton et al., 2015).

1.4 X-Ray Binaries

XRBs have been considered to be ideal objects to study the properties of the compact objects (COs). In Fig. 1.10, I show two typical examples, i.e., one of HMXB and one of LMXB. For the case of HMXB shown on the top panel, the donor star is more massive than in the LMXB case, and only part of its strong high-velocity stellar winds are captured by the accretor. The rest of the material is lost, and thus this MT process is non-conservative. However, for the LMXB case, the donor star is overflowing its Roche lobe, all the materials leaving from the donor are transferred onto the CO through the first Lagrangian point. We have here a case of conservative MT.

In the Milky Way, more than 90% XRBs fall into these two groups. Fig. 1.11 shows the galactic distributions of the HMXBs and LMXBs. The distribution of galactic HMXBs shows an obvious concentration to the galactic center. A statistic study of the kinematic properties of the optically confirmed HMXBs (van Oijen, 1989) shows that they are runaway stars. For galactic LMXBs, its distribution has a wider latitude dispersion, and the study of their kinematic properties indicates that these are among the oldest objects in our Galaxy. In addition to the two groups, when XRBs have a companion star with mass in the interval $1 - 10 M_{\odot}$, they are referred as IMXBs.

XRBs have been considered as ideal laboratories for obtaining the properties of the NSs or BHs. The radial velocity of the companions can be used to determine the lower limit (calculated from binary mass function) of the dynamical mass of the COs. Fig. 1.12 presents currently observed masses of NSs and BHs in XRBs, as well as relevant theoretical explanations. A mass gap was first noted by Bailyn, Jain, Coppi, & Orosz (1998) that there are no observed COs in the mass range $2 - 5 M_{\odot}$. It was found that this gap depends on the growth time of instability (Belczynski et al., 2012). The observed data can be accounted for when the rapid instability (growth time is $10 - 20$ ms) is considered. In this model, they found that an instability develops with the first $\sim 10 - 20$ ms after the bounce and then leads a rapid explosion ($\sim 100 - 200$ ms). However, if the instabilities are strong enough, a delayed explosion ($\sim 500 - 1000$ ms) may follow. In this case, this gap would be filled when significant fallback appears due to slowly growing instabilities (namely the delayed SN model). Now the existence of this gap is still an open question. The physics of the core collapse of massive stars is complex and the links between the characteristic of the progenitors and the properties of the stellar remnants are still to be reliably established.

Another aspect of CO formation that has been recognized as a key element, but is not yet understood from first principles is that of asymmetries associated with the SN explosion and the resulting natal kicks imparted to COs.

Observational evidence since the 70's primarily based on the kinematics of radio pulsar populations (Zou et al., 2005) strongly suggest that NSs acquire very significant natal kicks of the order of a few to a several hundreds of km/s. Studies of the NS binary systems (Pfahl, Rappaport, Podsiadlowski, & Spruit, 2002) imply that a subset of NS acquire smaller kicks ($10-100$ km/s) (Janssen et al., 2008). These COs are believed to be formed from through electron-capture instead of Fe core-collapse. Simulations from Janka et al. (2007) support natal kick of larger than

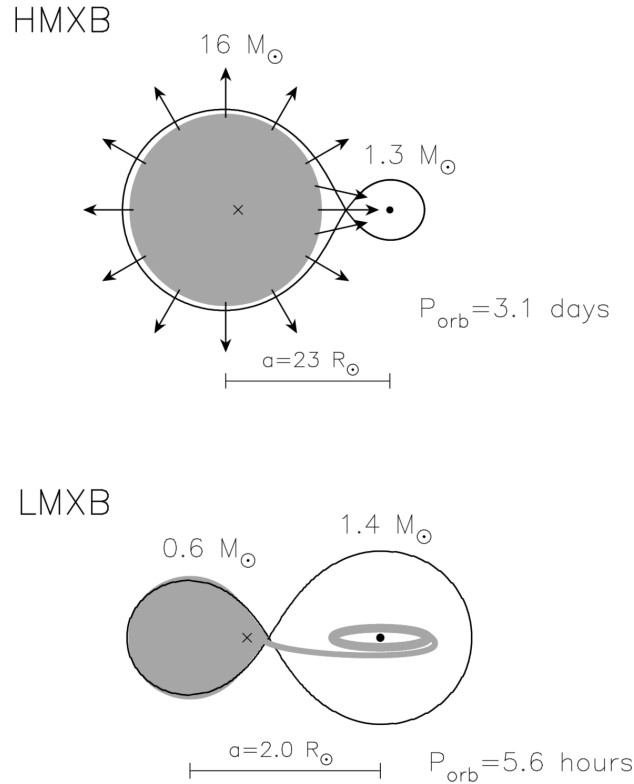


Figure 1.10: Two typical examples of HMXB (top panel) and LMXB (bottom). The NS in HMXB is fed by strong mass-loss winds while for LMXB the NS is accreting mass from its companion via Roche-lobe overflow. This figure is from Tauris & van den Heuvel (2006).

~ 100 km/s and this is a strong evidence for the asymmetric SN explosion. Compared to NS, relevant evidence for BHs is very rare (Repetto, Davies, & Sigurdsson, 2012). Natal kicks play a significant role in understanding the process of BH formation: if BH kicks are ubiquitous then their formation must be closely associated to that of NS before the BH horizon is formed; if BH kicks are required just for some BH then formation through more than one physical process will be favored.

For the Galactic XRB XTE J1118+480, an asymmetric natal kick is currently required to explain its formation (Fragos et al., 2009). It is still in debate that for GRO J1655-40 (Willems et al., 2005) the kick is necessarily required to explain this formation. While studies of Cyg X-1 indicates an upper limit kick (< 77 km/s; e.g., Wong, Valsecchi, Fragos, & Kalogera, 2012) is needed to understand its evolutionary history. Besides, other similar work has also been done for XRBs outside of our Galaxy, i.e., M33 X-7 (Valsecchi et al., 2010), IC10 X-1 (Wong et al., 2014), and LMC X-1 (Sørensen et al., 2017).

The spatial motion of the binary system holds the intrinsic information related to SN kicks imparted onto the

CO and hence provides some useful hints for further understanding the physics associated with the core-collapse itself. With the help of recent GAIA (Gaia Collaboration et al., 2018) data release ⁴, accurate position and velocity measurements of galactic XRBs will be used to directly study the natal kicks imparted to SN remnants during core-collapse. More details about this will be given in the last chapter of this thesis where I present some future perspectives. In the following, I introduce the three types of XRBs, with a focus on their potential formation channels and the methods for spin measurement of BH in XRBs.

1.4.1 High-mass X-Ray Binaries

In general, three formation channels of BH HMXBs according to the initial orbit of the binary system have been proposed. In the standard scenario, the more massive star evolves faster and becomes a Wolf-Rayet (WR) star by losing outer hydrogen layers due to stable MT and strong winds. After depletion of the nuclear fusion, the WR star forms a BH through SN explosion, and then a HMXB that contains a BH and main-sequence star forms.

However, another two channels, Case-A MT and chemically homogeneous evolution (CHE) channels, have also been recently proposed. For the former channel, the BH progenitor initiates MT on to its companion while still in the MS (Case-A MT, see Kippenhahn & Weigert, 1967). This formation channel was for the first time proposed by Valsecchi et al. (2010) to explain the formation of M33 X-7. More specifically, a systematic study for this formation channel was carried out by Qin et al. (2019).

Alternatively, if the two components are close enough (orbital period around a few days), especially for low metallicity (i.e. not higher than 1/3 solar metallicity), the two stars rotate fast due to tidal locking, and hence evolve chemically homogeneously as efficient chemical mixing is caused by fast rotation (Maeder, 1987; de Mink et al., 2009; Marchant et al., 2016; Song et al., 2016). Fig. 1.14 shows a schematic formation of HMXBs through CHE. In the scenario, the two stars stay compact due to fast rotating and MT throughout the whole evolutionary process is avoided. Fast rotating BH can be formed via the two channels, and the Case-A MT channel could explain well the current observed 3 systems with close orbits. More details about the two channels for explaining the current observed 3 HMXBs are given in Qin et al. (2019).

1.4.2 Low-mass X-Ray Binaries and Intermediate-mass X-Ray Binaries

In this standard scenario (Tauris & van den Heuvel 2006 and references therein) for the LMXBs formation, the more massive star expands after the MS, and initiates unstable MT on a dynamical timescale due to an extreme mass ratio. This process is called CE phase, which is the most uncertain process and poorly understood in the classical binary evolution. Relevant discussions related to some uncertain physical parameters, as well as other proposed formation channels for LMXBs can be found in recent review (Li, 2015). The IMXBs are not easily

⁴<https://www.cosmos.esa.int/web/gaia/dr2>

recognized due to a short-lived X-ray phase. They will become LMXBs by losing mass via stellar winds or mass transfer to its companion.

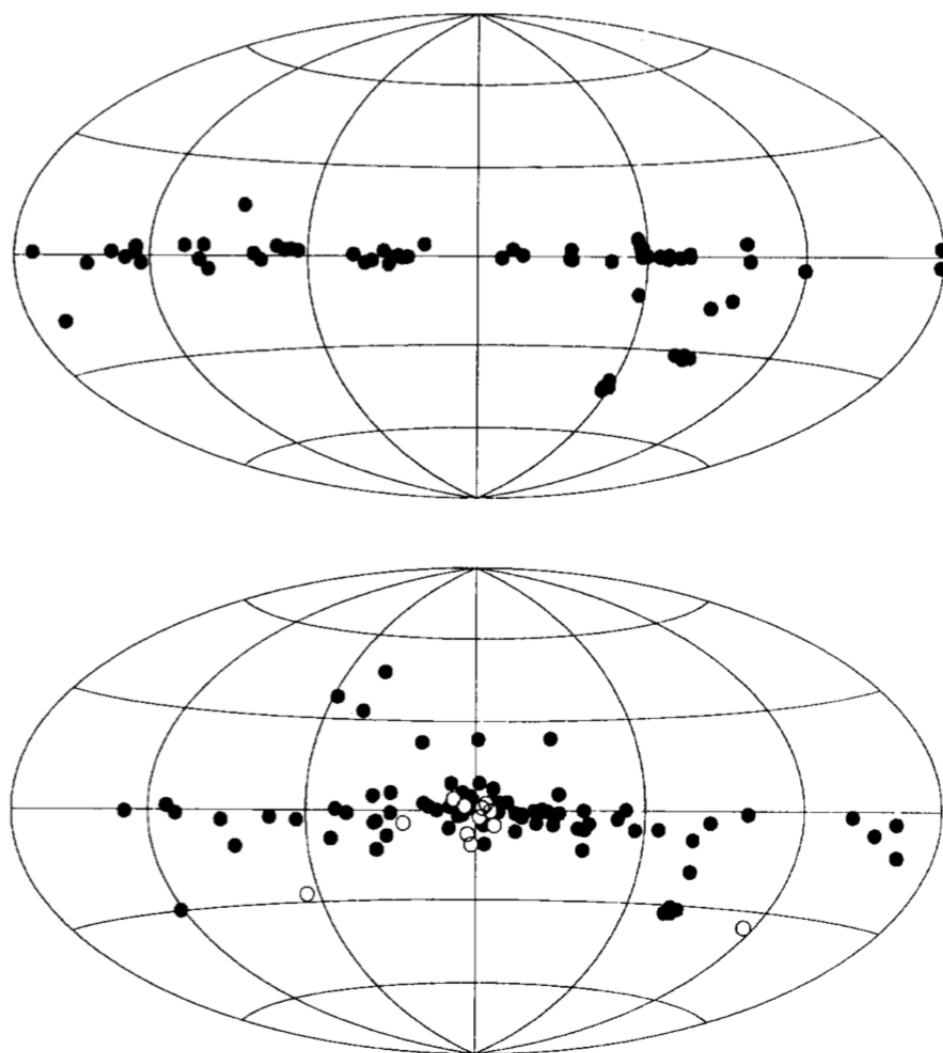


Figure 1.11: Distribution of galactic HMXBs (top) and LMXBs (bottom). Open circles represent LMXBs in globular clusters. This figure is from van Paradijs (1998).

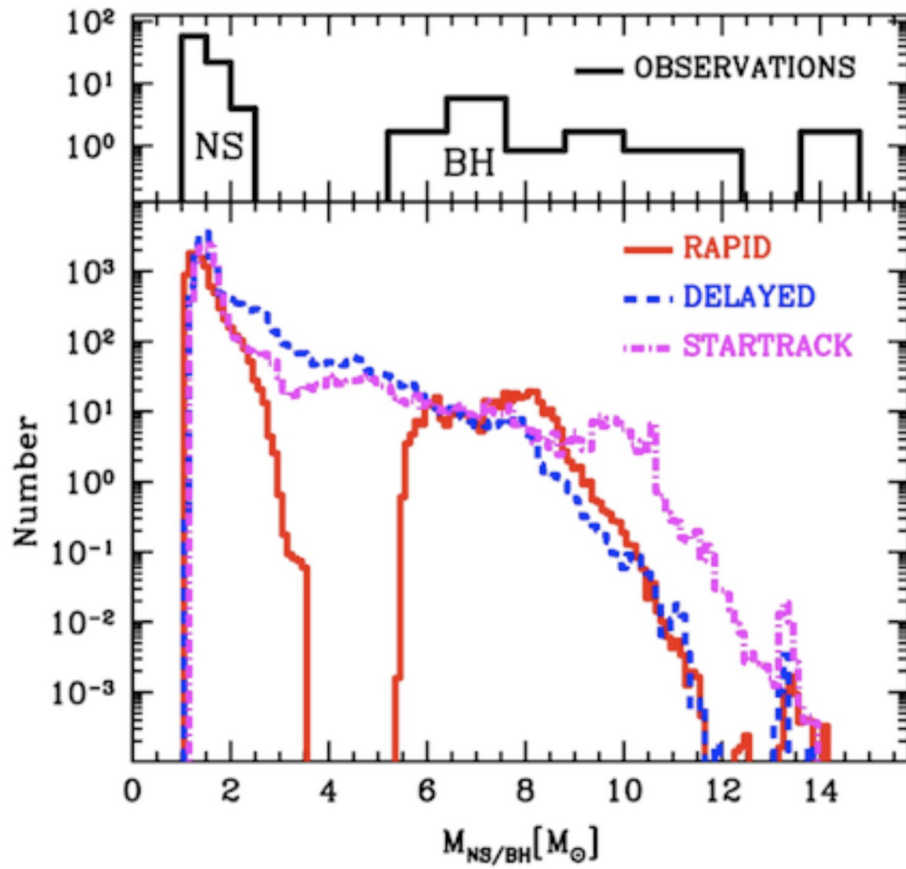


Figure 1.12: Mass distribution of observed galactic COs in XRBs (top) and mass distribution of theoretical simulations from different SN models (bottom). This figure is from Belczynski et al. (2012).

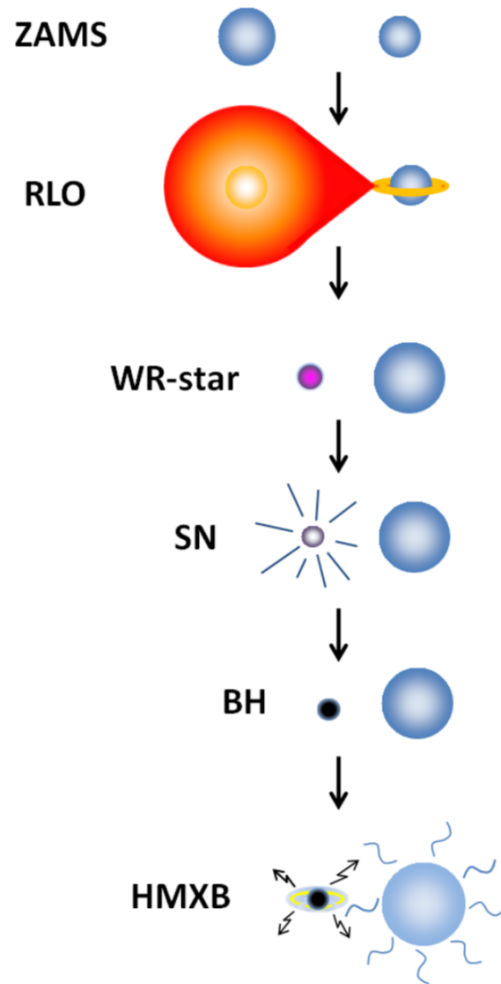


Figure 1.13: The standard scenario of binary stellar evolution that forms a HMXB. ZAMS: zero-age MS; RLO: Roche-lobe overflow; WR-star: Wolf-Rayet star; SN: supernova; BH: black hole. This figure is from Marchant et al. (2016).

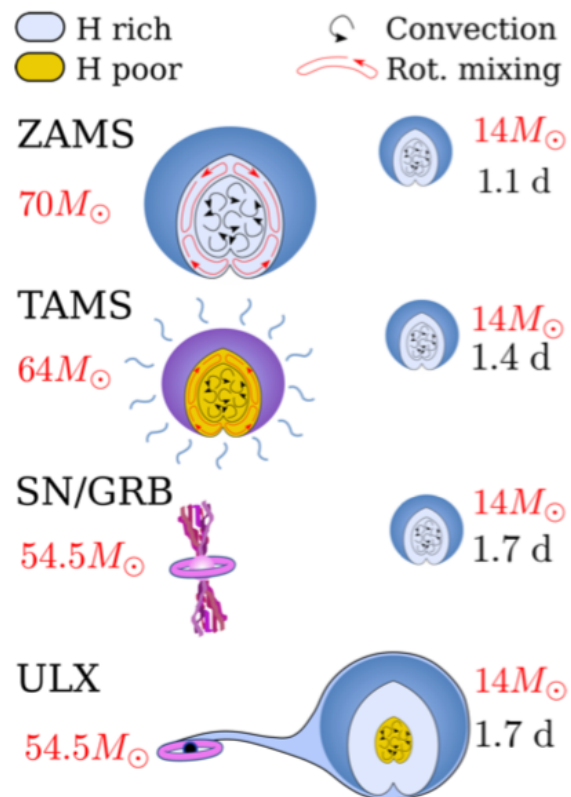


Figure 1.14: Schematic formation of HMXB through CHE. TAMS: terminal-age MS; GRB: Gamma-Ray Burst; ULX: ultra-luminous X-ray sources. This figure is from Marchant et al. (2017).

1.4.3 Measurements of BH spins

For astrophysical BH, its dimensionless spin \vec{a}^5 is determined by its spin AM \vec{J} and mass M as follows

$$\vec{a}_* = c\vec{J}/GM^2, \quad (1.23)$$

where c is the speed of light in vacuum. The innermost stable circular orbit (r_{ISCO}) refers to a major transition point in disk physics inside which no stable circular orbits are available and the gas falls dynamically into the BH (McClintock, Narayan, & Steiner, 2014). In order to estimate the BH spin, r_{ISCO} is introduced and defined below

$$r_{\text{ISCO}} = r_g \left\{ 3 + Z_2 \mp [(3 - Z_1)(3 + Z_1 + 2Z_2)]^{1/2} \right\}, \quad (1.24)$$

where $r_g = GM/c^2$, $Z_1 \equiv 1 + (1 - a_*^2)^{1/3} \left[(1 + a_*)^{1/3} + (1 - a_*)^{1/3} \right]$, and $Z_2 \equiv (3a_*^2 + Z_1^2)^{1/2}$. Here “-” and “+” sign in the equation above refer to the r_{ISCO} that are for prograde and retrograde orbits with respect to the BH spin, respectively. Then a BH has a maximum spin with $a_* = 1$ and $r_{\text{ISCO}} = GM/c^2$ for prograde orbits, while a non-rotating (Schwarzschild) BH has $r_{\text{ISCO}} = 6GM/c^2$.

There are two widely used methods that have been proposed to indirectly estimating the spins of the BHs (Remillard & McClintock, 2006), i.e., Fe-line method and Continuum-Fitting method. In both methods, the accretion disk around the BH is used to infer its spin. It is assumed that the disk is geometrically thin and radiatively efficient, and the innermost stable circular orbit (ISCO) is considered to be the inner boundary where the fitted emission is terminated (Miller & Miller, 2015). A brief introduction for the two methods is given in the following.

The Fe-line Method

The Fe-line method (a.k.a X-ray reflection spectroscopy) is a powerful tool that allows us to measure the spin of the stellar-mass BHs and the supermassive BHs in active galactic nuclei. Applying this method will allow us to acquire the innermost stable circular orbit r_{ISCO} , and then the spin a_* by modeling the Fe-line formed in the disk by Doppler effects, light bending, as well as gravitational redshift (Fabian, Rees, Stella, & White, 1989; Reynolds, 2014). In this method, the Fe-line is the most prominent feature in the reflection spectrum. In general, some basic assumptions (see more below) and the geometry of the accretion disk are the key to determine the BH spin (Reynolds, 2014).

- Basic Assumptions

The key assumption of this method is that the accretion disk is geometrically-thin, optically thick, and radiatively efficient down to the r_{ISCO} (Reynolds, 2014). The accreted material flows across the ISCO, the inward

⁵In the rest of the thesis, a_* refers to the magnitude of the spin and it covers from 0 (non-rotating BH) to 1 (maximally rotating BH). $a_* = 0.998$ is considered to be the upper limit of BH spin proposed by Thorne (1974) showing that fast rotating BH would be spun down by photons emitted retrograde to the spin. But in this thesis, $a_* = 1$ is considered to be the maximum spin.

velocity quickly increases. The flow quickly becomes super-sonic, and the density of the flow rapidly drops due to conservation of mass flux. This behaviour was confirmed by magnetohydrodynamical simulations (Reynolds & Fabian, 2008; Penna et al., 2010). The ISCO is considered as the “inner-dege” of the accretion disk. The BH spin can be estimated based on the monotonic function (Bardeen, Press, & Teukolsky, 1972) shown in Fig. 1.15 (Here I only show a prograde orbit with respect to BH spin a_* and a complete one will be presented in the method of the Continuum-Fitting method.) between r_{isco}/r_g and spin a_* .

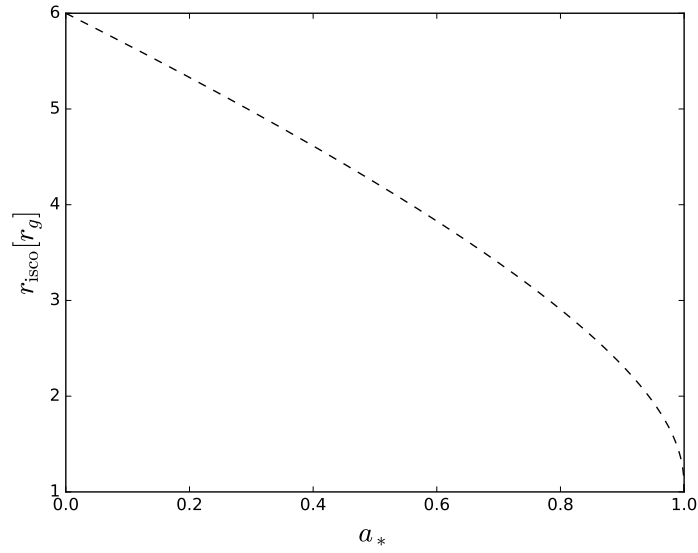


Figure 1.15: r_{isco}/r_g as a function of the BH spin a_* .

- Geometry

In addition to the basic assumptions above, the geometry of the accretion disk also plays a key role in determining the BH spin. The X-ray reflection terminates where the inward flow reaches the ISCO. Inside the ISCO, the region is fully ionized by the X-ray irradiation of the inward flow. Therefore, there is no contribution to the observed atomic signatures, and hence no iron absorption within the ISCO. However outside of the r_{ISCO} , the disk is optically thick and has some combined metal ions. As shown in Fig. 1.16, we can see atomic emissions sitting on top of a Compton-backscattered continuum. The most important feature of the X-ray reflection spectrum is the iron $K\alpha$ line is around 6.4 – 6.97 keV (Reynolds, 2014).

- Current stellar-mass BH spin measurements via Fe-line method

Barr, White, & Page (1985) for the first time found the broad iron line in the *EXOSAT* spectrum of Cygnus X-1 and explained that the line broadening is due to the Compton scattering of iron emission line photons in the disk atmosphere. Combining this observation and the method mentioned above made the BH spin

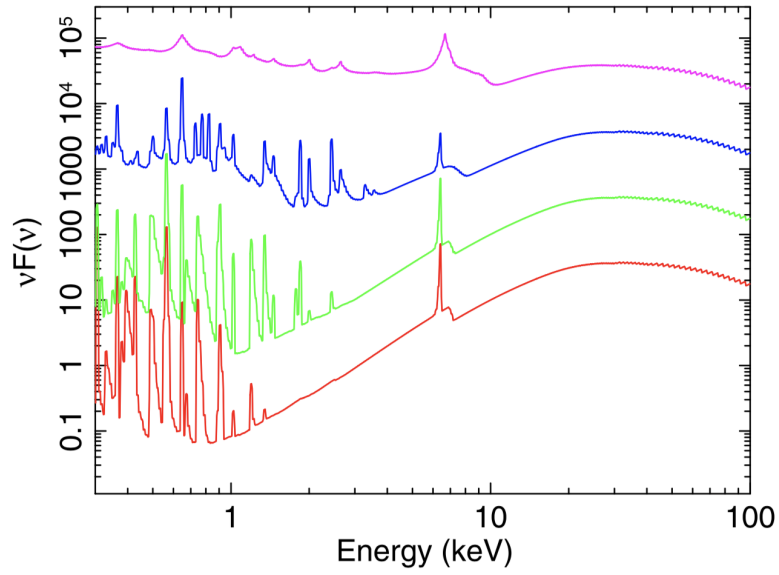


Figure 1.16: The rest-frame X-ray reflection spectrum of the photospheric ionization parameters for $\log \xi = 3, 2, 1, 0$ (from top to bottom). This figure is from Reynolds (2014).

measurement possible. Table 1.1 shows currently published stellar-mass BH spin measurements obtained by the Fe iron line method. For some of these objects, the BH spins were measured via the Continuum-Fitting method, which is explained below.

Table 1.1: BH spin measurements via the Fe-line method

Sources	a_*	References
4U 1543–475	0.3 ± 0.1	Mi09/Sh06
Cygnus X-1	> 0.95	Fa12/Go11
GX339–4	0.94 ± 0.02	Mi09
GRS1915+105	> 0.97	Bl09/Mc06
GRO J1655–40	> 0.9	Rei09/Sh06
LMC X 1	0.55	St12/Go09
MAXI J1836–194	0.88 ± 0.03	Rei12
SAX J1711.6–3808	$0.6^{+0.2}_{-0.4}$	Mi09
Swift J1753.5–0127	$0.76^{+0.11}_{-0.15}$	Rei09
XTE J1550–564	$0.33 - 0.77$	Mi09/St11
XTE J1650–500	0.79 ± 0.01	Mi09
XTE J1652–453	0.45 ± 0.02	Hi11
XTE J1752–223	0.52 ± 0.11	Rei11
XTE J1908+094	0.75 ± 0.09	Mi09

BH spin a_* is shown with 90% level of confidence.

References: Bl09 = Blum et al. 2009; Fa12 = Fabian et al. 2012; Go11 = Gou et al. 2011; Hi = Hiemstra et al. 2011; Mc06 = McClintock et al. 2006; Mi09 = Miller et al. 2009; Rei09 = Reis, Miller, & Fabian 2009; Rei11 = Reis et al. 2011; Rei12 = Reis et al. 2012; Sh08 = Shafee et al. 2008; St11 = Steiner et al. 2011; St12 = Steiner et al. 2012

The Continuum-Fitting Method

Another approach to measuring BH spin is the continuum Fitting method, which was for the first time proposed by Zhang, Cui, & Chen (1997). In the Continuum-Fitting method, the determination of BH spin requires extra information, i.e., the luminosity of the accretion disk, the source distance D , and the disk inclination i . In addition, the mass of the BH is necessarily needed to scale r_{isco} . For simplicity, the main feature is that one fits the thermal continuum spectrum of an accretion disk to a relativistic thin-disk model of NT model (Novikov & Thorne, 1973) and then determines the radius of the inner edge of the disk (McClintock, Narayan, & Steiner, 2014). Therefore, one identifies the innermost stable circular orbit r_{isco} and then obtains the BH spin using the monotonic function between r_{isco}/r_g and spin a_* (Bardeen, Press, & Teukolsky, 1972). Compared to the Fe-line method, this thin-disk model is simpler, and well confirmed (Novikov & Thorne, 1973). More importantly, a larger amount of spectra data (*RXTE* PCA, *Ginga* LAC, *ASCA* GIS, etc.) is available for the application of this method. In contrast, the data for the Fe-line method is sparse, and its signal of the Fe-line is much fainter. In this part, I first briefly present some assumptions of the NT models and then present the implementation of the continuum fitting (More details in McClintock, Narayan, & Steiner, 2014).

- Introduction of the NT model

As introduced above, the ISCO is considered as the inner edge of the disk, which indicates a transition point in the disk physics. As gas flows inward, it steadily loses its AM that is due to magnetic stresses coming from the magnetorotational instability (Balbus & Hawley, 1998) via the α -viscosity and then terminates when reaching the radius of the ISCO. Then the gas rapidly falls into the BH once it enters into the radius of the ISCO.

As shown in Fig 1.17, the BH spin a_* is a monotonic function of the radius of the ISCO, and so it is possible to measure a_* by modeling the emission in the disk. In the NT model (Novikov & Thorne, 1973), one determines an analytical solution for the differential luminosity $dL(R)/dR$ as a function of the radius R . In Fig 1.18, we can see for three different values of a_* the differential disk luminosity predicted based on the NT model (McClintock, Narayan, & Steiner, 2014).

we can see three different spin values of a_* given based on the NT model. The disk luminosity reaches a peak and then gradually decreases outward. The most important feature is that for a given total disk luminosity, the temperature of the radiation increases with increasing spin a_* , which is the key in the application of the continuum fitting method.

Based on the NT model, it is possible to estimate the BH spin a_* by measuring the luminosity and the temperature in the disk. Therefore, the accuracy of the Continuum-Fitting method depends on the reliability

of the NT model. In addition to this, the calculation of the radiation spectrum would also have an impact on the determination of the BH spin a_* . More details are beyond this thesis, but can be found in McClintock, Narayan, & Steiner (2014).

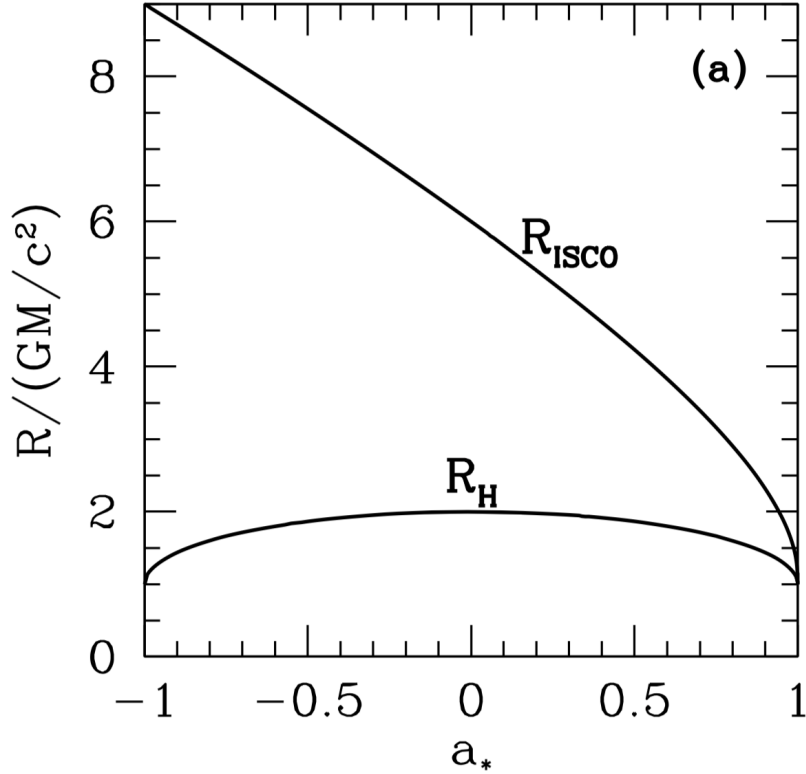


Figure 1.17: r_{isco} and radius of the horizon R_H in units of r_g (i.e. GM/c^2) as a function of the BH spin a_* . Positive and negative values of a_* refer to the prograde and retrograde orbits, respectively. This figure is from McClintock, Narayan, & Steiner (2014).

- Continuum-Fitting to the NT model

In order to fit the X-ray continuum spectrum to the NT model of a thin accretion disk, one still needs other spectral components, i.e., a Compton component. As mentioned above, extra accurate input parameters, the source distance D , disk inclination i and BH mass M , are required in the spectra fitting process. The BH spin a_* together with the mass accretion rate \dot{M} then will be returned as the main output parameters.

In practice, in order to fit the thermal component, one needs to use *KERRBB2* (Remillard & McClintock, 2006), which is a hybrid code that combines two relativistic disk models, *BHSPEC*⁶ (Davis, Blaes, Hubeny, & Turner, 2005) and *KERRBB* (Li, Zimmerman, Narayan, & McClintock, 2005). *KERRBB* is a detailed

⁶it is a reliable model of the disk's atmosphere

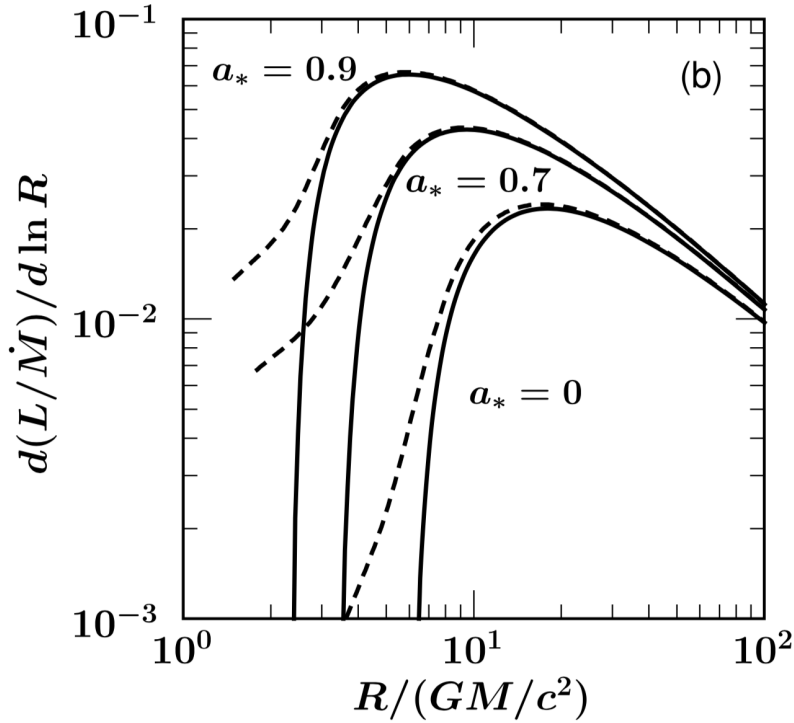


Figure 1.18: $dL(\dot{M})/d\ln R$ as a function of the radius R (in unit of GM/c^2) for three different values of a_* (0.9, 0.7 and 0). Solid lines present the predictions from the NT model, and the dashed lines come from the results of Zhu et al. (2012). Relevant discussion of their discrepancies is shown in McClintock, Narayan, & Steiner (2014). This figure is from McClintock, Narayan, & Steiner (2014).

implementation of the NT model, which has three fitting parameters, BH spin a_* , accretion rate \dot{M} and a spectra hardening factor f that relates the observed temperature to the effective temperature, i.e., $f = T/T_{\text{eff}}$. A further constraint on the spectra hardening factor f is obtained by pairing the *KERRBB* with *BHSPEC* that can be used for fit directly for BH spin a_* (McClintock, Narayan, & Steiner, 2014). Here I show you one case of a successful application of the Continuum-Fitting method. In Fig. 1.19, it shows a disk-dominated spectrum of LMC X-3 with a peak flux in the Compton component.

- Current BH spin measurements via Continuum-Fitting method

Some objects with BH spin a_* measurements via Continuum-Fitting method are listed in Table 1.2. The spin a_* covers the whole range of prograde values.

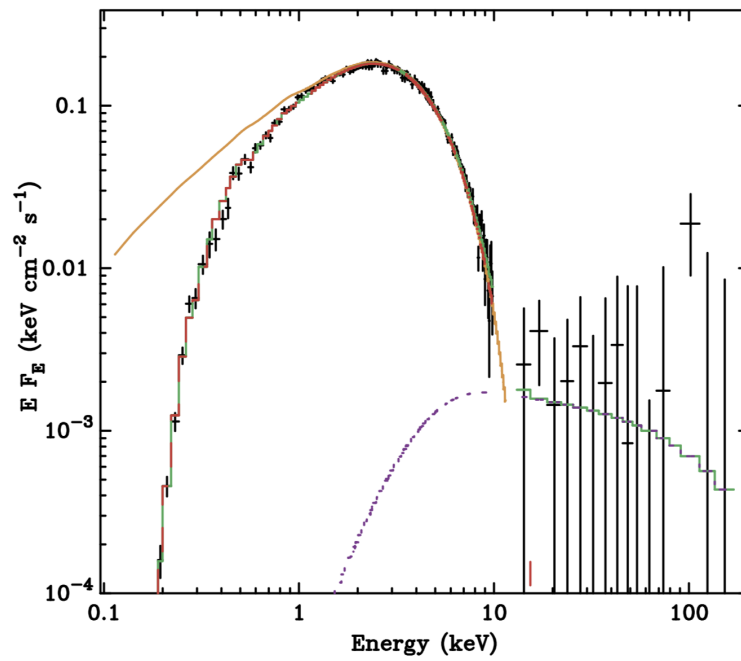


Figure 1.19: Fitting spectrum of LMC X-3 by using the data from *BeppoSAX* satellite ($D = 52$ kpc, $i = 67^\circ$ and $M = 10 M_\odot$ in Davis & Hubeny 2006). This figure is from McClintock, Narayan, & Steiner (2014).

Table 1.2: BH spin measurements via the Continuum-Fitting method

Sources	a_*	M/M_\odot	References
Cygnus X-1	> 0.95	14.8 ± 1.0	(1), (2)
LMC X-1	$0.92^{+0.05}_{-0.07}$	10.9 ± 1.4	(3), (4)
M33 X-7	0.84 ± 0.05	15.65 ± 1.45	(5), (6), (7)
GRS 1915+105	0.95	10.1 ± 0.6	(8), (9)
4U 1543–47	0.80 ± 0.10	9.4 ± 1.0	(10), (11)
GRO J1655–40	0.70 ± 0.10	6.3 ± 0.5	(10), (12)
XTE J1550–564	$0.34^{+0.20}_{-0.28}$	9.1 ± 0.6	(13), (14)
H1743–322	0.2 ± 0.3	8	(15)
LMC X-3	< 0.3	7.6 ± 1.6	(16), (11)
A0620–00	0.12 ± 0.19	6.6 ± 0.25	(17), (18)

BH spin a_* is shown with 68% level of confidence.

References: (1) Orosz et al. 2011, (2) Gou et al. 2014 (3) Orosz et al. 2009, (4) Gou et al. 2009, (5) Orosz et al. 2007, (6) Liu et al. 2008, (7) Liu et al. 2010, (8) McClintock 2006, (9) Steeghs et al. 2013, (10) Shafee et al. 2006, (11) Orosz 2003, (12) Greene, Bailyn, & Orosz 2001, (13) Steiner et al. 2011, (14) Orosz et al. 2011, (15) Steiner, McClintock, & Reid 2012, (16) Davis & Hubeny 2006, (17) Gou et al. 2010, (18) Cantrell et al. 2010

1.5 Progenitors of Merging Stellar-Mass Black Holes

Gravitational waves (GWs) were first predicted by Albert Einstein in 1916. The discovery of the binary pulsar PSR B1913+16 by Hulse & Taylor (1975) and subsequent observations of the energy loss found by Taylor & Weisberg (1982) confirmed the existence of GWs.

The detection of the first GW (GW150914) event (Abbott et al., 2016a) from a double BH system was found by the Advanced Laser Interferometer Gravitational-Wave Observatory (AdLIGO; LIGO Scientific Collaboration et al., 2015). This discovery has opened a new window for the study of the BHs. Furthermore, on August 17, 2017, a GW signal from the inspiral of two NSs merger by the LIGO-Virgo detector (Abbott et al., 2017a) was discovered. To date, ten GW events related to double BH merging and one from double NS merging have been found. In the following, a brief introduction of the first GW event (GW150914) and relevant theoretical models for GW progenitor are presented, respectively.

1.5.1 Observational results of the first GW event: GW150914

On September 14, 2015, the LIGO detectors at Hanford, Washington and Livingston Louisiana detected the GW signals of the GW150914. As shown in Fig. 1.20, the AdLIGO measures GW150914 strain with a difference in length of its perpendicular arms. The relative difference in the length of the AdLIGO arms produced by GW150914 is less than 10^{-20} .

This event signal shown in Fig. 1.21 was detected on September 14, 2015 by AdLIGO detectors at Hanford, Washington (H1) and Livingston Louisiana (L1). In the matched-filter analysis, relativistic models of compact binary waveforms recovered GW150914 signal from the second row in both detectors shown in Fig. 1.21. Unfortunately, during this observing times, the Virgo detector was being upgraded and not in observational mode. The GW150914 event represents the significant feature meaning the coalescence of two BHs, i.e., their orbital inspiral, merger, and subsequent ringdown, which is shown in Fig. 1.22. During the whole time of 0.2 s, the signal frequency (from 35 to 150 HZ) and amplitude in both detectors increases. The explanation is that two orbiting BHs with masses, m_1 and m_2 , coalesce due to the GW emission.

There are two quantities that can be obtained from the signal of GWs, i.e, chirp mass M_{chirp} and the effective inspiral spin parameter χ_{eff} . The chirp mass M_{chirp} , which is determined by the observed frequency f and its time derivative \dot{f} , is defined as,

$$M_{chirp} = \frac{(m_1 m_2)^{3/5}}{(m_1 + m_2)^{1/5}} = \frac{c^3}{G} \left[\frac{5}{96} \pi^{-8/3} f^{-11/3} \dot{f} \right]^{3/5}, \quad (1.25)$$

where G and c are the gravitational constant and speed of light in vacuum. A complete analysis of numerical relativity model for GW150914 is shown in Fig. 1.22. The frequency f and its time derivative \dot{f} can be estimated from the signal in this figure. Then the M_{chirp} is obtained by using the Eq. 1.25. The decrease of the strain amplitude

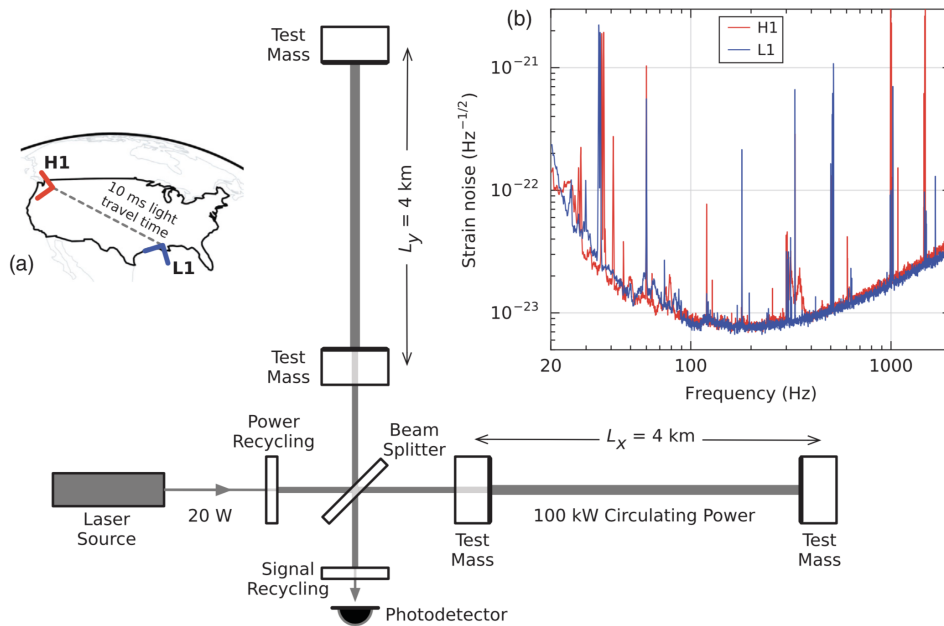


Figure 1.20: Simplified diagram of the AdLIGO detector. (a): Location of the AdLIGO detectors at Hanford, Washington (H1) and Livingston Louisiana (L1). (b): Amplitude spectral density (in terms of equivalent gravitational-wave strain amplitude). This figure is from Abbott et al. (2016a).

shows the decay of the waveform after it reaches the peak, which is consistent with the damped oscillations of a BH relaxing to a final stationary Kerr configuration (Abbott et al., 2016a).

The χ_{eff} (see Fig. 1.23) is considered to be another quantity that can be extracted from the GW signal. It has been suggested that this quantity can identify the formation channel of the GW progenitors, however, currently observed sample is not enough to be statistically used. More discussions for this are given in the following part.

1.5.2 Formation channels of merging stellar-mass black holes

Various binary BH formation channels have been proposed since the discovery of the GW150914 event by the AdLIGO. There are three main channels proposed to explaining the progenitor of double BHs, i.e., *Common Envelope (CE) channel* (Phinney, 1991; Tutukov & Yungelson, 1993; Belczynski, Holz, Bulik, & O’Shaughnessy, 2016; Tutukov & Cherepashchuk, 2017), *Chemically homogeneous evolution (CHE) channel* (de Mink & Mandel, 2016; Marchant et al., 2016; Mandel & de Mink, 2016) and *dynamical channel* in globular clusters (Sigurdsson & Hernquist, 1993; Rodriguez et al., 2015, 2016). These three main channels are briefly shown in the following.

- *CE channel*

The first channel is also called classical isolated binary evolution, which has been well studied. In this scenario shown in Fig. 1.24, a massive binary is formed initially in a wide orbit (typically the orbit is around a

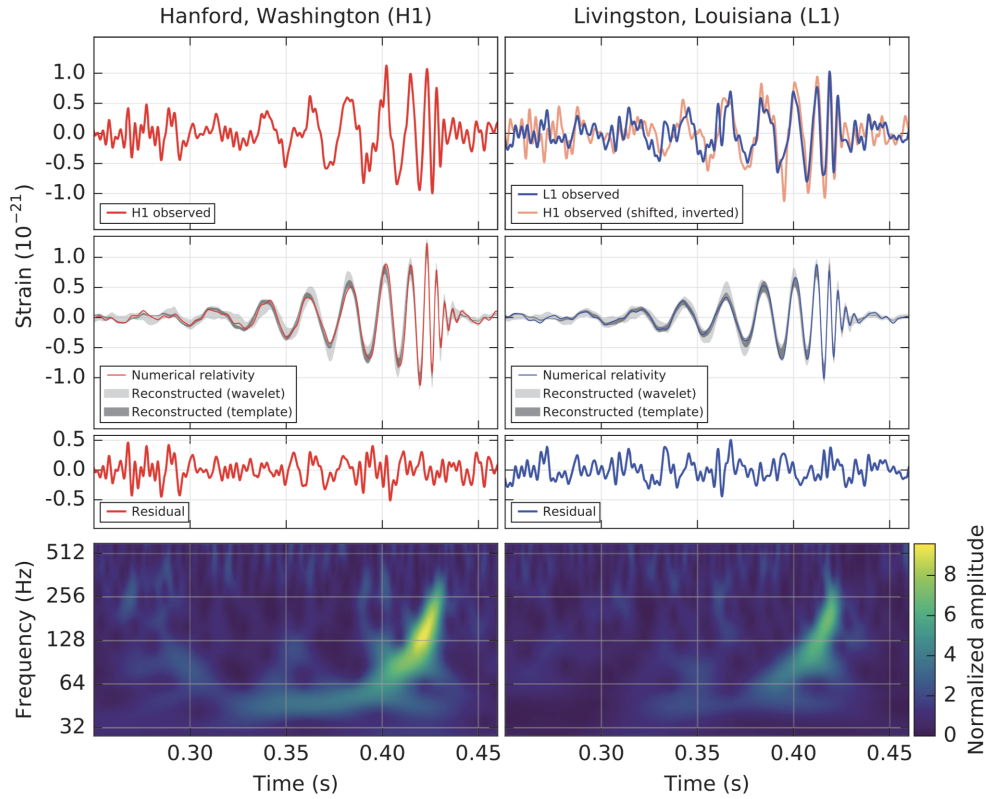


Figure 1.21: The GW150914 event detected by LIGO H1 detector (left panel) and L1 detector (right panel). Top left row: H1 strain; top right row: L1 strain. Second row: GW strain in each detector. Solid lines represent the waveform of a numerical relativity that is consistent with the GW150914. Shaded areas refer to 90% credible confidence level from independent waveform reconstructions. Third row: Residuals after the numerical waveform subtracted from the filtered detector time series. Bottom row: the signal frequency increasing with the time. This figure is from Abbott et al. (2016a).

few thousand solar radii). The more massive star expands to become a red supergiant star after the depletion of core hydrogen burning and then undergoes stable MT. After losing its entire hydrogen envelope, the primary becomes a helium star (Wolf-Rayet star), and then rapidly forms the BH (first-born BH). When the secondary depletes its core hydrogen and expands, an inverse MT initiates onto the primary. The MT onto the BH undergoes to a dynamical unstable MT process that leads to the formation of a CE. The viscous drag on BH in the envelope results in a rapid inspiral. Through this process, the orbital energy is dissipated to eject the envelope and ultimately a close BH-helium star forms. As a result, the double BHs will then merge due to GW emission.

- *CHE channel*

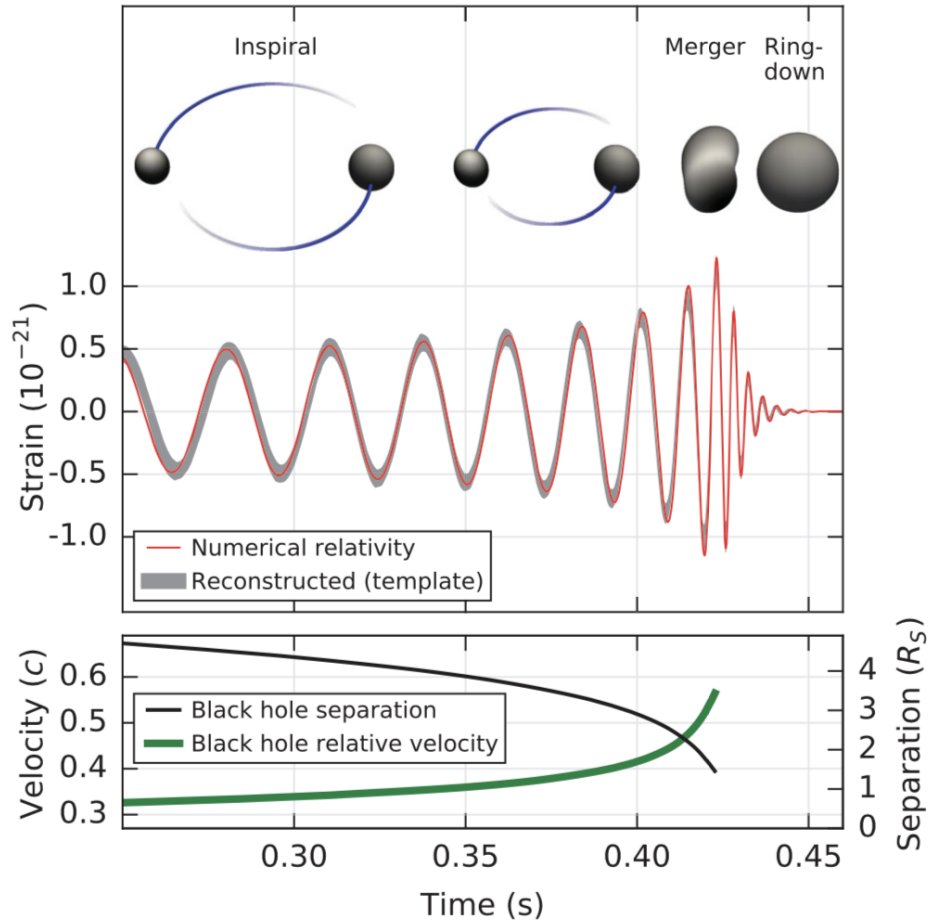


Figure 1.22: Top panel: Numerical relativity models of the BHs as they coalesce and estimated GW strain amplitude for GW150914 of detector H1. Bottom panel: The Keplerian effective BH separation in units of Schwarzschild radii ($R_s = 2GM/c^2$) and the effective relative velocity. This figure is from Abbott et al. (2016a).

Massive stars induced by rotational mixing evolve chemically homogeneously throughout core hydrogen burning (Maeder, 1987). Studies of CHE for massive close binaries were for the first time made by de Mink et al. (2009). As shown in Fig. 1.25, both stars stay compact and the MT is avoided. Such formation channel has been extensively studied recently (de Mink & Mandel, 2016; Marchant et al., 2016; Mandel & de Mink, 2016; Song et al., 2016). In addition, CHE is also considered to be an alternative approach to predicting BH with high spin a_* in HMXBs (Qin et al., 2019). However, this model predicts orbit periods that are too large for currently three observed systems and more studies in detail are presented in chapter 4.

- *Dynamical formation channel*

In dense stellar environments, the BHs naturally segregate towards the center of the cluster. Many interactions with other objects in the cluster would gradually tighten a binary BH system. Fig. 1.26 shows a simplified

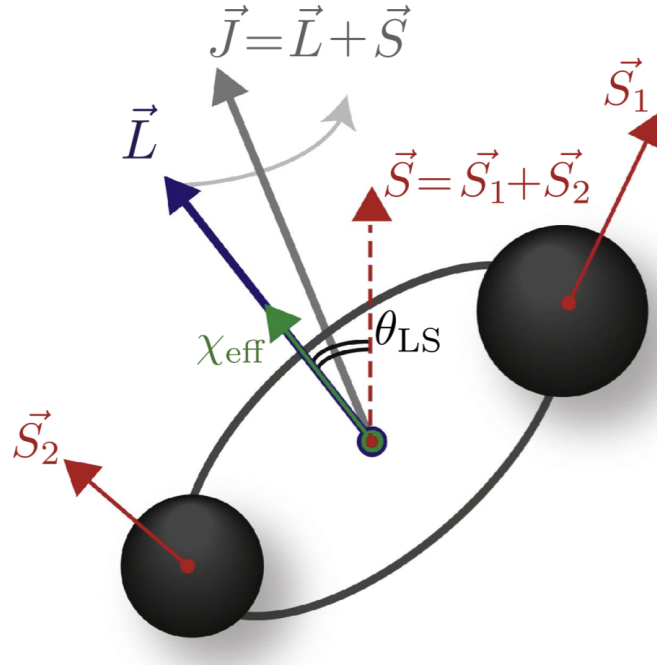


Figure 1.23: Diagram of the vectors and angles for a rotating double BH system. \vec{J} (grey symbol): total AM, \vec{L} (blue symbol): orbital AM, \vec{S} : total spin AM (red symbol). The χ_{eff} is shown along the direction of \vec{L} with a green arrow. This figure is from Rodriguez et al. (2016).

process of the dynamical friction in a globular cluster and eventually a close binary BH forms through multiple three-body dynamical interactions.

As mentioned earlier, χ_{eff} can be used to distinguish the formation channels of double BHs. For *CE channel*, both spins of two BHs is expected to be aligned to the orbital angular momentum throughout the whole evolution process. The more massive star evolves almost like a single star due to weak tides, and is expected to have a negligible spin. The spin of the second-born BH covers the whole range (from 0 to 1). The spins a_* of the BHs could retain significant memories of their evolutionary processes. Based on the detailed binary evolution through this channel, I show in Fig. 1.27 the timescale for the merger of a binary BH due to GWs as a function of χ_{eff} and M_{chirp} . At high metallicity environment, massive stars form low-mass BHs due to strong mass-loss winds, and on the other hand, high-mass BHs could be formed in a low metallicity environment. Detailed studies of the χ_{eff} for this channel is given in chapter 3. Currently, all the available GW events are well consistent with the predictions through CE channels.

Alternatively, the progenitors of two BHs evolve chemically homogeneously instead if they rotate fast. In this *CHE channel*, both BHs have a significantly high spin and hence result in a high χ_{eff} . In addition to binary evolution channels (CE and CHE), the two BHs can also form separately in a dense cluster, and then would be

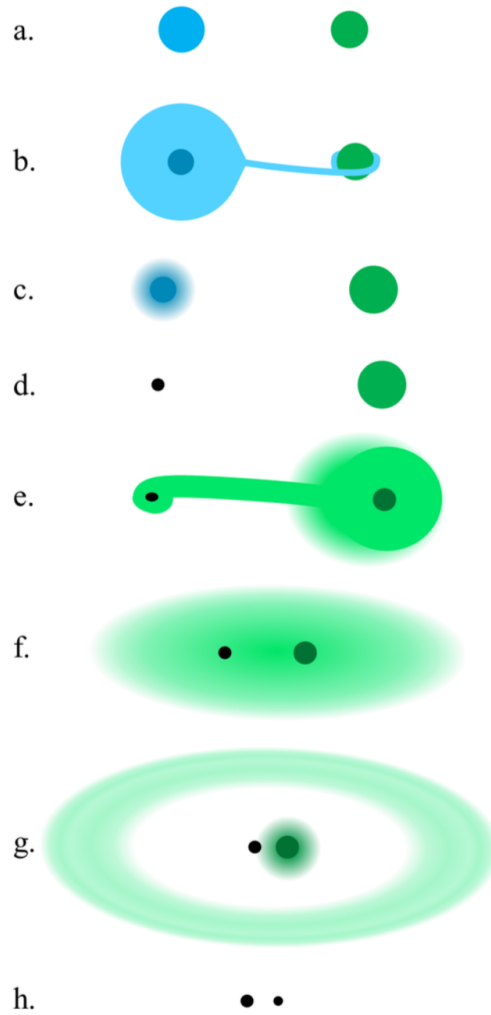


Figure 1.24: Merging BH binary formation via CE channel. This figure is from Mandel & Farmer (2018).

brought together through dynamical friction. The spins of the two BHs from this formation channels are expected to have a random, isotropically distributed direction. Therefore, it is expected that the observable quantity χ_{eff} is close to zero.

However, a limited number of currently observed distribution of χ_{eff} is not enough to be statistically useful for distinguishing various formation channels of double BHs. The third run (O3) of LIGO is still in the process of improving its sensitivity during my writing of thesis, and the sample will be significantly increased during the third run. Therefore, a reliable result can be obtained with a large sample of the GW events, which can be used for understanding the historical formation processes of double BHs.

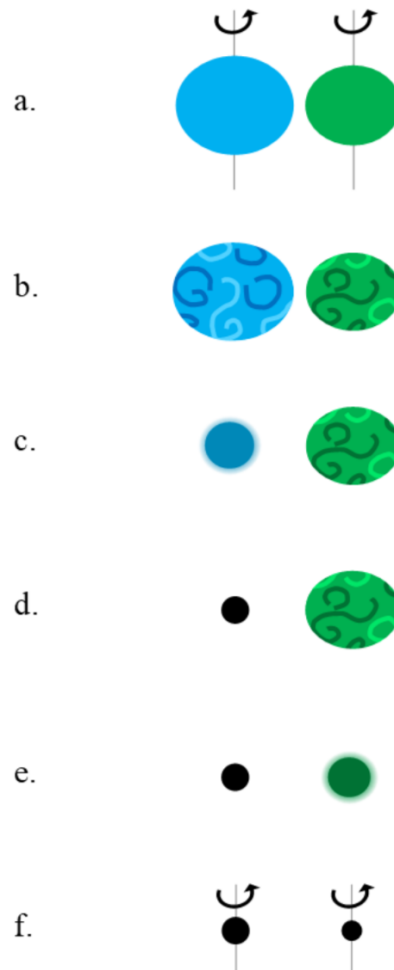


Figure 1.25: Merging BH binary formation via CHE channel. This figure is from Mandel & Farmer (2018).

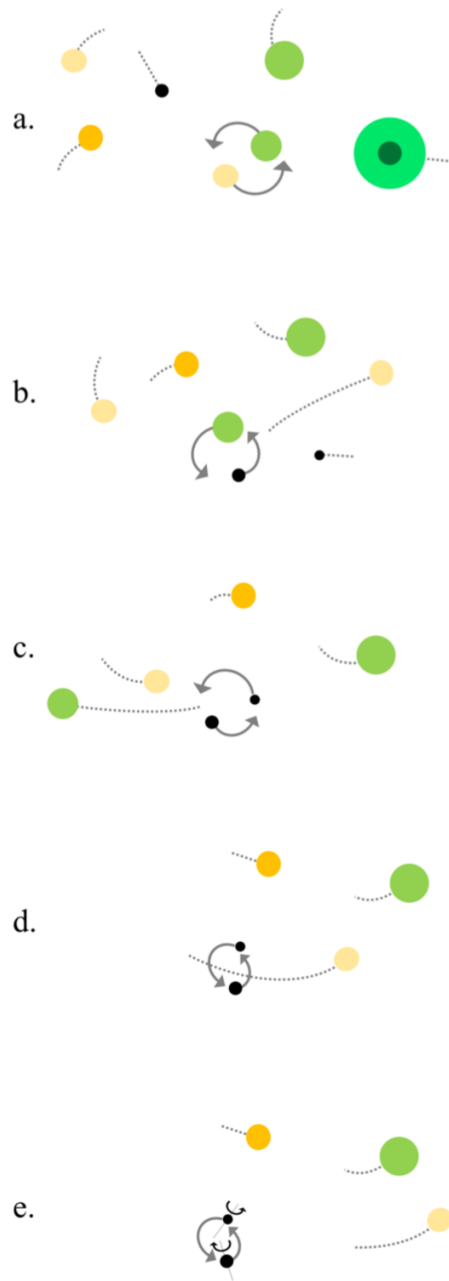


Figure 1.26: Merging BH binary formation via dynamical channel. This figure is from Mandel & Farmer (2018).

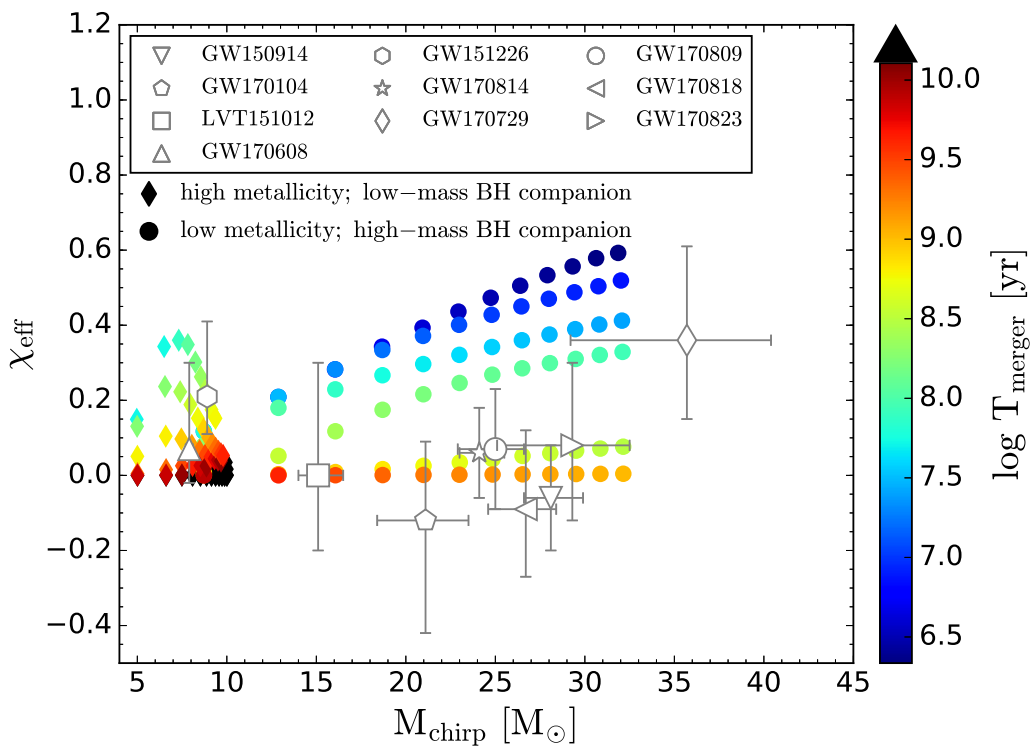


Figure 1.27: T_{merger} as a function of χ_{eff} and chirp mass M_{chirp} . Different empty symbols represent currently observed GW events. Black diamonds and circles represent models at solar metallicity and 0.01 solar metallicity.

1.6 This Thesis

My research is focused mainly on detailed stellar structure and binary evolution, especially tracking the evolution of AM transport of the star by taking into account the stellar winds, differential rotation, tidal interaction with its companion, and MT through Roche-lobe overflow of donor star.

1.6.1 Calculation of tidal coefficient E_2

In §2, we introduce the detailed calculation of the tidal coefficient E_2 for both H-rich and He-rich stars. For H-rich stars, we covered the masses from 4 to 40 M_\odot for metallicity $Z = 0.01 Z_\odot$, $0.1 Z_\odot$ and Z_\odot . Similar computations were performed for He-rich stars. In the end, for both cases, we provided new prescriptions for the tidal coefficient E_2 for both H-rich and the He-rich stars.

1.6.2 The spin of the second-born black hole in coalescing binary black holes

In §3, we present the studies on the spin of the second-born BH in coalescing binary BHs. Various binary black hole formation channels have been proposed since the first gravitational wave event GW150914 Abbott et al. (2016a) was discovered by AdLIGO. The immediate progenitor of the binary BH is a close binary system composed of a BH and a helium star, which can be the outcome of the classical isolated binary evolution through the CE, or alternatively of the massive close evolution through chemically homogeneous channel.

We focused on the former channel and performed detailed stellar structure and binary evolution calculations that take into account, mass-loss, internal differential rotation, and tidal interactions between the helium star and the BH companion, where we also calculate the strength of the tidal interactions from first principles based on the structure of the helium stars. We argue that the natal spin of the first-born BH through the CE scenario is negligible ($a_* < 0.1$), and therefore the second-born BH's spin dominates the measured effective spin T_{eff} from GW events of double BH mergers. We find that tides can be only important when orbital periods are shorter than 2 days. Upon core collapse, the helium star produces a BH (the second-born BH in the system) with a spin that can span the entire range from zero to maximally spinning. We show that the bimodal distribution of the spin of the second-born BH obtained in recent papers is mainly due to oversimplifying assumptions. We find an anti-correlation between the merging timescale of the two BHs, T_{merger} , and the effective spin T_{eff} . Finally, we predict that, with future improvements to AdLIGO's sensitivity, the sample of merging binary BH systems will show an overdensity of sources with positive but small T_{eff} originating from lower-mass BH mergers born at low redshift.

1.6.3 On the origin of the black hole spin in High-mass X-ray Binaries

In §4, we introduce the studies on the origin of BH spin in HMXBs, especially with a focus on the formation through Case-A MT or CHE. Sana et al. (2012) found that a large fraction of all massive binaries would exchange

mass with a companion. So Case-A channel is a natural, common outcome of the initial orbital period distribution of massive binaries. The spin of the BH in LMXBs can be well explained through accretion from its companion (Fragos & McClintock, 2015); however, from the observational point of view, the BH spins measured in three HMXBs (i.e., Cygnus X-1, LMC X-1 and M33 X-7) have been found to be near maximal. So the BH's spin is believed to have a different origin. We use **MESA** to investigate the detailed evolution of massive stars in close binary, especially including differential rotation inside the star and MT between two components to study the BH's natal spin in HMXBs by direct core-collapse supernova model.

In our results, we found that weak coupling between the core and envelope inside the star is necessarily required to form a fast-rotating BH in HMXB through Case-A MT and CHE channel. The former one can be well accepted to explain the properties of currently observed Cygnus X-1, LMC X-1, and M33 X-7. Furthermore, through Case-A MT channel, the enhancement of the nitrogen on the companion's surface is considered an effective tool to distinguish from CHE or classical binary evolution channel with CE involved. More importantly, TS dynamo (TS dynamo, produced by differential rotation in the radiative region of the star) has been in debate for decades. Although the slowly rotation of the Solar core is well explained (Eggenberger, Maeder, & Meynet, 2005) with the TS dynamo, such weak coupling (without TS dynamo) between the core and envelope mediated by a strong magnetic field (Spruit, 1999, 2002; Heger, Woosley, & Spruit, 2005) is still necessarily required to explain the observed high BH spins for three known HMXBs.

1.6.4 On the conditions of CHE

Enlightened by the ongoing work, we will plan to systematically investigate the thresholds for triggering the CHE of stars. Mixing induced by the fast rotation can keep massive stars evolving chemically homogeneously through the hydrogen burning phase (Maeder, 1987). This channel was for the first time proposed in binaries by de Mink et al. (2009) and has also been further investigated in recent work (de Mink & Mandel, 2016; Marchant et al., 2016; Mandel & de Mink, 2016; Song et al., 2016). In general, the initial rotation and metallicity are considered the main physics that are responsible for CHE in stars. Besides, we have already found that TS dynamo plays a critical role in transporting AM inside the star. Based on the comparison between **MESA** and **GENEVA**, we find that with the TS dynamo the condition for triggering CHE is similar, however, the result can be significantly different when the TS is not included.

Chapter 2

Calculation of tidal torque coefficient E_2

2.1 Introduction of the tidal torque coefficient

Tides, in a close binary system, have a significant impact on both secular evolution of the orbit and the internal angular momentum of two stars. In general, dynamical tides are dominant for massive stars with radiative envelope and convective core (Zahn, 1977). For dynamical tides, the timescale of synchronization is given by (Zahn, 1977) as follows

$$\frac{1}{T_{\text{sync}}} = -\frac{1}{\Omega - n} \frac{d\Omega}{dt} = 3 \cdot \frac{K}{T} \frac{q^2}{r_g^2} \left(\frac{R}{a}\right)^6, \quad (2.1)$$

$$\left(\frac{K}{T}\right)_r = \left(\frac{GM}{R^3}\right)^{1/2} (1+q)^{5/6} E_2 \left(\frac{R}{a}\right)^{5/2},$$

where Ω and n are the spin angular velocity and the orbital angular velocity, respectively, q is the mass ratio of the secondary star to the primary one, a the orbital separation, r_g^2 is the dimensionless gyration radius of the star. $\left(\frac{K}{T}\right)_r$ is a coupling parameter depending on the tidal interaction mechanism, where G is the gravitational constant, M and R are star's mass and radius.

The synchronization timescale T_{sync} depends on the tidal torque coefficient E_n (only $n = 2$ is considered, as the contributions from larger n are negligible). Hurley, Tout, & Pols (2002) derived a fitting formula based on tabulated results for stars at Zero-Age main-sequence (ZAMS) from Zahn (1977) as follow

$$E_2 = 1.592 \times 10^{-9} \left(\frac{M}{M_\odot}\right)^{2.84}, \quad (2.2)$$

where M is the total mass of a star. This approximation is not accurate, as E_2 is sensitive to the radius of the stellar core (Zahn, 1977). Another widely used one calculated in Yoon, Woosley, & Langer (2010) by fitting the dependence of E_2 on R_{conv}/R from the values in the Table of Zahn (1977) is as follows:

$$E_2 = 10^{-1.37} \left(\frac{R_{\text{conv}}}{R}\right)^8, \quad (2.3)$$

where R_{conv} is the radius of the star's convective core, and R star's radius.

The values for fitting this formula are based on ZAMS stellar models with various masses. This formula has been implemented in recent studies (de Mink et al., 2009; Song et al., 2013, 2018).

However, the values of E_2 do not account for the time evolution of the star (ZAMS stellar models) and may reveal to be inadequate when applied to advanced stages of the evolution. In addition, the sensitivity of the E_2 to other conditions (i.e. metallicity) has not been studied. Therefore, we computed new values for E_2 based on stellar models with different initial masses, ages, metallicities.

2.2 Expression of the tidal torque coefficient

The complete set of equations to calculate E_n are as follows (Zahn, 1977):

$$E_n = \frac{3^{8/3}[\Gamma(4/3)]^2}{(2n+1)[n(n+1)]^{4/3}} \frac{\rho_f R^3}{M} \left[\frac{R}{g_s} \left(\frac{-gB}{x^2} \right)'_f \right]^{-1/3} H_n^2, \quad (2.4)$$

where Γ is the usual gamma function, f and s refer to the boundary of the convective core and surface, respectively. x denotes the normalized radius coordinate of the star, that is, $x = r/R$. Primed symbols denote derivatives with respect to x , R is the stellar radius, M the stellar mass, g the gravity, and $-gB$ is the square of the Brunt-Väisälä frequency. B is the difference between the actual density gradient and the adiabatic one:

$$B = \frac{d}{dr} \ln \rho - \frac{1}{\Gamma_1} \frac{d}{dr} \ln P, \quad (2.5)$$

where Γ_1 is the adiabatic exponent $\left(\frac{d \ln P}{d \ln \rho} \right)_{ad}$. The coefficient H_n is given by

$$H_n = \frac{1}{X(x_f)Y(1)} \int_0^{x_f} \left[Y'' - \frac{n(n+1)Y}{x^2} \right] X dx, \quad (2.6)$$

where X and Y are found by solving the following second order differential equations:

$$\begin{aligned} X'' - \frac{\rho'}{\rho} X' - \frac{n(n+1)}{x^2} X &= 0, \\ Y'' - 6\left(1 - \frac{\rho}{\bar{\rho}}\right) \frac{Y'}{x} - \left[n(n+1) - 12 \left(1 - \frac{\rho}{\bar{\rho}}\right) \right] \frac{Y}{x^2} &= 0, \end{aligned} \quad (2.7)$$

where $\bar{\rho}$ is the mean density inside the radius r of the star and the primes on X and Y indicate derivatives with respect to x . A fourth-order adaptive stepsize Runge-Kutta method is used to solve the two differential equations for X and Y . We find that the derivative of the Brunt-Väisälä frequency divided by x^2 in Eq. 2.4 is sensitive to the boundary of the convective core. For determining the boundary of the convective cores, which define f and s in Eq. 2.4, we used the Schwarzschild criterion. Overshooting above the Schwarzschild boundary of the convective core is considered with an extension given by $\alpha_p = 0.1 H_p$, where H_p is the pressure scale height estimated at the Schwarzschild boundary limit.

2.3 Solution for X and Y

In order to calculate E_2 , the whole structure of a star is required. Here I briefly describe how Eq. 2.7 is solved, and the detailed solution can be found in Siess, Izzard, Davis, & Deschamps (2013). In the centre of the star, many physical quantities are zero. In order to overcome this difficulty, I briefly introduce how these boundary conditions are given.

2.3.1 Boundary conditions for X

The differential equations of X is given as:

$$x^2 X'' + Ax^2 X' - 6X = 0, \quad (2.8)$$

where $A = -d \ln \rho / dx$. Now we use a series solution for X at the center ($X_0 = X(x_0)$)

$$X = \sum_{m=0}^{\infty} a_m x^{s+m}, \quad (2.9)$$

and the differential equation can be then written as:

$$\begin{aligned} x^2 X'' + Ax^2 X' - 6X &= \sum_{m=0}^{\infty} a_m (m+s)(m+s-1) x^{s+m} \\ &+ A a_m (m+s) x^{s+m+1} \\ &- 6 a_m x^{s+m}. \end{aligned} \quad (2.10)$$

Collecting the term x^s ($m=0$) gives $a_0 s(s-1) - 6a_0 = 0$ hence $s = 3$ or -2 (this value is discarded due to $X \equiv 0$).

The coefficients of the polynomials are given following recursion relation

$$a_{m+1} = \frac{A(m+3)}{6 - (m+3)(m+4)} a_m. \quad (2.11)$$

Now we have the boundary term

$$X_0 = \sum_{m=0}^N a_m x_0^{m+3}. \quad (2.12)$$

The first coefficient a_0 cancels in the final expression of H_n . Here at the center, X_0 and its derivative are not sensitive to the index m (higher terms of N have less important contribution). Therefore, the differential equation can be integrated for small x and then numerically for all $0 < x < 1$.

2.3.2 Boundary conditions for Y

The original definition of Y in Zahn (1970) is given

$$Y = M \frac{x^3}{m(x)} y_1(x), \quad (2.13)$$

where the function $y_1(x) \rightarrow x^3$ and $m(x)$ is the mass coordinate. We rewrite the Y equation

$$\frac{d^2 Y}{dx^2} - \frac{6}{x} \left(1 - \frac{\rho}{\bar{\rho}}\right) \frac{dY}{dx} + 6 \left(1 - 2 \frac{\rho}{\bar{\rho}}\right) \frac{Y}{x^2} = 0. \quad (2.14)$$

It can also be rewritten as $x^2 Y'' + BxY' + CY = 0$, where $B = 6(\rho/\bar{\rho} - 1)$ and $C = 6(1 - 2\rho/\bar{\rho})$. This is an Euler-Cauchy equation that can be exactly solved. We define $x = e^t$, and hence

$$\begin{aligned} xY' &= \frac{dY}{dt}, \\ x^2 Y'' &= \frac{d^2 Y}{dt^2} - \frac{dY}{dt}. \end{aligned} \quad (2.15)$$

Combining them together gives

$$\frac{d^2 Y}{dt^2} + (B - 1) \frac{dY}{dt} + CY = 0. \quad (2.16)$$

Eq. 2.16 is a standard second-order differential equation with the two roots

$$D_{1,2} = \frac{1 - B \pm \sqrt{(B - 1)^2 - 4C}}{2}. \quad (2.17)$$

Now $Y = j_1 e^{D_1 t} + j_2 e^{D_2 t}$ and then

$$Y = j_1 x^{D_1} + j_2 x^{D_2}. \quad (2.18)$$

At the center $x = 0$, $\rho/\bar{\rho} = 1$, hence $B = 0$, $C = -6$, and $D = 3$ (this also agrees with the original definition of Y in Eq. 2.13) or -2 . As the x^{-2} must have zero coefficient, $D = 2$ needs to be discarded, and j_1 will be canceled out in the final expression for H_n . Therefore, we have $Y = j_1 x^3$ at x_0 . Similar to a solution of X , the differential equation Y can be integrated for small x and then numerically for all $0 < x < 1$.

2.4 Results of E_2

Based on the boundary conditions of X and Y , the two differential equations can be numerically integrated for x from 0 to 1.

In Fig. 2.1 we show the evolution of E_2 for a 5 and 10 M_\odot H-rich star at solar metallicity, as computed by the method described above. We compare our results with calculations by Siess, Izzard, Davis, & Deschamps (2013) and Claret & Cunha (1997). As it was pointed out by Zahn (1977), E_2 is sensitive to the exact structure of the star, something which was also confirmed by Claret & Cunha (1997). Different treatments for the boundary of the convective core may lead to slight differences in the size of the convective core, but also, even when using the same physical criterion, the numerical implementation may differ (Gabriel, Noels, Montalbán, & Miglio, 2014). The adopted overshooting parameter α_{ov} , which affects the extent of the convective core, may also be responsible for differences in the evolution of E_2 . Compared with our value of $0.1H_p$, Siess, Izzard, Davis, & Deschamps (2013) used a value for α_{ov} in the range of $0.23-0.3H_p$, while Claret & Cunha (1997) adopted a value of $0.2H_p$.

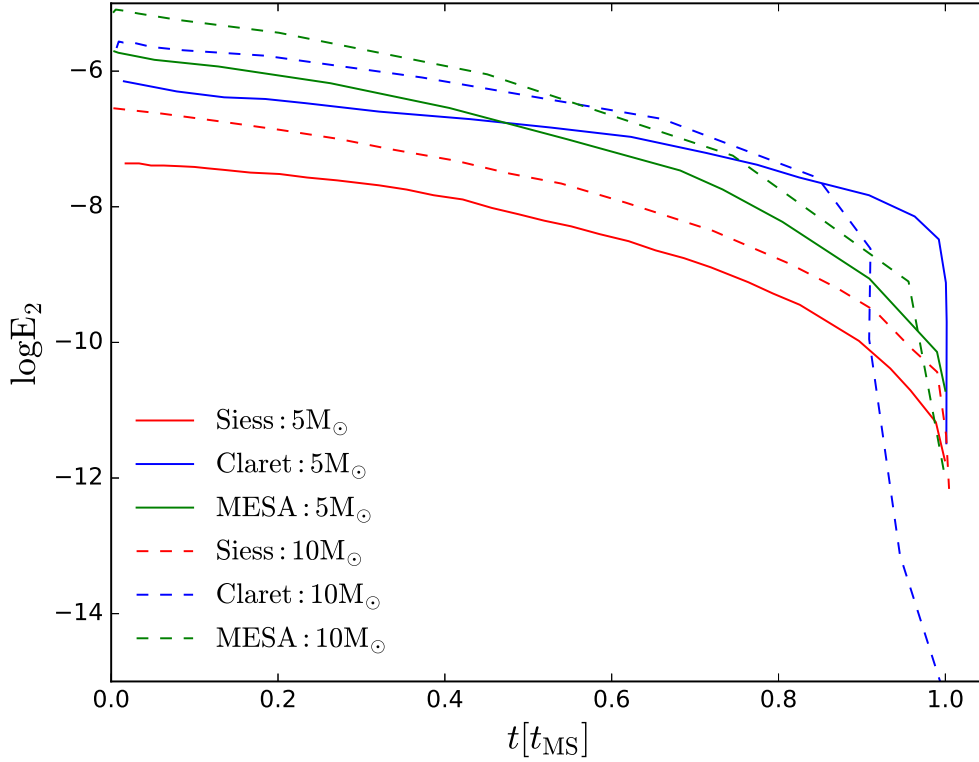


Figure 2.1: Comparison of E_2 coefficients computed by different authors. Solid lines and dashed lines correspond to 5 and 10 M_{\odot} main sequence stars, respectively. Red: Data from Siess, Izzard, Davis, & Deschamps (2013); blue: Data from Claret (2004); green: results from this study.

For stars on the main sequence, E_2 depends strongly on the radius of the convective core R_{conv} . In Fig. 2.2, the relation between E_2 and the ratio of R_{conv} to the total radius of the star is shown for star with masses between 2 and 40 M_{\odot} and for metallicity $Z = 0.01 Z_{\odot}$, $0.1 Z_{\odot}$ and Z_{\odot} . Our estimates of E_2 are offset by about one magnitude above the relation given by Yoon, Woosley, & Langer (2010), but in closer agreement with calculations by Claret & Cunha (1997). Figure 2.2 shows the fitting formulae that can be deduced from our calculations of H-rich stars. We note that for a given initial mass, some points correspond to long time-steps of our stellar evolution code and other points correspond to very short ones. To account for this effect when deriving our fitting formulae, we weight each of the data points by:

$$weight = \frac{dt}{T} * \frac{1}{N}, \quad (2.19)$$

where dt is the time step, N number of the steps and T the lifetime of the star during the core H-burning phase. On each panel corresponding to one specific metallicity, we have used three fitting methods. First, in order to have a comparison with the result of Yoon et al., we fixed the exponent relating E_2 with R_{conv} to 8, and performed

a separate fit for each metallicity. This result is shown by the green solid line in Fig. 2.3. Second, we directly fitted the data allowing for the exponent to vary freely. This is shown as a red dashed line in Fig. 2.3. Third, we fitted the combined data for all metallicities together. This is shown as a cyan dashed line. We find only small differences between the three fitting methods and a negligible dependence on the metallicity. Therefore the same fitting formula is suggested for use across metallicities. For reference, we also provide Yoon et al.’s fitting formula as a black, dashed line.

We have also investigated the relation of E_2 and R_{conv}/R for He-rich stars at different metallicities. The masses of He-rich stars in our investigation cover the range from 4 to 50 M_{\odot} with a mass interval of 2 M_{\odot} . Similarly, the results for He-rich stars are shown in Figs. 2.4 and 2.5. On these figures, we can see some “jumps” in the calculated values of E_2 which are due to the unstable boundary of the convective core. However, the fitting results are not significantly influenced by these jumps when the weights of the data points are considered. Given the insensitivity of our calculations to the metallicity, we again suggest that the same fitting formula should be used for all He-rich stars irrespective of their metallicity.

Ideally, E_2 should be calculated at every time step since its value depends on the structure of the star which evolves as a function of time and also depends on the important physical ingredients that vary from one set of models to another. Hence, it is not advisable to use a published formula without at least checking the conditions that have been used to obtain it.

Here we have established new fitting formulae that correspond to the physics of the present stellar models. We have shown that our fitting formulae differ significantly from the one proposed by Yoon, Woosley, & Langer (2010). The difference comes mainly from the treatment of convective criterion, the boundary of the convective core, as well as the overshooting. We show that the fitting formula below for the H- and He-rich stars are somewhat different; however these formulae do not strongly depend on the metallicity of the star.

$$E_2 = \begin{cases} 10^{-0.42} \left(\frac{R_{\text{conv}}}{R}\right)^{7.5}, & \text{H - rich stars} \\ 10^{-0.93} \left(\frac{R_{\text{conv}}}{R}\right)^{6.7}, & \text{He - rich stars} \end{cases} \quad (2.20)$$

2.5 Conclusion

The tidal interaction in a close binary plays a significant role in the evolution of angular momentum of two components and thus the spin of BH’s progenitor. However, the widely used expressions for E_2 are valid only for ZAMS stellar models at solar metallicity. In this work, we calculated the tidal coefficient E_2 for different evolutionary stages of the stars at different metallicities. New E_2 coefficients have been obtained for both H-rich and He-rich

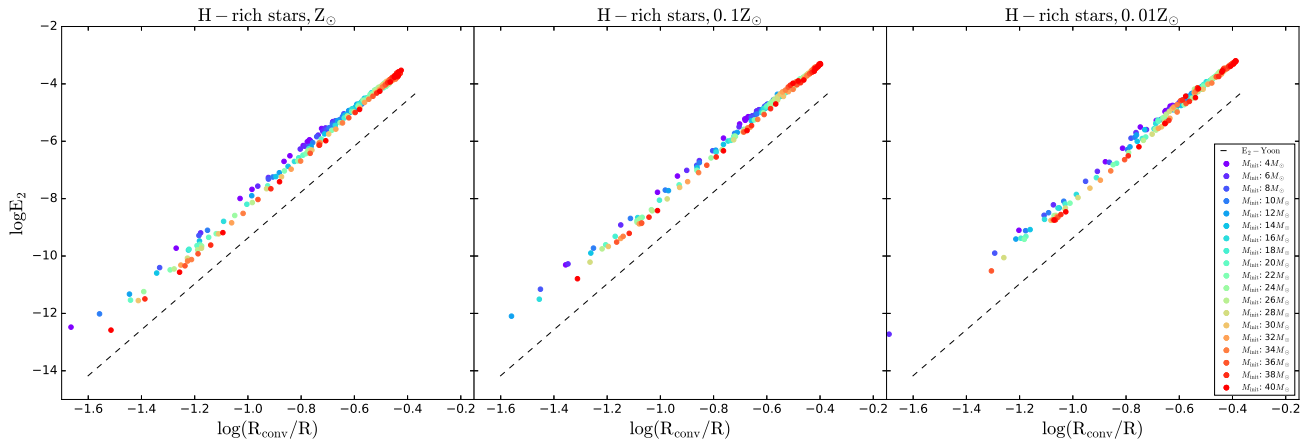


Figure 2.2: E_2 as a function of R_{conv}/R for H-rich stars at different metallicities. The different colors of the points correspond to various masses of the stars. Black dotted line corresponds to the formula from Yoon, Woosley, & Langer (2010). Left panel: Z_{\odot} , middle panel: $0.1 Z_{\odot}$, right panel: $0.01 Z_{\odot}$.

stars. We provided new prescriptions for the tidal coefficient E_2 for both H-rich and the He-rich stars.

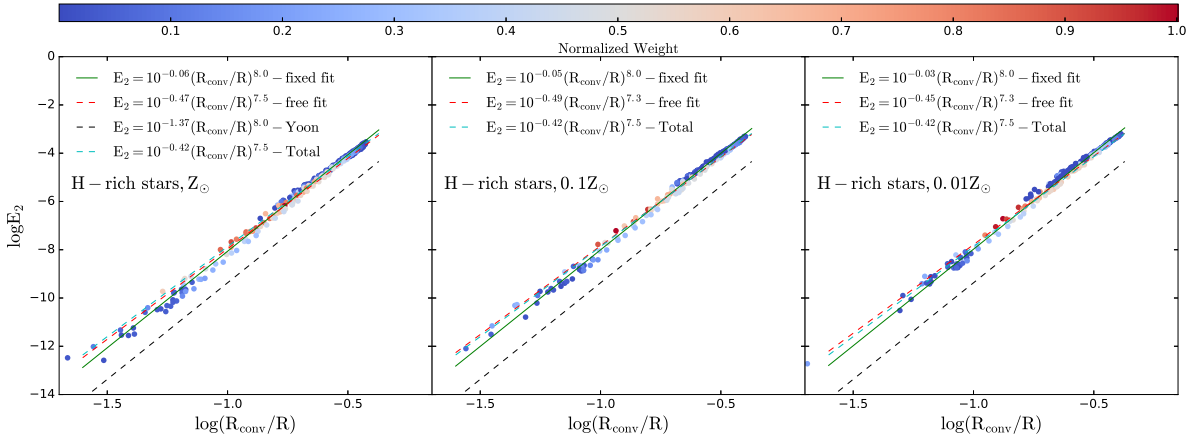


Figure 2.3: E_2 as a function of R_{conv}/R for H-rich stars at different metallicities. Black dotted line corresponds to the formula from Yoon, Woosley, & Langer (2010); red dashed line refers to the free fitting; green solid line refers to the fitting data with the fixed exponent of $R_{\text{conv}}/R = 8.0$, cyan dotted line refers to the fitting data with all three different metallicities. Different color bar points correspond to the weights of E_2 defined in Eq. 2.19. Left panel: Z_{\odot} , middle panel: $0.1 Z_{\odot}$, right panel: $0.01 Z_{\odot}$.

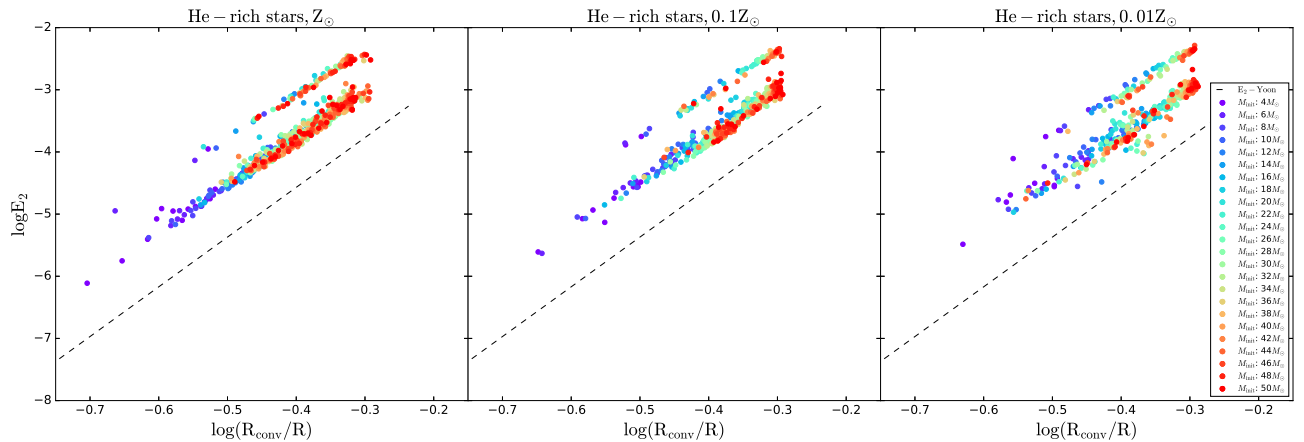


Figure 2.4: As in Fig. 2.2 for He-rich stars.

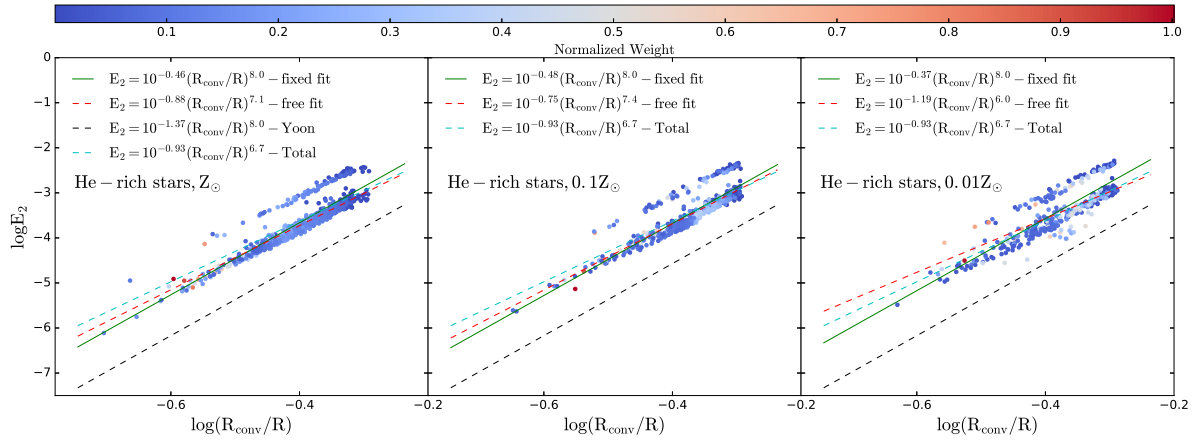


Figure 2.5: As in Fig. 2.3 for He-rich stars.

Chapter 3

The spin of the second-born black hole in coalescing binary black holes

3.1 Introduction

Stellar-mass black holes (BHs) are formed from the gravitational collapse of massive stars ($\geq 20 M_{\odot}$; e.g., Fryer, 1999; Heger et al., 2003; Sukhbold et al., 2016) after they exhaust the nuclear fuel at their centers. Astrophysical BHs can be fully described by only two quantities; their mass, M , and angular momentum \vec{J} . The angular momentum content of a BH is usually described by the dimensionless BH spin parameter

$$\vec{a} = c\vec{J}/GM^2, \quad (3.1)$$

where c is the speed of light in vacuum. Many BHs exist in binary systems with non-degenerate companion stars, for example, X-ray binaries, which makes it possible to obtain the BH's properties indirectly (McClintock, 2006; McClintock, Narayan, & Steiner, 2014; Reynolds, 2014; Casares & Jonker, 2014; Miller & Miller, 2015). Binary systems where both members are BHs can also exist. If the orbital separation of these binary BHs (BBHs) is initially sufficiently small, angular momentum losses due to gravitational wave emission contract their orbit further and can lead to their coalescence within the Hubble time. The existence of such BBHs in the Universe, as a result of the evolution of massive binary stars, was first theorized by Tutukov & Yungelson (1973).

A new window for the study of the BHs has opened with the detection of the first gravitational wave event (Abbott et al., 2016a) by the Advanced Laser Interferometer Gravitational-Wave Observatory (AdLIGO) (LIGO Scientific Collaboration et al., 2015). To date, six gravitational wave events and one high-significance gravitational wave event candidate (Abbott et al., 2016d,e,a, 2017d,a,c) from the merger of BBHs have been detected by AdLIGO. These observations demonstrate that massive stellar BBHs exist and can merge within the Hubble time (Abbott et al., 2016b). The suggested formation channels of these BBHs can be split into two broad categories: (i) Formation via the evolution of massive, isolated binaries in the field, that go through either a common enve-

lope (CE) phase after the formation of the first-born BH that significantly shrinks their orbits (hereafter referred to as the “CE” binary evolution channel (Phinney, 1991; Tutukov & Yungelson, 1993; Belczynski, Holz, Bulik, & O’Shaughnessy, 2016; Tutukov & Cherepashchuk, 2017)), a stable, non-conservative mass-transfer phase (van den Heuvel, Portegies Zwart, & de Mink, 2017; Inayoshi, Hirai, Kinugawa, & Hotokezaka, 2017), or spend their whole lives in close orbits and evolve chemically homogeneously (de Mink & Mandel, 2016; Marchant et al., 2016; Mandel & de Mink, 2016; Song et al., 2016), and (ii) dynamical formation in globular clusters (Sigurdsson & Hernquist, 1993; Rodriguez et al., 2015, 2016) and galactic nuclear clusters (Miller & Lauburg, 2009; O’Leary, Kocsis, & Loeb, 2009; Kocsis & Levin, 2012; Petrovich & Antonini, 2017). Finally, motivated by the existence of a potential electromagnetic counterpart for GW150914 in gamma-rays (Connaughton et al., 2016), a formation channel from a single star, via the fragmentation of their rapidly rotating cores, has been suggested (Loeb, 2016). However, both the applicability of this scenario to GW150914 (Woosley, 2016) and the detection of the electromagnetic counterpart itself (Savchenko et al., 2016; Ackermann et al., 2016) have been questioned.

For the isolated field binary channels, the spins of the two BHs are expected to be mostly aligned with the orbital angular momentum. In contrast, the spins of the two BHs from the dynamical formation channels are expected to have a random, isotropically distributed direction. Clearly the spin plays an important role in distinguishing among the various BBH formation channels (e.g. Abbott et al., 2016b; Farr et al., 2017). The spins of the BHs have an effect on the waveform of the gravitational waves, and this can be observed by AdLIGO. The effective inspiral spin parameter χ_{eff} which can be directly constrained by the gravitational wave signal, is defined in the following expression:

$$\chi_{\text{eff}} \equiv \frac{M_1 \vec{a}_1 + M_2 \vec{a}_2}{M_1 + M_2} \cdot \vec{L}, \quad (3.2)$$

where M_1 and M_2 are the masses of the two BHs, \vec{a}_1 and \vec{a}_2 are two BHs’ dimensionless spin parameters and \vec{L} is the direction of the orbital angular momentum. χ_{eff} has been observed to be $-0.06_{-0.14}^{+0.14}$, $0.21_{-0.1}^{+0.2}$, $-0.12_{-0.30}^{+0.21}$, $0.0_{-0.2}^{+0.3}$, $0.06_{-0.12}^{+0.12}$ and $0.07_{-0.09}^{+0.23}$, for GW150914, GW151226, GW170104, GW170814, LVT151012 and GW170608, respectively (Abbott et al., 2016d,e, 2017d,b,c). From these 6 χ_{eff} measurements, five are consistent with zero and only for GW151226 is χ_{eff} determined to have a positive, non-zero value with a high statistical confidence. Assuming an isotropic prior probability distribution for the misalignment angle between the individual BH spins and the orbit, the individual BH spins of GW170104 have a significant probability of being misaligned with the orbit, supporting the dynamical formation scenario. Alternatively, if the individual BH spin magnitudes are small, then the posterior probability of a misalignment between the individual BH spins with the orbit decreases and the “CE” channel cannot be ruled out (Belczynski et al., 2017).

In all the formation channels that are based on the evolution of an isolated field binary (i.e. the “CE” binary evolution channels and the chemically homogeneous evolution channels), the immediate progenitor of the BBH

is a close binary consisting of a BH and a He-rich star (i.e. WR star). In these binaries, the angular momentum of the progenitor of the second-born BH will be mainly determined by the net effect of the stellar winds and the tidal interaction in a close binary configuration. On the one hand, the outer layer of the He-rich star will be lost through stellar winds with a mass loss rate strongly dependent on the metallicity of the mass-losing He-rich star (e.g. Eldridge & Vink, 2006). At the same time, this mass loss rate can potentially be enhanced if the star is rapidly rotating, approaching critical rotation (Langer, 1997; Maeder & Meynet, 2000a). As a result of the mass and rotational and orbital angular momentum losses due to stellar winds, both the orbital separation and the rotation period of the He-rich star change. Stellar winds tend to increase the rotation period of the mass-losing star. As a result of the mass and angular momentum losses due to stellar winds, both the orbital separation and the rotation period of the He-rich star tend to increase; stellar winds extract both spin angular momentum from the mass-losing star, slowing its rotation, and mass and orbital angular momentum from the system, tending to widen the binary orbit. In addition to these effects, tidal interactions between the BH and the He-rich star may also induce angular momentum exchanges between the orbit and the star. Apart from stellar winds and tides, different initial conditions for the He-rich star at its birth, including initial rotation rate and metallicity, also play a key role in the spin of the second-born BH at its birth.

Following the detection of the first gravitational wave event, GW150914, for which the quantity χ_{eff} of the two coalescing BHs was found to be consistent with zero, several studies attempted to model this last evolutionary phase in the formation of a BBH and derive constraints on the expected spin of the second-born BH, under the assumption that these BBH were formed via the “CE” channel (Kushnir, Zaldarriaga, Kollmeier, & Waldman, 2016; Hotokezaka & Piran, 2017; Zaldarriaga, Kushnir, & Kollmeier, 2018). These studies employed analytic arguments and semi-analytic calculations to infer the angular momentum content of the progenitor of the second-born BH due to tidal interactions with its BH companion. The main conclusion of these studies was that the distribution of the second-born BH is expected to be bi-modal, with approximately half having no spin and half spinning maximally. However, in order to make the problem analytically tractable, in all three studies, several simplifying assumptions had to be made. For example, they used approximate timescales for the process of tidal synchronization that do not take into account changes in the structure of the star during its lifetime. Furthermore, these studies did not self-consistently take into account wind mass-loss which, through tidal coupling, affects the evolution of the orbit and the angular momentum content of the WR star. Hence, it is not obvious that these results will persist when using detailed binary evolution models that self-consistently include the complex interplay between tides, wind mass loss and stellar structure evolution.

Massive He-rich stars are also widely accepted as the progenitors of Type Ib/c supernovae (e.g. Filippenko, 1997; Woosley & Bloom, 2006, and references therein). During the core collapse of a rapidly rotating He-rich

star, its outer layers may form an accretion disk along with a highly relativistic jet around the newly formed BH resulting in the release of intense Gamma-ray radiation. According to this paradigm, also known as the collapsar model (Woosley, 1993), massive, rapidly rotating He-rich stars are the progenitors of long Gamma-Ray Bursts (IGRBs). In this context, the tidal spin-up of a He-rich star from a compact companion in a close binary system has been investigated in several studies (Brown et al., 2000; Izzard, Ramirez-Ruiz, & Tout, 2004; Petrovic, Langer, & van der Hucht, 2005; Cantiello, Yoon, Langer, & Livio, 2007; van den Heuvel & Yoon, 2007; Detmers, Langer, Podsiadlowski, & Izzard, 2008; Eldridge, Izzard, & Tout, 2008). Angular momentum can be transferred through the L-S coupling effect from the orbit to the He-rich star, but the orbital period needs to be sufficiently short to allow for a strong tidal interaction. Transferred angular momentum from the orbit to the outer layers of the He-rich star will spin up its core by various coupling effects such as toroidal magnetic fields generated from differentially rotating, radiative stellar envelopes (Spruit, 1999, 2002).

In this chapter, we focus on the later phases of the “CE” BBH formation channel and specifically on the evolution of a close binary system consisting of a He-rich star and a BH, immediately after the binary detaches at the end of the “CE” phase. Our results are relevant for all BBH formation channels based on the evolution of an isolated field binary. We investigate the angular momentum content of the second-born BH progenitor, using detailed stellar structure and binary evolution calculations that take into account the effects of internal differential rotation in the He-rich star, stellar winds, and tides. In order to better understand the interplay of these effects, we explore a five-dimensional initial parameter space of initial masses of the two binary components, initial orbital period, initial rotation of the He-rich star and metallicity.

This chapter is organized as follows. In §3.2, we present qualitative arguments about the expected spin of the first-born BH in the “CE” isolated binary evolution channel. We then introduce the theory of tidal interaction adopted in this study in §3.3. In §3.4, we show a semi-analytic test for the efficiency of tides in WR-BH binaries. In §3.5, we present detailed simulations of the angular momentum evolution of He-rich stars in close binary systems. In §3.6 we discuss the merging timescale of the two compact objects. Finally, discussion and conclusions of our results are given in §3.7 and §3.8, respectively.

3.2 The spin of the first-born BH in the classical isolated binary evolution channel

In the “CE” isolated field binary formation channel (e.g., see Belczynski, Holz, Bulik, & O’Shaughnessy, 2016), a binary consisting of two massive H-rich stars in a wide orbit evolve from Zero Age Main Sequence (ZAMS). The more massive star (star 1) evolves faster and fills its Roche lobe during either the Hertzsprung gap or the supergiant phase. Star 1 transfers mass to the less massive star (star 2) through the first Lagrangian point, and the mass transfer (MT) during this phase is stable. After losing all its H envelope, star 1 evolves into a He star and

soon directly collapses to form a BH (the first-born BH), while star 2, which has accreted part of star 1's envelope, still remains on the MS. At this point, the orbital separation has increased further, mainly due to MT. Subsequently, star 2 evolves off the main sequence and overfills its Roche lobe while on the red supergiant branch. Because of the mass ratio and the evolutionary stage of star 2, this MT phase is dynamically unstable and the binary enters into a CE phase. The BH spirals into the envelope of star 2, converting orbital energy into heat. During this phase the orbital separation shrinks dramatically, and the post-CE system consists of a He star and a BH in a close orbit of tens of solar radii. Eventually star 2 also collapses to form a BH, and potential asymmetries in the core collapse may alter the orbit further. The final product of this formation channel is a BBH in an orbit that is close enough to lead to the coalescence of the two BHs due to angular momentum losses from gravitational wave emission.

In this scenario, the spin of the first-born BH is expected to be very low ($a_{*,1} \sim 0$) for two reasons. First, while the progenitor of star 1 evolves through a red supergiant phase (assuming an efficient angular momentum transport mechanism such as the Taylor-Spruit dynamo; Spruit, 1999, 2002), most of the initial angular momentum is transported to the outer layers of the star upon expansion. The core of the star, although still rotating at a higher angular frequency than the envelope, is depleted of angular momentum. Eventually, the outer layer of the red supergiant star is removed either by the MT phase or by stellar winds, and thus the remaining angular momentum in the core of the star will be small. Second, before the onset of the MT phase, the orbital separation is relatively large. Therefore, even if tides can efficiently synchronize the rotation of the outer layers of the star to the orbit, the angular frequency of the latter will be so low that it will not be possible to actually spin up the core. A similar argument has been presented by Fragos & McClintock (2015) about the natal spin of BHs in Galactic low-mass X-ray binaries.

We note that in Yoon, Woosley, & Langer (2010), detailed binary evolution has been computed for primary stars between 12 and 25 M_{\odot} . Their results are not directly applicable here since we are studying the progenitor of the BH rather than neutron star. Progenitors of BHs likely come from more massive stars. However, it is interesting to mention that they find that the amount of angular momentum that remains in the core of the primary is very similar to the one obtained from the single stellar models (Heger, Woosley, & Spruit, 2005; Yoon, Langer, & Norman, 2006). Therefore, in order to obtain a more quantitative handling on the arguments presented above and in the mass regime that leads to BH formation, we evolved, using the Modules for Experiments in Stellar Astrophysics (**MESA**) code version 8118 (Paxton et al., 2011, 2013, 2015, 2018), single massive stars of 50 M_{\odot} and 90 M_{\odot} at metallicities of 0.01 Z_{\odot} , 0.1 Z_{\odot} and Z_{\odot} (Z_{\odot} is the solar metallicity taken here as 0.02). For each mass and metallicity, we evolve the stars from ZAMS, assuming different initial rotation rates (i.e. 0.1, 0.3, 0.5, 0.7 and 0.9 $\Omega_{\text{init}}/\Omega_{\text{crit}}$; where Ω_{init} and Ω_{crit} are the initial and the critical angular velocity at the surface of the star), where we assume that the stars are, initially, uniformly rotating. For this set of single H-rich models, we use stellar winds, mixing and angular

momentum transport parameters closely following Marchant et al. (2016). We also use the Schwarzschild criterion to treat the boundary of the convective zones and a convective core overshooting parametrized with $\alpha_{ov} = 0.1$. The impact of rotation on the mass-loss rate is considered as indicated in Eq. 3.3 (Heger & Langer, 1998; Langer, 1998).

$$\dot{M}(\Omega) = \dot{M}(0) \left(\frac{1}{1 - \Omega/\Omega_{\text{crit}}} \right)^\xi, \quad (3.3)$$

where Ω and Ω_{crit} ($\Omega_{\text{crit}}^2 = (1 - L/L_{\text{Edd}})GM/R^3$, L_{Edd} is the Eddington luminosity) are the angular velocity and critical angular velocity at the surface, respectively. The default value of the exponent $\xi = 0.43$ is taken from Langer (1998). No gravity darkening effect is accounted for (see Maeder & Meynet, 2000a, for a discussion on the impact of this process). More details about our settings in **MESA** for the single H-rich stars can be found on the **MESA** web page ¹.

We run all the models up to central He exhaustion. The spin of the BH is obtained assuming that its mass and angular momentum content are given by the mass and angular momentum of the carbon-oxygen core at that stage. The final spin obtained as indicated above is shown in Fig. 3.1 as the function of the initial relative rotation rate at ZAMS. We find that for initial rotations up to $0.5 \Omega_{\text{init}}/\Omega_{\text{crit}}$ and for all metallicities, the spin of the resultant BH is negligible ($a_* \leq 0.1$). Although Fig. 3.1 shows that stars with initial relative rotations above $0.5 \Omega_{\text{init}}/\Omega_{\text{crit}}$ and metallicities $\leq 0.1 Z_\odot$ produce near maximally spinning BHs, the fast-spinning nature of these He-star progenitors induces efficient internal mixing, forcing chemically homogeneous evolution; these stars never evolve onto the supergiant branch, and therefore they cannot be progenitors of the first-born BH in the ‘‘CE’’ formation scenario we consider here. Overall, we expect, as a first-order approximation, that the first-born BH in the ‘‘CE’’, isolated field binary formation channel has negligible spin.

The latter argument is even more convincing when accounting for two effects that we have neglected in this approach and that would remove angular momentum from the star. First, in this approach we considered that the star evolves as a single star, while it is a member of a binary system. As recalled above, in a close binary, the more massive star loses angular momentum through the first Lagrangian point during the stable MT phase, and its angular momentum content decreases. Second, we have neglected the effects of disk formation during the core collapse process (e.g., see discussion in Sect. 2.2 of Belczynski et al., 2017) which may remove some angular momentum from the core that collapses to form the BH. The latter effect is also relevant for the estimate of the spin of the second-born BH that we discuss later. In that sense our quoted spins can be considered as upper limits for the predicted BH spin.

¹The detailed list of parameters used for the single H-rich stars can be found at <http://MESAstar.org/results>.

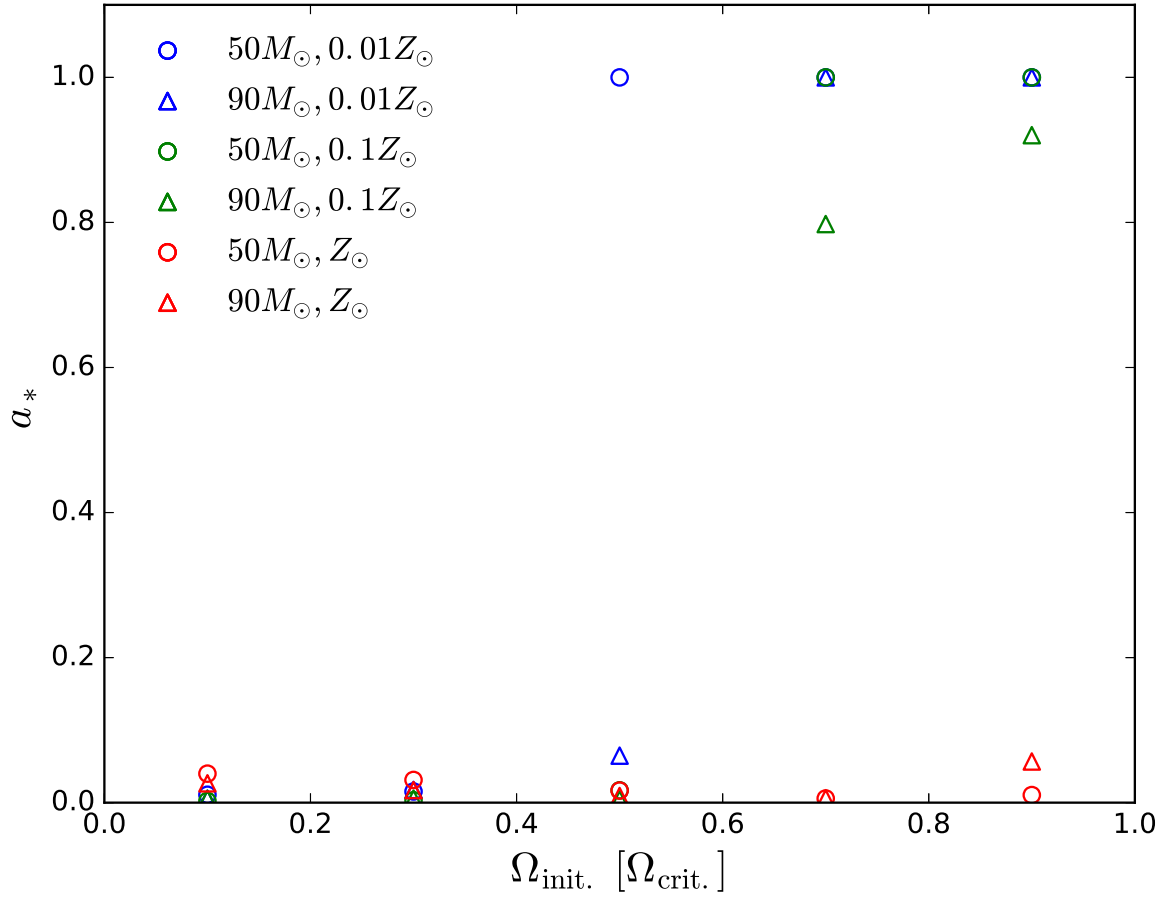


Figure 3.1: The spin of the resultant BH from the evolution of single stars at central He exhaustion for different masses ($50 M_{\odot}$ and $90 M_{\odot}$) and metallicities ($0.01 Z_{\odot}$, $0.1 Z_{\odot}$, and Z_{\odot}) as a function of initial rotation, assuming that the carbon/oxygen core will collapse to form the BH, conserving the angular momentum it had at the point of central He exhaustion.

3.3 Tidal interaction in binary systems

Tidal forces, in a close binary system, play a key role in both secular evolution of the orbit and the internal angular momentum of the stellar components. Two main mechanisms responsible for the dissipation of the tidal kinetic energy have been widely accepted, that is, turbulent dissipation (or convective damping) on the equilibrium tides applied to the stars with an outer convection zone, and radiative damping on the dynamical tides applied to the stars with an outer radiative zone (Zahn, 1977). The strength of the interaction depends on the ratio of the stellar radius to the orbital separation of the two stars, and the timescale of synchronization is defined as follows (Zahn, 1977; Hut, 1981):

$$\frac{1}{T_{\text{sync}}} = -\frac{1}{\Omega - n} \frac{d\Omega}{dt} = 3 \cdot \frac{K}{T} \frac{q^2}{r_g^2} \left(\frac{R}{a}\right)^6, \quad (3.4)$$

where Ω and n are the spin angular velocity and the orbital angular velocity, respectively, q is the mass ratio of the secondary star to the primary one, a the orbital separation, r_g^2 is the dimensionless gyration radius of the star², and $\frac{K}{T}$, a coupling parameter depending on the tidal interaction mechanism, which we describe in the following section.

3.3.1 Equilibrium tides

For stars with an outer convective envelope, the turbulent viscosity on the equilibrium tides in the convective regions of a star is responsible for the dissipation of the tidal kinetic energy. In equilibrium tides, it is assumed that the star keeps the state of hydrostatic equilibrium, and all other dissipation processes are neglected. $\left(\frac{K}{T}\right)_c$ is expressed (see Hurley, Tout, & Pols, 2002, and references therein) as:

$$\left(\frac{K}{T}\right)_c = \frac{2}{21} \frac{f_{\text{conv}}}{\tau_{\text{conv}}} \frac{M_{\text{env}}}{M} \text{yr}^{-1}, \quad (3.5)$$

where f_{conv} is a numerical factor, τ_{conv} (in unit of year) the eddy turnover timescale (Rasio, Tout, Lubow, & Livio, 1996), and M_{env} the mass of the convective envelope.

3.3.2 Dynamical tides

For stars with outer radiative envelopes, radiative damping of the stellar oscillations is responsible for the dissipation of the tidal kinetic energy. This is also known as the regime of dynamical tides. In this regime $\left(\frac{K}{T}\right)_r$ is defined as:

$$\left(\frac{K}{T}\right)_r = \left(\frac{GM}{R^3}\right)^{1/2} (1+q)^{5/6} E_2 \left(\frac{R}{a}\right)^{5/2}, \quad (3.6)$$

where E_2 (second order tidal coefficient, with higher orders being neglected) is a parameter that depends on the structure of the star and refers to the coupling between the tidal potential and gravity mode oscillations.

² $r_g^2 = \frac{I}{MR^2}$, where I is the moment of inertia of the star, M the mass of the star, R the radius of the star.

One widely used analytic approximation formula produced by Hurley, Tout, & Pols (2002), based on tabulated results from Zahn (1975), expresses E_2 as a function of the stellar mass:

$$E_2 = 1.592 \times 10^{-9} \left(\frac{M}{M_\odot} \right)^{2.84}. \quad (3.7)$$

More recently Yoon, Woosley, & Langer (2010) obtained the following expression:

$$E_2 = 10^{-1.37} \left(\frac{R_{\text{conv}}}{R} \right)^8, \quad (3.8)$$

by fitting the dependence of E_2 on R_{conv}/R , using the values given in Table 1 of Zahn (1977) for ZAMS stars with various masses.

There, R_{conv} denotes the radius of the convective core and R is the radius of the star. The latter expression relates E_2 to the radius of the convective star and therefore is more sensitive to the structure of the star. This formulation has been successfully implemented in several recent, detailed studies of rotation in massive stars (de Mink et al., 2009; Song et al., 2013, 2018).

The original methodology to calculate E_2 was introduced by Zahn (1975), and was discussed in more detail in later works (Claret & Cunha, 1997; Siess, Izzard, Davis, & Deschamps, 2013; Kushnir, Zaldarriaga, Kollmeier, & Waldman, 2017). Since both fitting formulae in Eqs. 3.7 and 3.8 for E_2 were calculated based on ZAMS, H-rich stellar models at solar metallicity, it is not obvious that they accurately represent He-rich stars over a variety of metallicities. We therefore decided to systematically investigate the dependence of E_2 , for both H-rich and He-rich stars, over a range of metallicities (i.e. $0.01 Z_\odot$, $0.1 Z_\odot$ and Z_\odot) and evolutionary stages.

For all the simulations of He-rich stars, we first create a naked He star at different masses. After that, with the same settings (i.e. stellar winds, rotational mixing parameters, Schwarzschild criterion for convection and overshooting with $\alpha_{ov} = 0.1$) as with H-rich stars in §2, we compute the evolution of He-rich stars at different metallicities up to the central He exhaustion. The physical ingredients of the models used to compute E_2 are also the same as those used to compute the evolution of the He-rich stars in binary systems³. Appendix A provides the details of our method for calculating E_2 as well as a brief discussion.

In all cases, a functional form similar to the one adopted by Yoon et al. provides an adequate analytic approximation:

$$E_2 = \begin{cases} 10^{-0.42} \left(\frac{R_{\text{conv}}}{R} \right)^{7.5}, & \text{H-rich stars} \\ 10^{-0.93} \left(\frac{R_{\text{conv}}}{R} \right)^{6.7}, & \text{He-rich stars} \end{cases} \quad (3.9)$$

³The detailed list of parameters used for creation and the evolution of single He-rich stellar models can be found at <http://MESASTAR.org/results>.

This updated relation is used in the expression for dynamical tides in the present work.

We note here that for fast rotating stars, it has been suggested that a high level of turbulence produced by rotation dominates over the radiative viscosity and therefore equilibrium tides should be used despite the lack of an outer convective zone (Toledano et al., 2007; Detmers, Langer, Podsiadlowski, & Izzard, 2008). In the following section, we test for the relative efficiency of equilibrium tides and dynamical tides in He-rich stars with radiative envelopes. However, we adopt the standard dynamical tides in all the detailed models that are presented on Sect. 5 and onward.

3.4 Testing the efficiency of the tides in WR-BH binary systems

Due to the large dimensionality of the available initial parameter space of WR-BH and WR-neutron star (NS) binaries (initial masses of the two binary components, initial orbital period, initial rotation of the He-rich star, and metallicity), it is computationally impractical to cover sufficiently densely the whole available parameter space. Knowing that tides play an important role only in close binary systems, we first perform an order-of-magnitude test to identify the part of the parameter space where tides become relevant. We use **MESA** to evolve single He-rich stars with different metallicities, in the mass range 4 - 50 M_{\odot} and steps of 2 M_{\odot} . The stellar structure information of these He-rich star models is used to calculate the tidal timescale of the synchronization with different compact object companions. For He-rich stars, the newly derived expression for E_2 from Eq.3.9 is adopted in the following calculations. Furthermore, we assume that a binary system has a He-rich star either with a BH of 10 or 30 M_{\odot} or a NS of 1.4 M_{\odot} . Finally, we consider different initial orbital periods, P , spanning the range from 0.1 to 10 days. For each binary system, the Roche lobe radius, r_L , of the He-rich star provides a lower limit of the orbital period, as initially the He-rich star cannot overflow its Roche lobe, where r_L is given in units of the orbital separation by (Eggleton, 1983):

$$r_L = \frac{0.49q^{-2/3}}{0.6q^{-2/3} + \ln(1 + q^{-1/3})}a, \quad 0 < q < \infty, \quad (3.10)$$

where q is the mass ratio of the companion compact object to the He-rich star and a the orbital separation. He-rich stars spend most of their lifetimes burning He in the core. We adopt the properties of the star half-way through its central He burning phase to calculate the synchronization timescale, T_{sync} . The ratio of the synchronization timescale to the lifetime of the core He burning phase, T_{He} , gives us a good handle on whether tides play a significant role in this binary configuration or not. In this approximation, we assume that the orbital separation remains constant during the whole evolution. In other words, we neglect the effects of stellar winds and spin-orbit angular momentum exchange.

The ratio $T_{\text{sync}}/T_{\text{He}}$ as a function of initial orbital period and the initial He-rich star mass, for three different companion masses (1.4, 10 and 30 M_{\odot}) is shown in Fig. 3.2. The color of the outer circle and inner dot of each

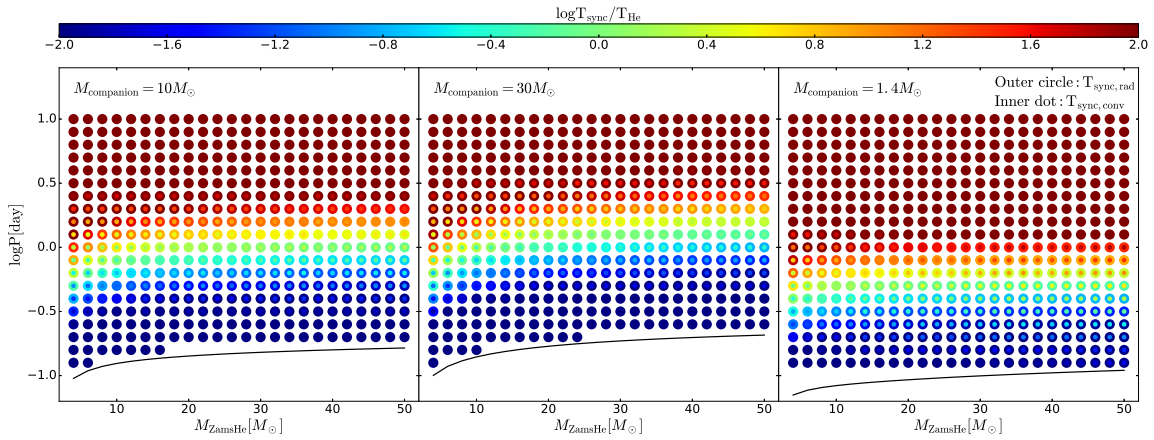


Figure 3.2: The ratio of $T_{\text{sync}}/T_{\text{He}}$ as a function of the He-rich star initial mass and orbital period. Left panel: $10 M_{\odot}$ BH as the companion, middle panel: $30 M_{\odot}$ BH as the companion, right panel: $1.4 M_{\odot}$ NS as the companion. Outer circle: $T_{\text{sync}}/T_{\text{He}}$ for dynamical tides, inner dot: $T_{\text{sync}}/T_{\text{He}}$ for equilibrium tides. The selected stellar structure profile for the calculation of T_{sync} refers to the stage when the central mass fractional He abundance is 0.5. The black line denotes the lower limit in orbital period, below which a He-rich star of a given mass would overflow its Roche lobe at ZAHems (Zero Age He Main Sequence: the time when a He star starts to burn He in the core, which is analogous to ZAMS for core H burning). The metallicity of the He-rich star models shown in this figure is $0.01 Z_{\odot}$, but the dependence of $T_{\text{sync}}/T_{\text{He}}$ on metallicity is very weak. Therefore, two similar figures corresponding to the He-rich stars at $0.1 Z_{\odot}$ and Z_{\odot} are not shown here.

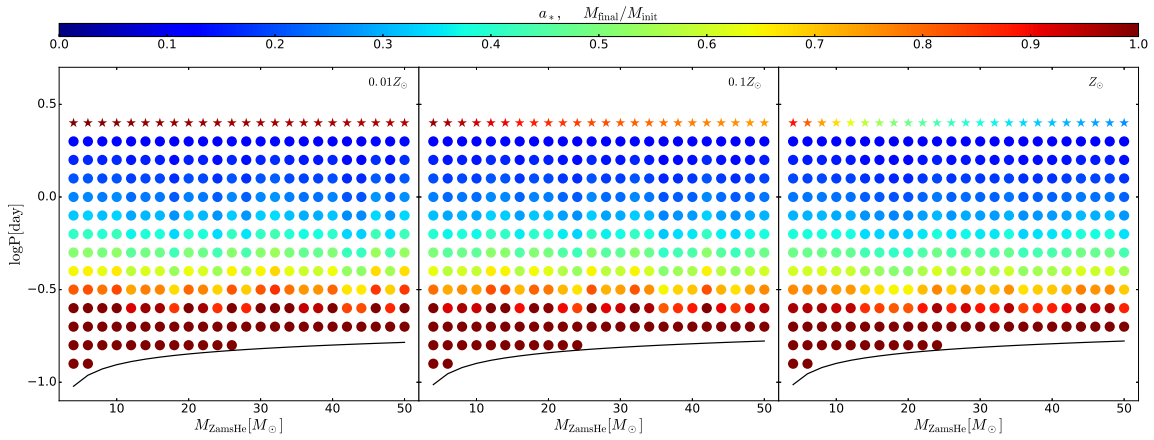


Figure 3.3: Approximate estimate of the dimensionless spin a_* of the resultant BH as a function of the He-rich initial mass and orbital period, denoted by the color of the filled circles. The star symbols, sharing the same color bar with a_* , refer to the ratio of the He-rich star’s mass at the central carbon exhaustion to its initial mass, i.e. $M_{\text{final}}/M_{\text{init}}$. For a given initial mass of the He-rich star, this quantity remains the same whatever the orbital period because in this estimation, stars are evolving as if they were single stars. Left panel: $0.01 Z_{\odot}$, middle panel: $0.1 Z_{\odot}$, right panel: Z_{\odot} . In these approximate estimates, the mass of the BH companion is assumed to be $10 M_{\odot}$, while the orbital separation is assumed to remain constant. We also assume that tides instantaneously synchronize the spin of the He-rich star with the orbital angular velocity. The solid black line denotes the lower limit in orbital period, below which a He-rich star at a given specific mass would overflow its Roche lobe at ZAHems.

symbol corresponds to the T_{sync} estimated based on dynamical tides and equilibrium tides, respectively. Blue dots and circles correspond to systems in which tidal forces are expected to be relevant, while red dots and circles correspond to systems in which tides are likely to play a minor role in the binary's evolution.

Most importantly, we find that the strong dependence of the synchronization timescale on the ratio of stellar radius to orbital separation ($T_{\text{sync}} \propto (R/a)^{-6}$) is the dominant factor, while the binary mass ratio and the exact dissipation mechanism is of less importance. Examining Fig. 3.2, it is safe to say that for WR-BH and WR-NS binaries with orbital periods above ~ 2 days, tides are not relevant, while binaries with periods below ~ 0.3 days are expected to have He-rich stars with spins synchronized with the orbit. We note that in this approximation we find that metallicity has a negligible effect on T_{sync} . The results for He-rich stars at higher metallicities ($0.1 Z_{\odot}$ and Z_{\odot}) are almost identical and are therefore not shown in the paper. Based on these estimates, we decided to limit the parameter space of initial orbital periods for which, below, we perform detailed calculations (see following sections) to below 2 days.

Stellar winds, scaled with metallicity, can greatly influence the final mass of the star, and this is clearly shown in Fig. 3.3. The three panels correspond to He-rich stars at $0.01 Z_{\odot}$, $0.1 Z_{\odot}$ and Z_{\odot} , respectively. The color of the filled circles denotes the spin of the resultant BH. In this figure, the dimensionless spin a_* is calculated based on the assumption that the He-rich star at the central He exhaustion still has enough mass to directly collapse to form a BH, and that the He-rich star is a solid body fully synchronized with the orbit. The color of the star symbols at the top of each panel refers to the ratio of the final to the initial He-rich mass. He-rich stars lose ≥ 3 times more mass at solar metallicity compared with $0.01 Z_{\odot}$.

From this figure, we see that for orbital periods below 2 days, the whole range of dimensionless spins (from 0 to 1) is covered. Fast-spinning BH's are obtained only for short period systems, typically below 0.3 days. For orbital periods above about 1 day, BH spins are small, and for intermediate orbital period moderately spinning BH's are produced.

These numerical experiments, however, suffer from strong limitations. Principally, we assume that the orbital separation remains constant and that synchronization is instantaneous. In the following section, we compute more sophisticated models where the effects of tides and of stellar winds on stellar rotation and orbital evolution are consistently accounted for. Through tidal coupling, changes in the orbit and the stellar rotation then impact the He-star's evolution.

3.5 Rotation of the second-born black hole

Now that we have gained a qualitative understanding of which physical processes are important for binaries with different initial conditions and we have significantly limited the relevant part of the parameter space, we can go

ahead and calculate grids of detailed calculations of close binaries consisting of a WR star and a compact object. The evolution of the binary is computed using the **MESA** code. The computation accounts for tidal coupling between the orbit and the He-rich star. Since the He-rich star has a radiative envelope, only the dynamical tide is considered. We assume that there is no MT between the He-rich star and the BH, which is assumed to be a point mass. More details about the computations can be found on the **MESA** web page ⁴.

The initial conditions explored are the masses M_1 and M_2 of the two binary components, the initial rotation and metallicity of the WR star and the initial orbital period. For the He-rich stars, we cover the mass range from 4 to 48 M_\odot with steps of 4 M_\odot and the mass of the companion is assumed to be a NS of 1.4 M_\odot or a BH of 10 or 30 M_\odot . The initial orbital periods are between 0.2 and 2 days. Below 0.2 days, the He-rich star overfills its Roche lobe at the onset of He burning, while for initial orbital periods above 2 days we showed in the previous section that tides are not important. Three metallicities (0.01 Z_\odot , 0.1 Z_\odot and Z_\odot) are considered. Finally, the following initial rotations for the He-rich stars have been chosen: zero rotation, angular velocity equal to the orbital angular velocity and 90% of the critical angular velocity at the surface. The formation of almost critically spinning helium stars is not expected in the “CE” formation channel. We include these models here for completeness, as the conclusions derived from these initially highly helium stars are relevant for the chemically homogeneous channel.

In Fig. 3.4, we show the spin a_* of the second-born BH as a function of the He-rich star’s mass and the orbital period for a metallicity $Z = 0.01 Z_\odot$. Figures 5 and 6 present the corresponding trends for metallicities 0.1 and 1.0 Z_\odot , respectively. In each figure, the three columns correspond to the different initial angular velocities of the He-rich star, i.e., $\Omega_{\text{init}} = 0$, $\Omega_{\text{init}} = \Omega_{\text{init,orb}}$ and $\Omega_{\text{init}} = 0.9 \Omega_{\text{crit}}$. The three rows correspond to the different masses of the compact object companion, i.e., 1.4, 10 and 30 M_\odot .

3.5.1 Dependence of orbital evolution and He-star rotation on different binary properties

Before describing the results, let us reiterate a few general trends: first tides tend to equalize the rotation period of the star and the orbital period. This effect implies that when the star has a relatively longer rotation period (or a slower rotation rate) compared with the orbital period, tides tend to transfer angular momentum from the orbit to the star spinning it up, and the orbit shrinks. On the contrary, when the spin period of the star is shorter than the orbital one, angular momentum is transferred from the star to the orbit. Consequently, the star spins down, the orbit widens and the orbital period increases. Second, mass loss has counteracting effects. On the one hand, it decreases the mass of one component, and therefore its gravitational attraction, which widens the orbit. On the other hand, it removes orbital angular momentum, shrinking the orbit. Under standard assumptions of “fast” stellar winds the overall effect is the expansion of the orbit. Mass loss also removes spin angular momentum from the star tending

⁴Detailed setting can be found at <http://MESAstar.org/results>.

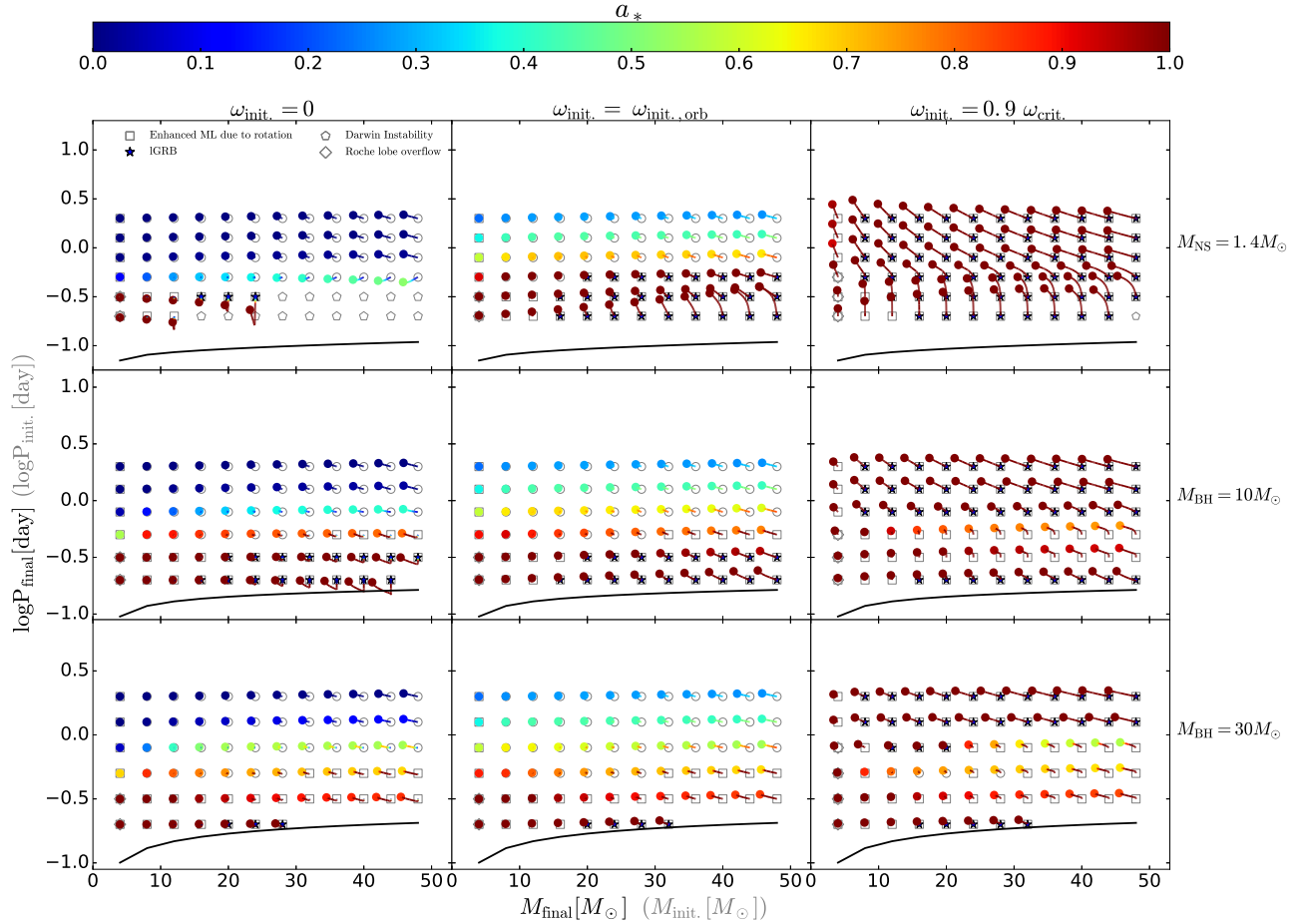


Figure 3.4: Spin parameter a_* (see the color bar at the top) as a function of the orbital period and masses of the He-rich stars. The metallicity of all He-rich stars is $0.01 Z_\odot$. The gray symbols indicate the initial conditions and the color symbols indicate the final ones. The colored lines linking these two symbols show the evolution of the binary. The color along the line gives a_* along the evolution. Black solid lines refer to the lower limit of the orbital period. At that limit, the He-rich star fills its Roche lobe at the beginning of the core He burning phase. Square: models for which rotation increases the mass lost by 10% with respect to the mass lost by non-rotating models; pentagon: Darwin instability; star: IGRB; Diamond: He-rich star starts to fill its Roche lobe. The three columns correspond to different initial velocities of the He-rich stars and the three rows correspond to different masses for the companion. All the He-rich stars have a metallicity equal to $0.01 Z_\odot$.

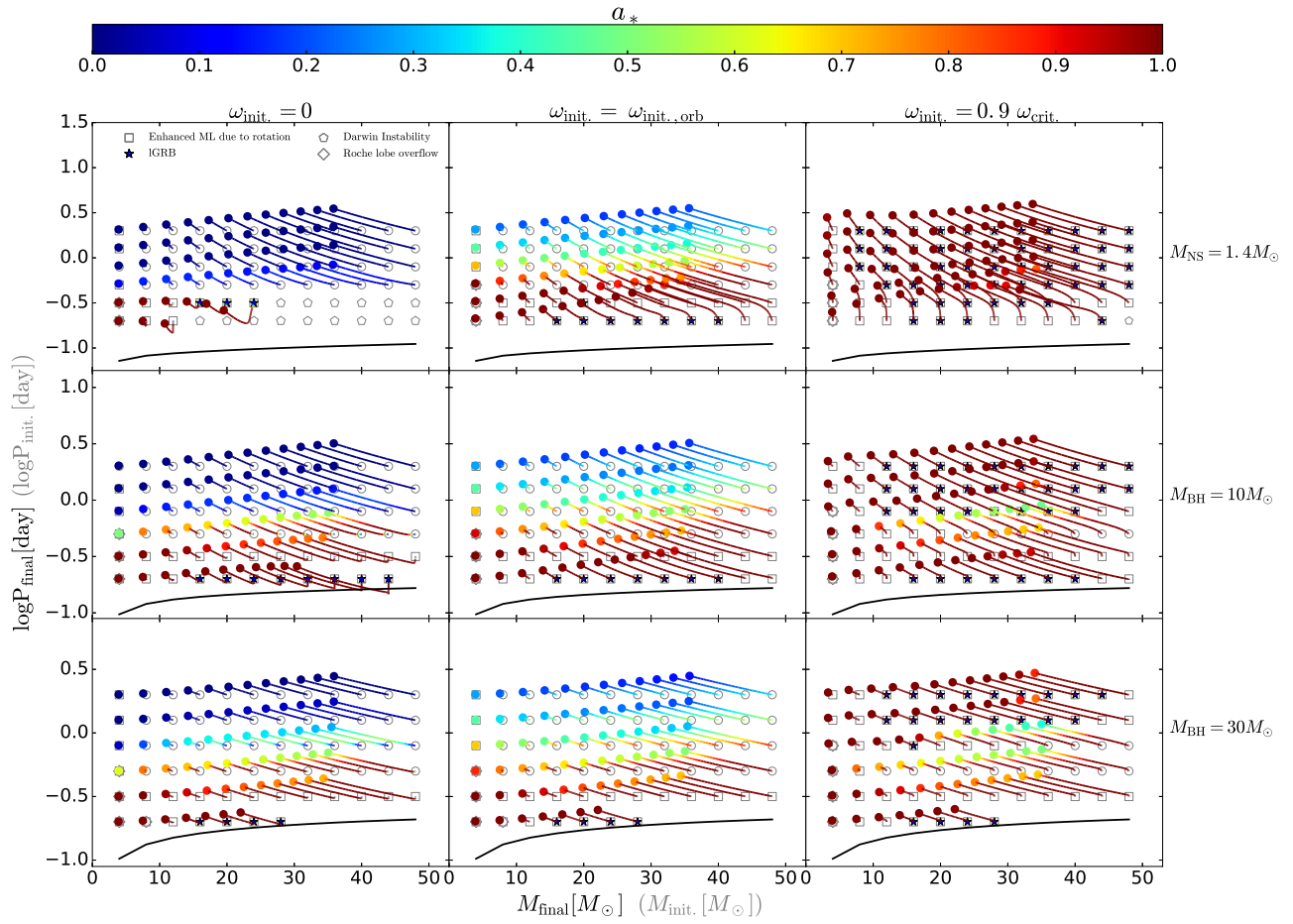
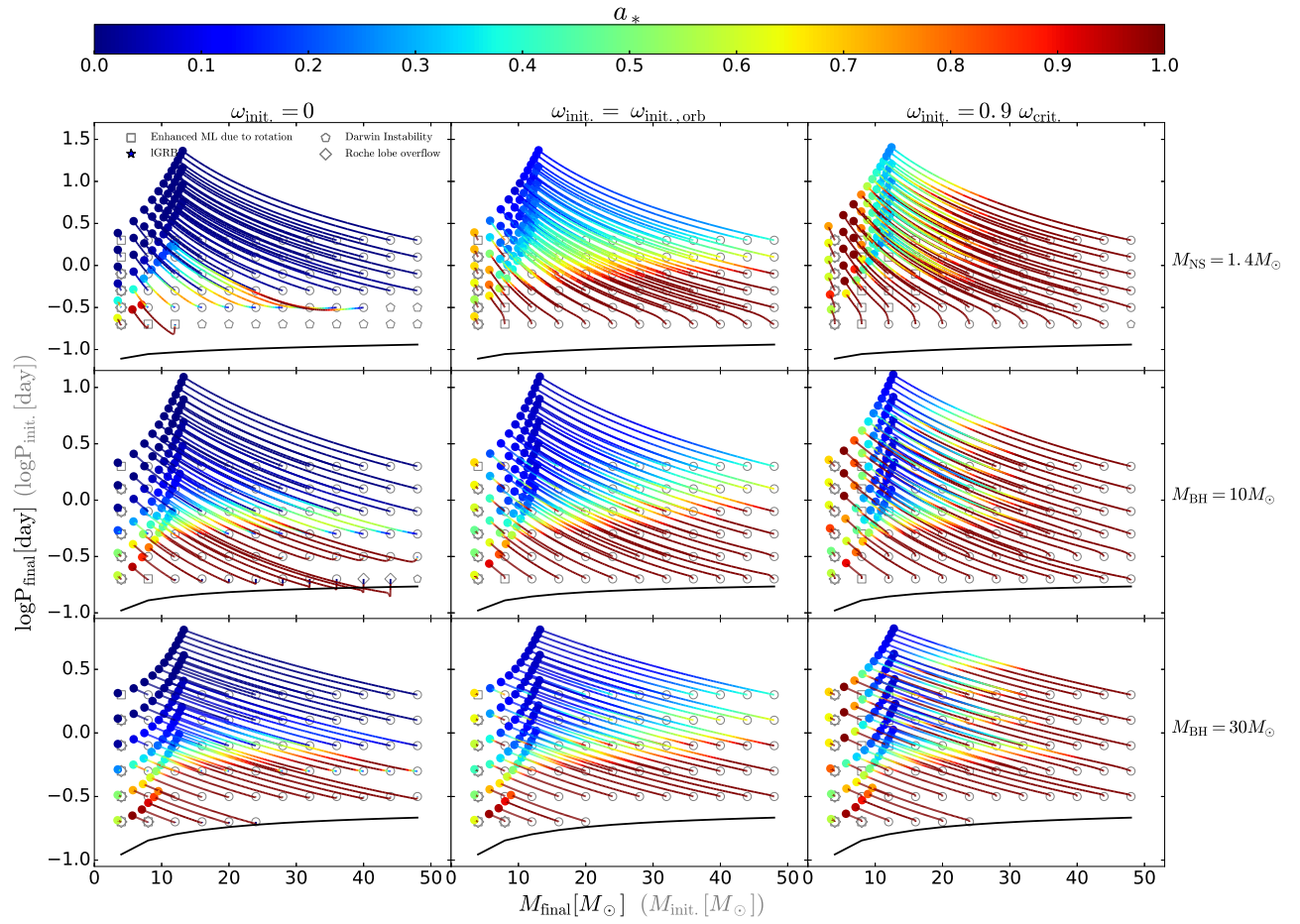


Figure 3.5: As in Fig. 3.4, but for the metallicity $Z = 0.1 Z_{\odot}$.


 Figure 3.6: As in Fig. 3.4, but for the metallicity $Z = Z_{\odot}$.

to spin down the star. For systems near spin-orbit synchronization, this implies that tides will spin up the primary by transferring angular momentum from the orbit to the star. This also tends to shrink the orbit.

In addition to mass loss, structural changes of the star as a function of time modify the tidal interaction and therefore contribute to modifying the orbit as well. As may be guessed from this discussion, it is not easy, without performing detailed calculations, to estimate the evolution of such systems. Depending on which effect dominates, the angular momentum of the He-rich star may increase or decrease.

Dependence on initial orbital period

Let us begin by describing the upper-left panel of Fig. 3.4. Tides are weak at large orbital periods. Therefore, no spin-up occurs (starting with a low rotation implies that tides can only spin up the primary) and the final spin of the He-rich star and of the resulting BH remain low. For higher masses, mass loss slightly decreases the mass and widens the orbit, hence the evolution towards the upper left in the period-mass plane.

At an orbital period of around half a day ($\log P \approx -0.3$), tides become important and spin up the He-rich star. In this case however, the synchronization timescale is still comparable to or longer than the He-star lifetime and therefore the binary never quite reaches a state of synchronization. Instead, the final rotation of the WR star is somewhere between its initial value and the one corresponding to the orbital angular velocity. The final spin of the BH is between 0 and 0.5.

At still smaller orbital periods, tides are efficient enough to make the He-star rapidly reach a rotation rate that is equal to the angular orbital velocity. At the same time, the angular momentum that is transferred from the orbit to the star in order to spin it up results in the initial shrinkage of the orbit. This phase corresponds to the nearly vertically downward evolution. This initial synchronization phase is short and hence mass losses have no time to significantly change the mass of the binary. The orbital period decreases because angular momentum is transferred from the orbit to the star. Once synchronization is reached, the rotation of the primary is maintained near the synchronized value by the tidal interaction. The orbit widens again because the mass-loss term dominates the tidal one in the evolution of the orbital distance.

Dependence on initial rotation of the He star

Let us now see how the results change when higher initial rotations are considered (see the upper-middle panel in Fig. 3.4 which shows the case when the initial rotation of the He-rich star is synchronized with the orbit). We see that starting from a higher initial rotation rate for the He-rich stars produces faster-rotating BHs in the end. Black hole spins are found in the range between 0.3 and 1.0. We also see that the orbital period always increases, and therefore the orbit becomes wider. For the large orbital periods, for which tides are weak, this is an effect of mass loss that decreases the mutual attraction between the two bodies and thus widens the orbit. The star's spin is slightly

slowed down, too, due to mass loss (one sees that the beginning of the line has a colour corresponding to a higher rotation than its end). More interestingly, and in contrast with the results for initially non-rotating He-rich stars, we see that even for small initial orbital periods the orbital period increases. Since here we start from synchronization, tides do not initially transfer a significant amount of angular momentum from the orbit to the stars, and therefore from the beginning of the evolution the effect of mass loss dominates. Tides counteract the spin down of the star due to mass loss and allow the star to maintain a fast rotation.

Further increasing the initial velocity up to 90% of the critical one (see the upper-right panel), produces only fast rotating BHs for all the initial conditions explored in this plot. In that case, spins of the BHs are always near 1.0. The evolution always tends to increase the orbital period. This widening of the orbit results, as before, from mass loss. For shorter periods though, where tides are efficient, it may also come from the fact that the tides, before synchronization, slow down the star and thus transfer angular momentum from the star to the orbit causing it to widen.

Dependence on the mass of the compact-object binary companion

Let us now see how the results change when the mass of the compact object is varied. If we consider systems where the orbital periods are kept fixed, increasing the mass of the compact object increases the orbital separation a (a varies as $(1 + q)^{1/3}$). On the other hand the quantity $1/T_{\text{sync}}$ varies as $q^2/(1 + q)^2$ and therefore increases when the mass ratio increases. This indicates that the tides at a given orbital period are stronger (despite the increase of the distance) when the mass of the compact object is larger.

For the case of low initial rotation (compare the left-middle panel to the left-upper one in Fig. 3.4), and considering a fixed initial orbital period and mass for the He-rich star, increasing the mass of the compact object more efficiently spins up the He-rich star and thus produces fast spinning BHs starting from longer initial orbital periods.

Comparing now the bottom-left panel with the middle-left one, that is, passing from a 10 to a 30 M_{\odot} BH, increases the spin of the second-born BH for longer periods, but slightly decreases the spin for the shorter ones. This appears to be slightly counter-intuitive at first, since one would expect that increasing the BH mass would always more efficiently spin up the He-rich star. However, as we increase the mass of the compact object companion, from 1.4 M_{\odot} all the way to 30 M_{\odot} , the ratio of the spin angular momentum of the He-rich star to the orbital angular momentum, in a state of synchronization, decreases. This means that a smaller fraction of the orbital angular momentum has to be transferred to the He-rich star to spin it up from an initially low rotation to synchronization, and therefore the orbit will shrink less in the initial phase until the system is brought into synchronization. To highlight this effect, let us consider the case of a 48 M_{\odot} He-rich star with a 10 M_{\odot} BH and an initial orbital period of 0.3 days ($\log P = -0.5$). Initially, due to the evolution towards synchronization, the orbit shrinks. This produces the small evolution downwards (a bit to the left because of the mass loss). After the binary reaches synchronization,

the orbit widens again due to the effects of mass loss. For more massive compact-object companions, this initial phase towards synchronization leads to a negligible shrinking of the orbit, as a much smaller fraction of the orbital angular momentum needs to be transferred to the He-rich star, and as a result the final orbital period of the binary is longer at the point of carbon exhaustion.

Despite the slightly shorter final orbital periods for higher-mass compact-object companions, if we compare the final spins of the resulting second-born BHs, we see that the final spins decrease with increasing companion mass, going from a value near 1 for the smallest mass companion to a value near 0.8 for the most massive one. What is the explanation for this trend? This behavior is due to the fact that at the very end of the core He-burning phase, the entire star quickly contracts. This contraction de-synchronizes the star from the orbit since the contraction timescale is shorter than the tidal timescale. After the contraction, the star is spinning faster than the orbit, with tides acting to slow down the star. The more massive the companion is, the stronger the tidal coupling, and therefore also the more efficient the spin down. We note that this fast contraction also occurs for He-rich stars in systems with larger orbital periods. However, in these systems the loss of spin angular momentum due to stellar winds throughout the evolution of the He-star is not compensated by tides, which are too weak. When the star contracts at the end of the core He-burning phase, it has too little angular momentum to reach large spins.

When one starts from a configuration where the binary is synchronized, increasing the mass of the compact-object companion has two effects at short orbital periods (compare the panels in the middle column in Fig. 3.4). Firstly, it decreases the widening of the orbit, and secondly it tends to produce slower rotating BHs in the regions where tides are important. The latter effect is explained above, while the former results from the two counteracting effects of the mass loss. On the one hand, mass loss spins down the He-rich star and forces tides to continuously transfer angular momentum from the orbit to the star. On the other hand it reduces the mass of the He-rich star and tends to widen the orbit. The net effect, that is, the widening of the orbit, remains the same when the mass of the compact object increases. However, since in the case of a higher-mass compact-object companion, a smaller fraction of the total binary mass is lost in winds, the overall expansion of the orbit is smaller. As a reminder, under the assumption that the mass lost is carrying the specific angular momentum of the mass-losing star (Jeans mass loss), the ratio of the final to the initial orbital separation is inversely proportional to the ratio of the final to the initial total binary mass ($a_{\text{final}}/a_{\text{initial}}=M_{\text{binary,initial}}/M_{\text{binary,final}}$).

Starting with still higher initial rotations for the He-rich stars (see the right column in Fig. 4) produces, in general, faster-rotating BHs. We note the same behavior as for the cases shown in the middle column, namely that increasing the mass of the compact remnant produces smaller rotations of BH in some initial mass and period ranges.

Dependence on the metallicity of the He star

When the metallicity increases (see Fig. 5 and 6), the same qualitative behaviors are obtained but the effect of mass loss dominates the evolution in almost all cases. In the period-mass diagrams, stronger mass losses bring the star to smaller final masses and longer orbital periods. At solar metallicity, even when starting with a high initial rotation for the He-rich star, most of the cases studied here end with slowly rotating BHs. The only exception is for the least massive He-rich stars considered here, for which the mass loss is much less important.

Summarizing the effects of different initial properties on the evolution of the binary

These computations show how the effects of mass loss and tides impact the final spin of the second-born compact object. The following results have been obtained:

- Independent of the initial rotation of the He-rich star and its metallicity, fast spin at the end of the evolution ($a_* > 0.9$) is obtained for short orbital systems, below about 0.3 days, and for initial masses below about $30 M_\odot$. In those systems, tides are the key players in determining the final spin.
- For orbital periods above about 0.3 days and at low metallicities, the initial rotation of the He-rich star is the main factor impacting the final spin. The faster the initial rotation is, the faster the final BH spin.
- For orbital periods above about 0.3 days and at solar metallicity, stellar winds have a major impact on the final rotation for stars with masses above about $25 M_\odot$. Mass losses in these cases efficiently slow down the He-rich star and modest final spins are obtained.
- The mass of the compact-object companion only has an impact in cases where tides are sufficiently strong, that is, for orbital periods below about 1 day. In general, a more massive companion produces a smaller final spin. This comes from the fact that when the star contracts at the end of the core He-burning phase, and therefore spins faster and faster, tides tend to slow it down. The more massive the compact-object companion is, the more efficiently the He star slows down.

As was already envisioned from the order-of-magnitude estimates presented in Sect. 4, the whole range of final spins can be reached for a given He-rich star at low metallicity depending on the initial orbital period and rotation (the mass of the compact object has little influence on the range of values that can be reached). At solar metallicity and for the most massive stars, this statement is no longer true. For these stars, only low spin parameters are obtained independently of the initial orbital period, the initial rotation or the mass of the companion.

3.5.2 Mass loss enhanced by rotation

Squares in Figs. 4, 5, and 6 indicate rotating models in which the total mass lost is more than 1.1 times the total mass lost by the corresponding model without rotation. At low initial rotation and for $Z=0.01 Z_{\odot}$, squares appear for small orbital periods, that is, for those cases where tides are efficient enough to spin-up the star. For faster initial rotation, squares, cover a larger zone of the period-mass diagram.

Comparing models with binary component masses, metallicity and initial rotation, but with different initial orbital periods, where in some cases the stars experience enhanced mass loss while in others they do not we see that the final He-rich star masses are not significantly different. Therefore, we infer that these enhancements in mass loss should also have little effects on the final rotation as well as the orbital evolution.

3.5.3 Systems with mass transfer

Diamonds indicate those systems encountering the Roche limit during their evolution. Only models with initial $M_{\text{ZAHemS}} = 4 M_{\odot}$ and initial orbital periods of 0.5 days or less, overflow their Roche lobes. This is because low-mass He-rich stars ($\leq 4 M_{\odot}$) expand towards the end of their evolution.

However, since this mass transfer occurs at the very end of the evolution, the effects on the evolution of the binary and the final angular momentum of the second-born BH progenitor are negligible. We performed tests where we compared results obtained with and without accounting for this mass transfer and the differences concerning the spin of the second-born BH are very small. We therefore conclude that this effect is negligible.

3.5.4 The Darwin instability

Pentagons indicate that a Darwin instability is encountered. This occurs only for the tightest systems and for those systems with an initial low rotation except for one case (systems with a $1.4 M_{\odot}$ NS with an initial rotation $0.9\Omega_{\text{crit}}$ for all the metallicities considered here). This instability requires that a large amount of the orbital angular momentum be transferred into the spin angular momentum of the He-rich star. Obviously this can only occur for tight systems because only tides can transfer angular momentum between the orbital and the spin angular momentum reservoirs. The transfer from the orbital to the spin reservoir is the most efficient when the difference between the low spin and the high orbital spin is the greatest, meaning those cases that start from a low initial rotation rate. The conditions are more favorable for low-mass compact stars because the orbital angular momentums in these systems are the lowest.

The domain where the Darwin instability is reached disappears at high initial rotations. This is because when one starts from a high rotation, tides tend to slow down the star and thus to transfer angular momentum from the star to the orbit making the system evolve away from the conditions needed for this instability to occur. There is however, as already indicated above, one exception: systems with a $1.4 M_{\odot}$ NS and an initial rotation of $0.9\Omega_{\text{crit}}$.

In this case, from the beginning of the evolution, the spin angular momentum of the star is larger than one third of the orbital angular momentum. This is therefore not an evolutionary effect but is rather due to the initial binary configuration.

3.5.5 The long gamma ray bursts

He-rich stars that are potential progenitors of IGRBs are shown by a star in Figs 4, 5 and 6. According to the collapsar model, IGRBs are formed on the condition that enough kinetic energy is available to launch a jet during the core collapse from massive stars (Woosley, 1993). In this work, we follow the procedure suggested in Yoon, Langer, & Norman (2006) to decide whether the collapse of the core would produce a IGRB or not. More specifically, a IGRB is produced if any part of the carbon/oxygen core has a specific angular momentum larger than the one at the last stable orbit j_{LSO} around a black hole with a mass equal to the enclosed mass of the specific shell (Bardeen, Press, & Teukolsky, 1972; Novikov & Thorne, 1973; Cantiello, Yoon, Langer, & Livio, 2007; Detmers, Langer, Podsiadlowski, & Izzard, 2008; Wu, Hou, & Lei, 2013).

At $Z=0.01 Z_{\odot}$, and for low initial rotation periods (see upper left panel of Fig. 4), the domain of the IGRBs is relatively limited to the most extreme cases, that is, those suffering the strongest tidal interactions while not encountering the Darwin instability. Models with an overly low initial mass produce a neutron star and are therefore discarded as possible progenitors of IGRBs. The conditions favorable for IGRBs in the period-mass diagram are in general more extended in the case of faster initial rotations. This is expected since the reservoir of spin angular momentum is larger. Looking at the middle and right columns of Fig. 4, we also note that the domain for IGRB reduces when the mass of the compact object increases. Also, in the case, for instance, of a $30 M_{\odot}$ BH, the most favorable cases are in the upper and lower parts of the orbital range considered here. When the metallicity increases, the extent of the initial parameter space leading to IGRBs generally reduces and nearly completely disappears at solar metallicity.

Overall, we see that the most favorable conditions for obtaining IGRBs from close binary systems are a high initial rotation for the He-rich star, a low-mass compact-object companion and a low metallicity.

3.6 Merging timescales and comparisons with observed merging systems

After the second-born BH forms, gravitational wave (GW) emission removes angular momentum from the orbit of the two compact objects, shrinking it, and eventually leading to the merger of the two compact objects. The timescale for the merger of a binary compact object due to GWs is given by (Peters, 1964)

$$T_{\text{merger}} = \frac{5}{512} \frac{c^5}{G^3 M^3} \frac{2q^{-2}}{1+q^{-1}} a^4, \quad (3.11)$$

where M is the mass of the second-born BH, q the mass ratio of the companion to the second-born BH and a is the orbital separation. In Fig. 3.7, the color bar indicates T_{merger} due to GW emission assuming that the He-rich star at

the end of its evolution can collapse directly to form a BH. Figures 8 and 9 are similar to Fig. 3.7, but correspond to metallicities of $0.1 Z_{\odot}$ and Z_{\odot} , respectively. When the merging timescale is for instance equal to 10% the age of the Universe, and assuming that the merger of this binary is observed today in the local universe (i.e. $z_{\text{observed}} \sim 0$), this binary compact object must have formed at redshift $z_{\text{formation}} = 0.103^5$. In all these three figures, black triangles refer to the systems whose merging timescale is longer than the Hubble time ($\sim 13.8 \text{ Gyr}$).

The initial orbital separation a , or the initial orbital period, is the most important factor in determining T_{merger} ($T_{\text{merger}} \propto a^4$). The mass of the He-rich star is also an important parameter. Decreasing the mass of the He-rich star, and keeping all other parameters equal, makes the merging timescale longer ($T_{\text{merger}} \propto M^{-3}$). Due to this dependence on orbital period and the mass of the He-rich stars, merging timescales shorter than the Hubble time are obtained for small initial orbital periods and/or massive He-rich stars. At high metallicity (Fig. 9), one can see clearly that the upper limit of the initial orbital period below which merging timescales are inferior to the Hubble time increases when the mass of the compact companion increases. This also occurs for the lower metallicities but is less apparent in the figures. This is a rather obvious consequence of the fact that increasing the mass of the compact remnant implies stronger tides and therefore shorter final orbital periods. One also notes that at high metallicity, decreasing the initial mass of the He-rich star, starting from a given initial orbital period, decreases the merging timescale. This is likely due to the fact that lower-mass He-rich stars lose less mass by stellar winds. This in turn implies less widening of the orbit and thus stronger tidal forces.

Interestingly we find that, generally, the shortest merging timescales are obtained for those systems that predict fast-rotating BHs. Indeed, systems in which the second-born BH is spun up or keeps a high rotation rate are those in which the tides are the strongest, which in turns translates to the shortest merging timescales. From the discussion in sect. 2, the main contribution to χ_{eff} (see Eq. 2) is from the spin a_* of the second-born BH. χ_{eff} therefore decreases when the merging timescale increases. In other words, systems with small observed values of χ_{eff} have a larger merging timescale, which can be seen in Fig. 3.10. Finally, this trend implies that merging systems with a low χ_{eff} are formed at high redshifts.

An anti-correlation between χ_{eff} and the merging timescale was already predicted by the analytic models of Kushnir, Zaldarriaga, Kollmeier, & Waldman (2016) and Zaldarriaga, Kushnir, & Kollmeier (2018). However, our detailed calculations show that this anti-correlation is both more complex and weaker, as the relation of merging timescale to χ_{eff} is also a function of the masses of the two binary components and the metallicity of the He-rich stars. It is interesting to see, in Fig. 3.10, how χ_{eff} varies with the chirp mass and the merging timescale. The chirp

⁵In this paper, we adopt the standard spatially flat Λ CDM cosmology with Hubble constant $H_0 = 67.8 \text{ km s}^{-1} \text{ Mpc}^{-1}$, a matter density parameter $\Omega_m = 0.308$, and vacuum density parameter $\Omega_{\Lambda} = 0.692$ (Planck Collaboration et al., 2016), to calculate the redshift corresponding to the timescale of merger events.

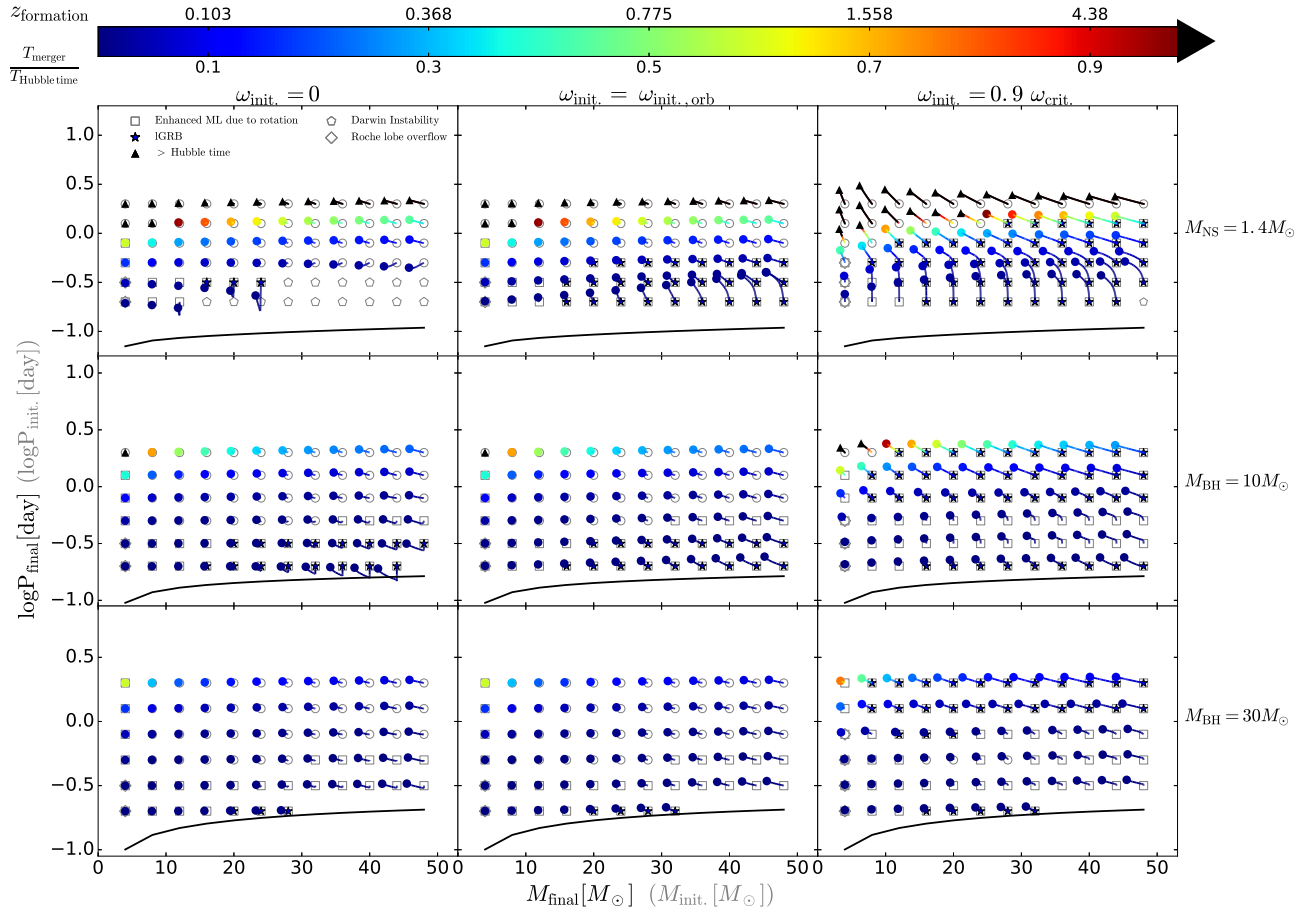


Figure 3.7: As in Fig. 3.4, but the color bar refers to the merger timescale of the two compact objects due to gravitational wave emissions. Black triangles refer to the systems whose merger timescales are longer than the present age of the Universe (~ 13.8 Gyr). $z_{\text{formation}}$ refers to the redshift of the formation of the binary compact object, assuming that the merger took place at redshift ~ 0 and adopting the standard cosmological parameters (Planck Collaboration et al., 2016).

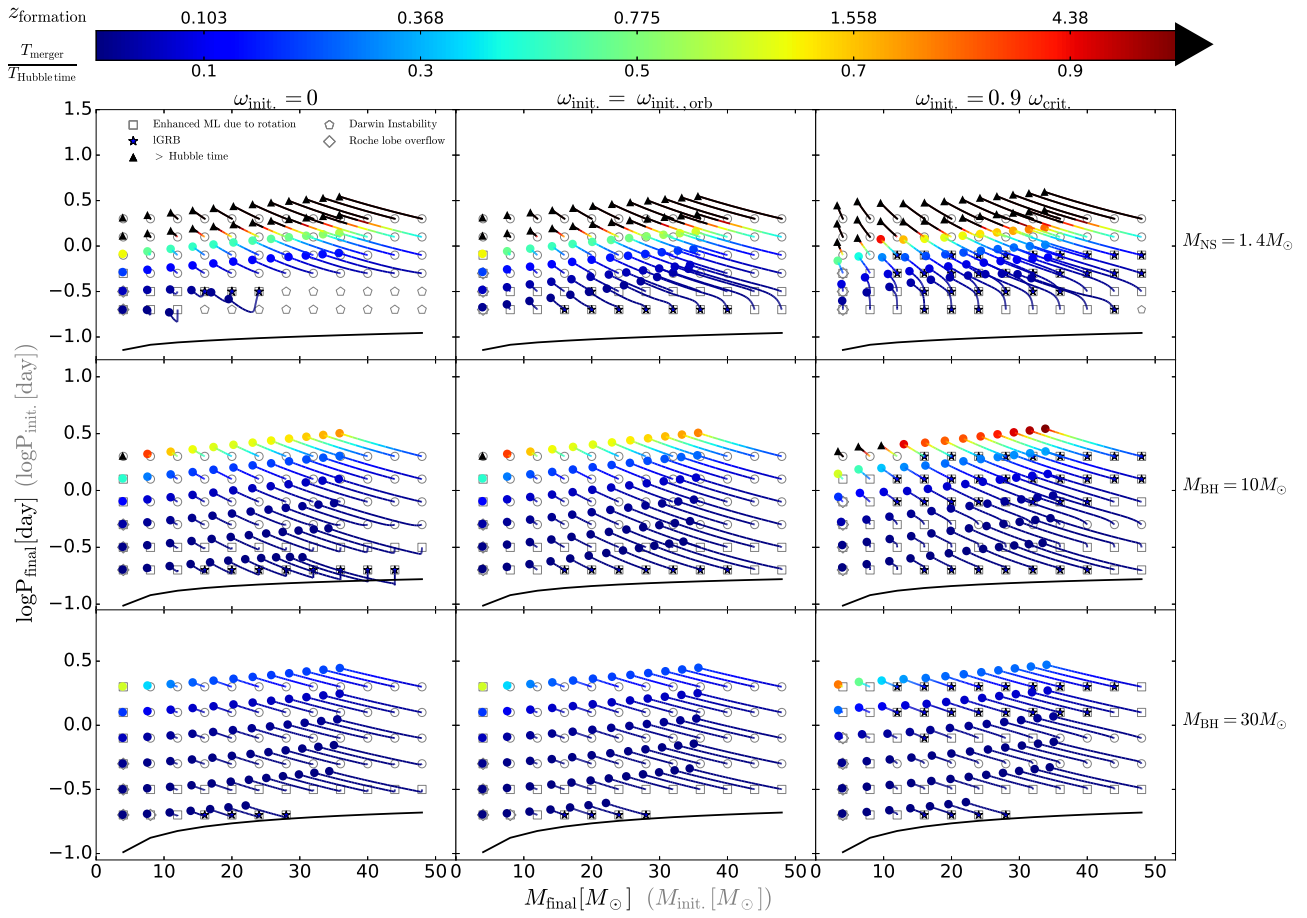
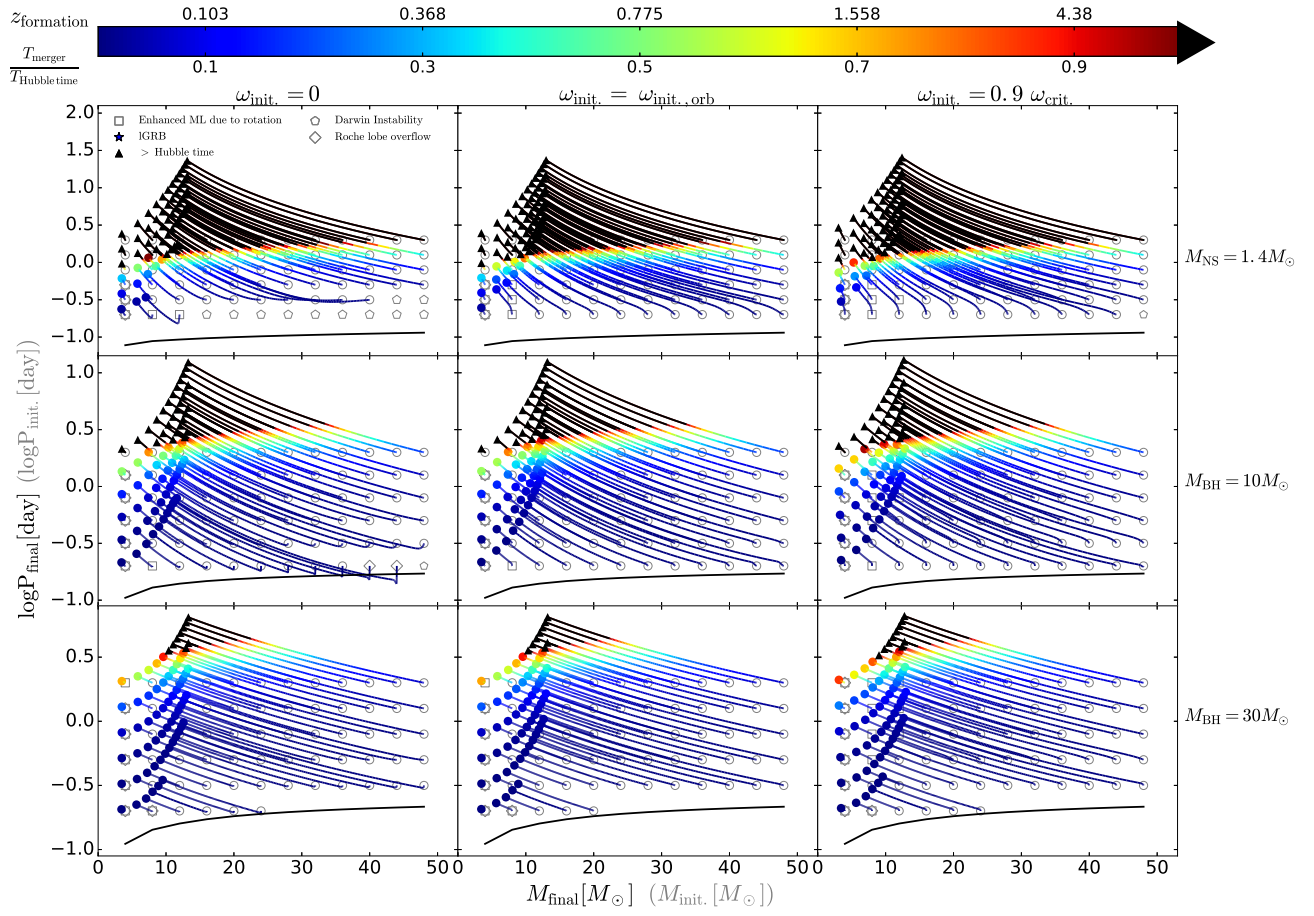


Figure 3.8: As in Fig. 3.7, but for the metallicity $Z = 0.1 Z_{\odot}$.


 Figure 3.9: As in Fig. 3.7, but for the metallicity $Z = Z_{\odot}$.

mass, M_{chirp} , is defined by

$$M_{\text{chirp}} = \frac{(m_1 m_2)^{3/5}}{(m_1 + m_2)^{1/5}}, \quad (3.12)$$

where m_1 and m_2 are the masses of the two BHs, respectively. Consistently with the discussion in Sect. 2, we have calculated χ_{eff} assuming that the spin of the first-born BH is 0. A few interesting points can be noted. First, at solar metallicity, there is no possibility to produce chirp masses larger than about 17-18 M_{\odot} , even assuming that the first-born BH is $30M_{\odot}$, which is unrealistic. In contrast, at low metallicities, provided the mass of the first born BH is high enough, there is no difficulty in producing chirp masses up to values around 30 M_{\odot} .

As already underlined above, high χ_{eff} values are obtained only for short merging timescales. At low metallicities, it is easier to form BBHs with higher values of χ_{eff} . At the same time, these BBHs will likely have higher chirp masses, as the lower metallicity results in weaker wind mass-loss and larger overall final compact-object masses (e.g., Belczynski et al., 2010). However, low-metallicity star-formation environments are more common at high redshift (e.g., Zahid et al., 2014). The combination of these correlations implies that BBHs with high χ_{eff} and M_{chirp} values have formed at high redshift (i.e., high $z_{\text{formation}}$), but given their inferred short merging timescales, they have also merged at high redshift (i.e., high z_{observed}). Given the current sensitivity of AdLIGO in the science runs O1 and O2, these merging BBHs are not detectable, as the highest observed redshift of a GW event is that of GW170104 at $z_{\text{observed}} \simeq 0.18$. Future improvements in the sensitivity of GW observatories will allow the detection of GWs for BBH mergers at higher redshifts, and confirm or disprove the predicted complex correlation between χ_{eff} , M_{chirp} , merging timescale and metallicity implied by the ‘‘CE’’ isolated binary formation channel.

Five confirmed and one candidate GW event are believed to stem from the merger of two stellar mass BHs. In the ‘‘CE’’ channel, combining our results with the current six events, we draw the following conclusions.

- The masses of the two BHs for GW150914 are around 30 M_{\odot} . Such ‘‘heavy’’ BHs are expected to form in metal-poor environment. We see that models with 0.1 Z_{\odot} may provide a good match with the observed properties, at least as good as the one at $Z = 0.01Z_{\odot}$. Such metallicities are encountered in the present day Universe within the Small Magellanic Cloud. Thus per se, a low metallicity does not strictly require a high redshift. On the other hand, low χ_{eff} values imply a long merging timescale and thus imply that the merging occurred at high redshift. This illustrates how the information on the masses and the spin complement each other for constraining the metallicity and the redshift. From the events GW170104 and GW170814, although less extreme in term of BH masses, similar conclusions can be drawn.
- The event LVT151012 has a lower chirp mass, nearly allowing solar metallicity models with a 30 M_{\odot} BH to be compatible with its observed properties. However, even if it were possible to form a 30 M_{\odot} BH at solar metallicity, present models predict a merging timescale longer than the Hubble time. The measurement of

χ_{eff} consistent with zero allows for long merging timescales and hence, again, the formation of this BBH at high redshift seems to be the most likely scenario.

- The event GW151226 may be explained at all metallicities considered here and in particular by solar metallicity models. Furthermore, taking at face value the statistically significant positive value for χ_{eff} , our models favor merger times shorter than a few Gyr. This implies that the system was formed at a redshift when most of the star formation occurs at solar-like metallicity.
- GW170608 is the lowest-mass BBH merger yet reported. It is found that χ_{eff} has a slight preference to be positive. Therefore, the same arguments hold as for GW151226.

3.7 Discussion

The present results show that the spin parameter of the second-born BH can span all values between 0 and 1. Especially at lower metallicities, the dynamic range of initial orbital periods that lead to a final spin for the second-born BH between 0 and 1 is relatively large. This result is different from those obtained by (Zaldarriaga, Kushnir, & Kollmeier, 2018; Hotokezaka & Piran, 2017) who concluded that the spin parameter of the second-born BH will be either very low, around 0, or very high, around 1 (bimodality). The differences between the present results and those of the aforementioned studies stem from different assumptions concerning mass losses and tides. The bimodality results are based on the approach explained in Kushnir, Zaldarriaga, Kollmeier, & Waldman (2016). Compared to the present approach, the impact of mass loss on a_* is much less pronounced, and the impact of tides is much stronger. This is why, in their model, when tides are important, the He-rich star is tidally locked and the maximum spin is always reached. In our model, even if the orbit is tight at the beginning and tides are important, the star often cannot remain tidally locked indefinitely.

A major uncertainty of the “CE” isolated binary formation channel concerns the way the CE phase is accounted for. In the present work, we did not study this phase directly since we began our investigation after the CE phase. We however implicitly assumed that the star has lost its complete H-rich envelope and that the system is tight. These are features commonly assumed as resulting from a CE phase and in that respect this work follows the present common wisdom. Of course, should these facts be challenged by future studies, it would imply a very strong revision of the global scenario for the evolution of isolated close binary systems.

Mass loss due to the stellar winds of the He-rich star is another source of uncertainty. We used here the most recent estimates for these mass loss rates and we did not explore the impact of changing these values. However, since we studied the evolution of systems at three metallicities, and since changing the metallicity has a deep impact on the mass loss rates, comparing the results at a range of metallicities gives an idea of what would be obtained

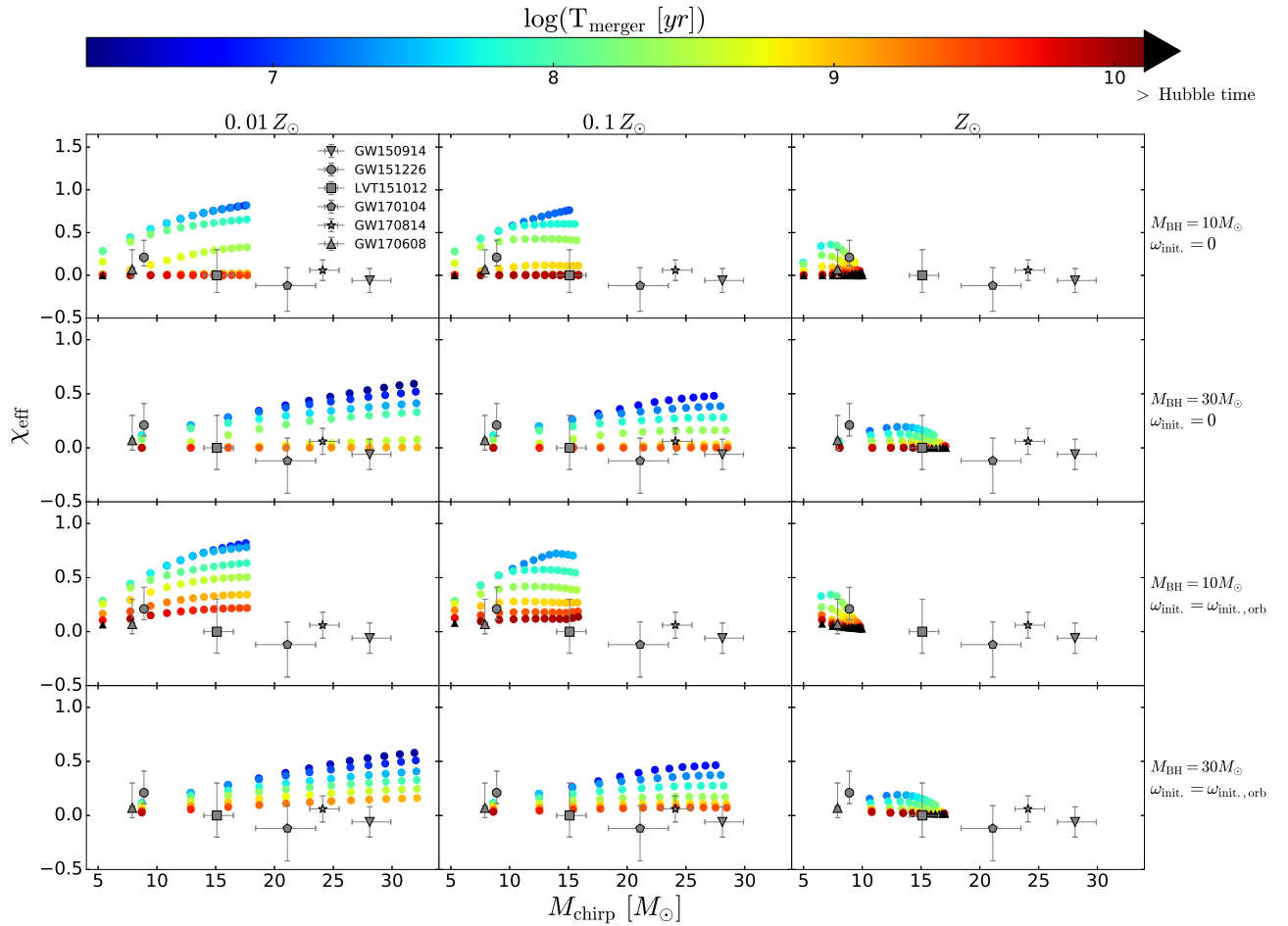


Figure 3.10: T_{merger} as a function of χ_{eff} and M_{chirp} . The first row including three panels corresponds to the binary systems in which the companions are $10 M_{\odot}$ BHs and there is no initial rotation for the He-rich stars. The other three rows are similar to the first row, but with different companions and initial rotation of the He-rich stars. The three columns refer to different metallicities of the He-rich stars, i.e., $0.01 Z_{\odot}$, $0.1 Z_{\odot}$ and Z_{\odot} . The colored dots correspond to the T_{merger} . Three gravitational events and one candidate with specific χ_{eff} and M_{chirp} from the observation of AdLIGO are shown on each panel. Black triangles correspond to binary systems whose T_{merger} is longer than the Hubble time.

by changing the mass loss rates. As discussed above, the effects are large and this underlines the fact that accurate mass loss rates are indeed needed to obtain reliable stellar evolution models.

The physics of the angular momentum transport inside stars is still uncertain. The present results have been obtained assuming a strong coupling between the core and the envelope mediated by a strong magnetic field (Spruit, 1999, 2002; Heger, Woosley, & Spruit, 2005). In cases angular momentum is transported mainly by meridional currents, the coupling is less efficient (e.g., Georgy et al., 2012) allowing the core to retain more angular momentum. All the other physical ingredients kept the same, this produces faster-rotating BHs and NSs.

Under the adopted direct core-collapse model, we assume that the helium stars evolving up to the carbon depletion will soon directly collapse to BHs without any additional mass and angular momentum loss. On the one hand, If the IGRB was produced by the Blandford-Znajek mechanism (Blandford & Znajek, 1977), most of the angular momentum would be lost to launch a jet. This will decrease the spin a_* of the second-born BH and the corresponding χ_{eff} will be lower. For binaries where the helium star at the end of its evolution rotates fast enough to produce a IGRB, these assumptions are inaccurate (systems denoted with star symbols in figures 4-9). On the other hand, if the IGRB was associated with a supernova explosion, the resulting BH mass would be smaller than the mass of the BH from direct core-collapse without mass loss. Based on the expression in Eq. 3.12, M_{chirp} will be smaller. Combining the two factors above, the χ_{eff} and M_{chirp} shown in Fig. 3.10 will be shifted to the lower left. In addition, T_{merger} will also be changed, becoming longer or shorter depending on the degree of anisotropy of the mass ejection.

3.8 Conclusions

Since the first GW event, GW150914, was discovered by AdLIGO, research in the field of BBH-formation channels has been very active. The ‘‘CE’’ channel is one of the main proposed formation channels and likely the most widely studied. The aim of this work is to investigate the final phase in the formation of BBH through this channel, namely the evolution of close binaries consisting of a He-rich star and a compact object. In doing so, we employed detailed binary evolution models that self-consistently take into account the effects of tidal interactions, wind mass loss and the evolution in the structure of the He star, including stellar rotation, and we explored a multidimensional parameter space. Our main findings are summarized in the following.

- Based on detailed stellar structure information, we computed the tidal coefficient E_2 for both H-rich and He-rich stars in a large range of masses and at three different metallicities (Z_{\odot} , $0.1Z_{\odot}$ and $0.01Z_{\odot}$). Based on those calculations, we derived fitting formulae that relate the value of E_2 to the ratio of the convective core radius to the total radius of the star.

- We estimate that the spin of the first-born BH should be low ($a_{*,1} \leq 0.1$), as the progenitor star of the first-born BH evolves to the giant phase before losing its envelope and collapsing to form a BH. During this expansion phase, most of the primordial angular momentum that the star might have had is transferred to its outer layers and subsequently lost due to Roche-lobe overflow mass transfer and wind mass loss. Hence, the first-born BH is expected to have a negligible contribution to the χ_{eff} of the BBH, which in turn sets an upper limit to its possible value at $\chi_{\text{eff}} \leq 0.5$.
- The tidal synchronization timescale becomes comparable to or shorter than the lifetime of the He star at orbital periods below about ~ 2 days, with the exact value depending on the mass of the He star and the binary mass ratio, but independent of metallicity. However, wind mass-losses are strongly dependent on metallicity, and hence the overall orbital evolution of the binary, which is determined by the interplay between tides and wind mass loss, does depend on metallicity.
- Although we find that the initial rotation of the He star does affect our estimates for the resultant BH spin, arguments similar to the ones presented for the first-born BH imply that the expected initial rotation of the He star should be small ($\Omega_{\text{init}} \simeq 0 - \Omega_{\text{init,orb}}$). Limiting the possible initial rotation of the He star in this range results in a weak dependence of our findings on that parameter.
- A systematic exploration of the initial parameter space shows that the spin a_* of the second-born BH covers the whole range (0-1, i.e. from non-rotating to maximally rotating), and that especially at lower metallicities, the dynamical range of initial orbital periods that lead to BH spin with non-extreme values, i.e. between 0 and 1, is quite large.
- Furthermore, we find an anti-correlation between the merging timescale of the BBH, T_{merger} , and the spin of the second born BH, a_* , or the observable quantity χ_{eff} . This is a natural consequence of the fact that in order to form a fast rotating second-born BH, tides should be strong, and therefore the orbital separation between the He-star (progenitor of the second-born BH) and its compact-object companion should be small. The latter also leads to short merging timescales of the resulting BBH. We should note, however, that this anti-correlation is not a one-to-one relation between T_{merger} and χ_{eff} , as it also depends on other factors such as the masses of the two BHs, or the chirp mass M_{chirp} of the BBH, and the metallicity of the BH progenitor star. In that sense, simultaneous and precise estimates of M_{chirp} , χ_{eff} and the redshift at which the merger happened carry information about the time and environment at which the BBH was formed.
- Our models present many possibilities for the formation of BBHs with non-zero, positive χ_{eff} . This at first glance is in contrast to the currently observed sample where 5 out of the 6 detected merging BBHs have χ_{eff}

consistent with 0. However, one should also take into account the current sensitivity of GW observatories that limit us to mergers that happened in the local universe ($z_{\text{observed}} \sim 0$) and show a strong preference to high chirp masses. Combining this with the star-formation and metallicity evolution of the Universe as a function of redshift, we conclude that, most likely, the currently observed sample of merging BBH mainly originates from BBHs that formed at low-metallicity environments and $z_{\text{formation}} \geq 2-3$. Hence, these BBHs must have had long merging timescales and thus low χ_{eff} . As the sensitivity of GW observatories improves and we are able to probe more BBH mergers at high z_{observed} and/or lower chirp masses, our models predict that those BBHs will have preferentially positive, non-zero χ_{eff} .

Chapter 4

On the Origin of Black Hole Spin in High-mass X-Ray Binaries

4.1 Introduction

X-ray binaries are a class of binary stellar systems containing a compact stellar remnant, either a neutron star or a black hole (BH), accreting from a non-compact companion (donor) star. X-ray binaries are often divided into high-mass X-ray binaries (HMXBs) or low-mass X-ray binaries (LMXBs) according to the mass of the donor star. While in LMXBs the donor star overfills its Roche lobe, transferring mass to the compact object through the first Lagrangian point, HMXBs are most often wind-fed systems, where the compact object is capturing and accreting part of the strong stellar wind of its massive donor star companion. Interestingly, all three dynamically confirmed BH HMXBs have massive main-sequence (MS) companion stars (see Table 1), in a few-day orbits, where the companion is close to filling its Roche lobe (Roche-lobe filling factors $> 80\%$, see Orosz et al., 2011; Ziółkowski, 2014).

We should note that some types of BH X-ray binaries, like the BH HMXB candidates IC10 X-1 and NGC300 X-1, are potential progenitors of double BHs (Bulik, Belczynski, & Prestwich, 2011). However, these two systems have Wolf-Rayet companion stars, and the measured velocities are most likely due to the stellar winds of the BH companion instead of its orbital motion (Laycock, Maccarone, & Christodoulou, 2015), which makes the dynamical measurement of the BH mass unreliable.

Over the last decade, the BH spins of 20 X-ray binaries (Miller & Miller, 2015, and references therein) have been measured using two main methods: the continuum fitting method (McClintock, Narayan, & Steiner, 2014, and references therein) and the iron (Fe) $K\alpha$ line fitting method (Reynolds, 2014, and references therein). For LMXBs, the measured spins (namely, $a_* \equiv cJ/GM^2$, where J and M are the AM and mass of the star, c is the speed of light, and G is the gravitational constant) of BHs span the entire range from zero to maximally spinning. Based on the standard isolated binary formation channel, the origin of the BH spin in these binaries can be explained through accretion onto the BH after its birth (Podsiadlowski, Rappaport, & Han, 2003; Fragos & McClintock, 2015; Sørensen et al., 2017).

Table 4.1: Main Properties of High-mass X-Ray Binaries with Measured Spins.

Sources	M_1/M_\odot	M_2/M_\odot	a_*	P/days	References
M33 X-7	15.65 ± 1.45	70.0 ± 6.9	0.84 ± 0.05	3.45	(1),(2),(5)
Cygnus X-1	14.8 ± 1.0	19.16 ± 1.90	>0.983	5.60	(6),(7)
LMC X-1	10.9 ± 1.4	31.79 ± 3.67	$0.92^{+0.05}_{-0.07}$	3.91	(3),(4)

References: (1) Orosz et al. 2007, (2) Liu et al. 2008, (3) Orosz et al. 2009, (4) Gou et al. 2009, (5) Liu et al. 2010, (6) Orosz et al. 2011, (7) Gou et al. 2014.

In contrast, all three of the BH spins measured in HMXBs have been found to be near maximal (see Table 1). Accretion after BH formation was also proposed to explain such a high spin (Brown & Weingartner, 1994; Moreno Méndez, 2011), but the lifetime of the massive companion star was too short (Valsecchi et al., 2010; Wong, Valsecchi, Fragos, & Kalogera, 2012) to significantly spin up the BH assuming Eddington limited accretion. Hence, it would require significantly super-Eddington (mass transfer) MT rates for the BH to accrete any appreciable amount of material. Furthermore, it is unclear how a wind-fed system with a MS accretor can reach such high MT rates, and there is no observational evidence that either of the three observed BH HMXBs are currently undergoing super-Eddington MT. Most recently, it was suggested that slow ejecta from a failed supernova that formed the BH can interact with the companion and be torqued, increasing their specific angular momentum (AM) before falling back onto the newly formed BH (Batta, Ramirez-Ruiz, & Fryer, 2017). However, follow-up simulations showed that realistic velocity profiles of the supernova ejecta can only lead to mild spin-up of the BH (Schröder, Batta, & Ramirez-Ruiz, 2018). Alternatively, it has been suggested that gravity waves during the very last phases of the evolution of massive stars (Fuller, Cantiello, Lecoanet, & Quataert, 2015) or instabilities during the core collapse phase (Moreno Méndez & Cantiello, 2016) can add AM in the collapsing core in a stochastic way. But in both cases the amount of AM that can be transferred cannot lead to a significant BH spin.

Rather than being acquired at its birth or posterior to it, the spin of the BH could be directly related to the AM of the progenitor star. Valsecchi et al. (2010) proposed a formation channel for the BH HMXB M33 X-7, where the initial binary has an orbit of a few days, and the BH progenitor star transfers part of its envelope to the secondary while still in the MS (Case-A MT, see Kippenhahn & Weigert, 1967). Assuming solid-body rotation during the MS phase and tidal locking while the binary is mass-transferring, the core of the BH progenitor contains large amounts of AM at the end of its MS phase. Having lost its envelope during the Case-A MT, the BH progenitor star never expands to become a giant star. Instead, after the end of the MS, it contracts to become a Wolf-Rayet star, and the binary remains in a close orbit of a few days during its whole lifetime. Sana et al. (2012) found that $\sim 70\%$ of observed O-type stars are in close binary systems, and that half of these are close enough to undergo the

Case-A MT, making this evolutionary path a common one. We also note that a series of systematic investigations (Kobulnicky et al., 2014; Kiminki et al., 2015, and references therein) of massive star binary characteristics in Cygnus OB2 associations have been carried out, which have slightly weaker constraints on the binarity due to limited observational samples.

For binaries close to Roche-lobe overflow at birth with sub-solar metallicities, enhanced rotational mixing has been predicted to result in the CHE of both stars (Mandel & de Mink, 2016; Song et al., 2016; Marchant et al., 2016) or just the more massive component (de Mink et al., 2009; Marchant et al., 2017). The latter case is realized in systems with initial mass ratios far from unity and results in the formation of BH HMXBs with high spins and a MS companion, providing an alternative channel to the Case-A MT.

In this Letter, we investigate the origin of the spin of the BH in HMXBs by studying in detail the evolution of close massive binaries, which leads to the Case-A MT and the CHE. The main methods used in the stellar and binary evolution models are discussed in §4.2 and we present our results in §4.3. We describe the resulting BH spins from the Case-A MT and the CHE in §4.3.1, the relevant range in orbital periods, primary masses, and mass ratios leading to both formation channels in §4.3.2, and also discuss how the Case-A MT leads to nitrogen enrichment of the BH companion in §4.3.3. We then compare our results with current observations in §4.4. Finally, the main conclusions of this Letter are summarized in §4.5.

4.2 Methods

We use release 10398 of the **MESA** stellar evolution code (Paxton et al., 2011, 2013, 2015, 2018) to perform all of the binary evolution calculations presented in this Letter. We adopt a metallicity of $Z = Z_{\odot}/2$, where we take the solar metallicity to be $Z_{\odot} = 0.017$ (Grevesse, Noels, & Sauval, 1996). The initial helium mass fraction is computed by assuming that it increases linearly from its primordial value of $Y = 0.2477$ (Peimbert, Luridiana, & Peimbert, 2007) at $Z = 0$ to $Y = 0.28$ at $Z = Z_{\odot}$. We model convection by using the standard mixing-length theory (Böhm-Vitense, 1958) with a mixing-length parameter of $\alpha = 1.5$ and adopt the Ledoux convection criterion. We model semiconvection according to Langer, Fricke, & Sugimoto (1983) with an efficiency parameter of $\alpha_{sc} = 1.0$. Step overshooting is considered with an extension given by $0.1H_P$, where H_P is the pressure scale height at the convective core boundary. We model our binary systems until core carbon depletion in the center of the primary star.

Stellar winds are modeled following Brott et al. (2011). For mass loss from hot hydrogen-rich stars ($X > 0.7$ at their surface) we use the prescription of Vink, de Koter, & Lamers (2001). For stars with a surface hydrogen of $X < 0.4$, we use the mass-loss rate of Hamann, Koesterke, & Wessolowski (1995) divided by a factor of 10 to account for clumping (Yoon, Woosley, & Langer, 2010). We further scale the mass-loss rate of Hamann, Koesterke,

& Wessolowski (1995) by a factor of $(Z/Z_{\odot})^{0.85}$, assuming the same metallicity dependence predicted by Vink, de Koter, & Lamers (2001) for hydrogen-rich stars. We linearly interpolate these two mass-loss rates when the surface hydrogen X is between 0.7 and 0.4.

We model rotational mixing and AM transport as diffusive processes (Heger & Langer, 2000), including the effects of Eddington–Sweet circulations, the Goldreich–Schubert–Fricke instability, as well as secular and dynamical shear mixing. We also include diffusive element mixing from these processes with an efficiency parameter of $f_c = 1/30$ (Chaboyer & Zahn, 1992; Heger & Langer, 2000). For an efficient AM transport mechanism (i.e., Tayler–Spruit dynamo; Spruit, 1999, 2002), most of the internal AM is transported to the outer layers when the star leaves the MS.

Tides, in close binaries, play a critical role in the evolution of the orbit and the internal AM of the two stellar components. Here, we adopt the dynamical tide model derived by Zahn (1975). The synchronization timescale, T_{sync} , between the orbital period and the spin period of each star strongly depends on the tidal coefficient E_2 , which in turn depends on the structure profile of each stellar component. Qin et al. (2018) recently computed E_2 for both H-rich and He-rich stars, in a wide range of initial masses, evolutionary stages, and at three different metallicities (Z_{\odot} , $0.1Z_{\odot}$, and $0.01Z_{\odot}$). For H-rich stars, the derived fitting formula relating the value of E_2 to the ratio of the convective core radius to the total radius of the star is given in Eq. 9 of that paper, and this is what we use throughout this Letter. In the standard implementation of tides in **MESA**, each layer of the star is synchronized independently on the timescale of T_{sync} (i.e., equation (20) from Paxton et al., 2015). Instead, in this Letter we implement a variation of that approach, where the tides operate only on the radiative layers. We have verified that this variation has a very small impact on our results. MT is treated as a conservative process, but as the accreting star is spun up due to accretion, enhanced stellar winds can lead to effectively fully non-conservative MT (see section 2.9 of Paxton et al. 2015 and references therein). Relevant files to reproduce all of the calculations of this Letter can be found on the **MESA** website ¹.

4.3 Results

4.3.1 Spin of BHs formed by the Case-A MT or the CHE

Here we investigate in detail the evolution of two close massive binaries that only have a different initial orbital period. In Fig. 4.1, we show the evolution of various quantities including the spin parameter a_* for the two representative binaries undergoing the Case-A MT and the CHE. The initial masses of the primary and the secondary, for both sequences, are 95.0 and 38.0 M_{\odot} . For an initial orbital period of 3.25 days, the orbit initially expands to a period of about 4 days due to wind mass loss, at which point the primary star has expanded enough to fill its

¹http://cococubed.asu.edu/MESA_market/inlists.html

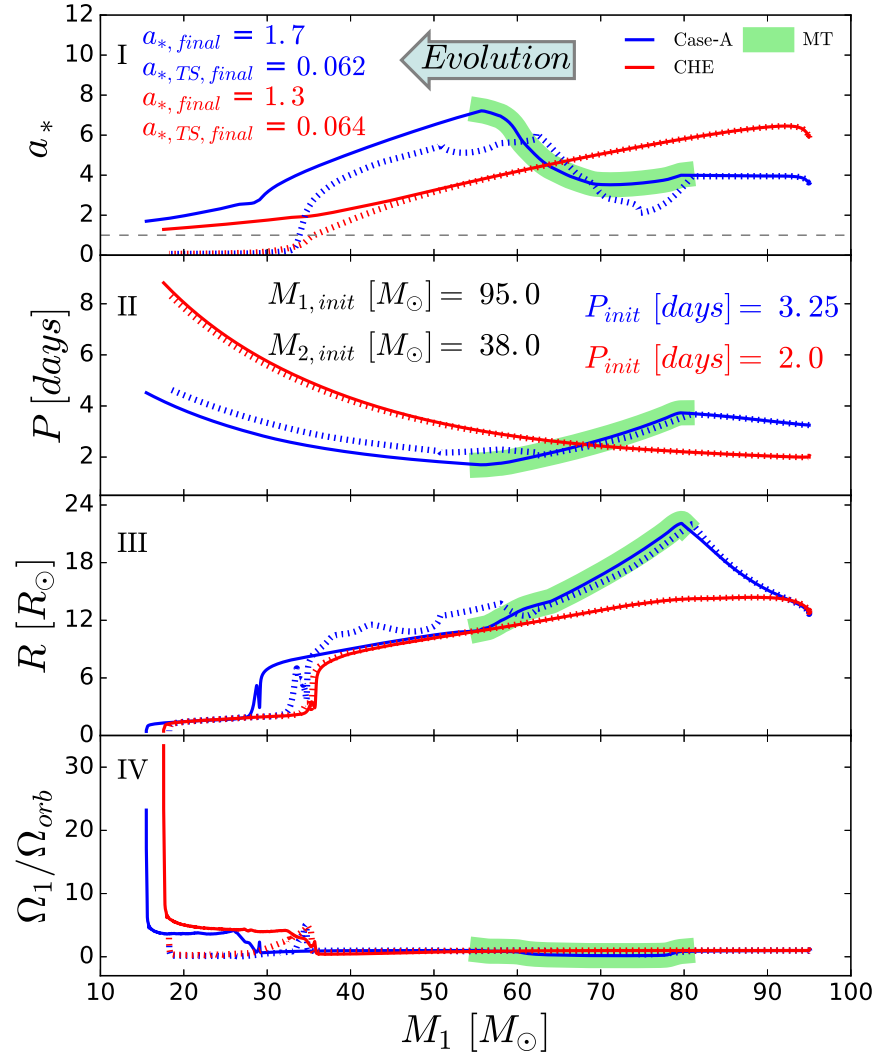


Figure 4.1: Spin parameter a_* (I), orbital period (II), primary’s radius (III), and rotational frequency ratio of primary to the orbit (IV) as a function of primary mass for two binary evolutionary sequences starting with same initial masses of two components but different initial orbital periods. The sequence with the longer initial period ($P_{init} = 3.25$ days; blue line) evolves via the Case-A MT, while the one with the shorter initial period ($P_{init} = 2.0$ days; red line) evolves via the CHE. Green shading represents the MT phase for the Case-A MT channel. The gray dashed line on the top panel indicates the theoretical maximum spin (i.e., $a_* = 1$) of a BH and the arrow represents the direction of the evolution along the time. In both cases, assuming direct collapse, the BH progenitor star has enough AM to form a maximally spinning BH when it reaches core carbon depletion. For comparison, the dotted lines represent the same sequences but with an efficient AM transport mechanism.

Roche lobe and initiate MT (shown in green shading). Since the binary is initially assumed to be synchronized, a_* is already high (~ 3.8) at the beginning of the simulation, and even increases slightly during the initial detached evolution, as the star expands during the MS increasing its moment of inertia. When the MT phase initiates, the primary star contracts due to mass loss in order to fit within its Roche lobe, and at the same time the orbit shrinks on a timescale of ~ 1000 years. These two processes have competing effects on the spin AM of the star. The decrease of the radius lowers the moment of inertia of the star, while the decrease of the orbital period increases the spin frequency of the star, which remains synchronized until the end of the MT phase. Overall, after an initial small decrease, a_* reaches its maximum value at the end of the MT phase.

Shortly after the mass ratio of the binary reverses and the orbit starts expanding due to the MT, the binary detaches. The primary star continues to lose mass due to stellar winds, leading to orbital expansion and a gradual decrease of the spin parameter a_* . When the primary depletes hydrogen in its core, most of the hydrogen envelope has been lost and the entire star contracts until helium is ignited in its core. The timescale of contraction is much shorter than both the timescales of tidal synchronization and mass loss, so the star retains most of its AM, and loses corotation with the orbit; see panel (IV). The primary star, whose radius has now decreased by a factor of ~ 5 , continues its evolution effectively as a single star, losing mass and AM only via stellar winds. Despite the intense mass loss, the primary star retains enough AM when it reaches core carbon depletion to form a maximally spinning BH.

Evolution is significantly different for a binary with the same component masses but a shorter orbital period (i.e., $P_{\text{init}} = 2.0$ days). Enhanced rotational mixing leads to the CHE for the primary star, and its radius never expands to fill its Roche lobe. Instead, during its MS evolution the radius of the primary decreases due to stellar winds, and when core hydrogen is depleted, its radius quickly decreases by a factor of ~ 4 as the star contracts to ignite helium. Since the binary never experiences Roche-lobe overflow, which would shrink the orbit, the final orbital period is larger than that of the Case-A MT sequence shown. The spin parameter a_* of the primary is monotonically decreasing during the whole evolution and its final value is 1.3, retaining enough AM to form a fast-spinning BH.

We should note here that the efficiency of AM transport does not play a crucial role during MS evolution. Fig. 4.1 also shows the evolution of these two representative models including efficient AM transport from the Tayler–Spruit dynamo (see the dotted lines). We find that the evolution in the MS is similar, with both the Case-A MT and the CHE leading to the formation of a helium star with enough AM to produce a maximally spinning BH. The subsequent evolution, however, heavily depends on the AM transport efficiency, as tidal interaction becomes negligible and the star undergoes effectively single stellar evolution. Efficient AM redistribution coupled with strong wind mass loss rapidly depletes the AM of the whole star and our models that include the Tayler–Spruit

dynamo result in BHs with spin parameters of $a_* < 0.1$.

4.3.2 Impact of the initial orbital period and primary mass on the various outcomes

In order to explore the impact of the initial parameters on Case-A and CHE, we computed 4845 binary evolution sequences with varying primary star masses, mass ratios ($q = M_2/M_1$), and initial orbital periods. The primary masses range from 20 to 110 M_\odot in intervals of 5 M_\odot , mass ratios from 0.25 to 0.95 in steps of 0.05, and initial orbital periods between 1 and 4 days in steps of 0.25 days and between 4 and 6 days with a lower resolution of 0.5 days. In Fig. 4.2, we show a slice of our grid with initial mass ratios of 0.4 (other mass ratios show qualitatively similar results). Our fiducial grid assumes inefficient AM transport. However, we repeated our calculations with the Tayler–Spruit dynamo operating in the interior of the star. Including the Tayler–Spruit dynamo does not change the outcomes shown in Fig. 4.2 significantly, but alters the final BH spins dramatically.

For primary masses $M_1 < 60M_\odot$, most of the systems in Fig. 4.2 undergo dynamically unstable MT and are expected to merge. The more massive primaries lose significant mass before the Roche-lobe overflow, reducing the mass ratio and leading to stable Case-A MT and the formation of a HMXB. Most binaries with initial orbital periods of $P < 2$ days evolve into overcontact binaries extending beyond the second outer lagrangian point L_2 overflow (Marchant et al., 2016), and are also expected to merge. When the initial orbital period becomes much shorter (i.e., $P_{\text{init}} < 1.5$ days), the primary star overflows its Roche lobe at the ZAMS, representing a lower limit on the initial orbital period. Finally, CHE occurs only for a very small part of the parameter space, for orbital periods near overflow at ZAMS and high primary masses. This part of the parameter space has been shown to grow significantly for lower metallicities (Marchant et al., 2017). Furthermore, here we point out that a convergence of a_* to changes in spatial and temporal resolution was reached before running all of the simulations, which makes our result more reliable. The orange squares shown in Fig. 4.2 correspond to the simulation that was not completed. Such numerical errors don not arise from some inadequacies in the code, but rather from the need to take very small time steps. Likely the proper handling of such situation would require a change in the numerical techniques.

Fig. 4.3 shows the evolution of masses, orbital periods, and spin parameters a_* , for sequences from a slice of our grid with an initial mass ratio of 0.4. The systems that evolve via the Case-A MT channel (blue squares in Fig. 4.2) are shown on the first column of Fig. 4.3, where, for clarity, we only show half of the sequences. In the second column, all of the systems going through CHE (red squares in Fig. 4.2) are presented. In each column, black triangles refer to the initial conditions and the lines with same color and style correspond to the same binary system. The same grid is also calculated assuming efficient AM transport through the Tayler–Spruit dynamo, and the results are presented in the two columns with the gray background. We find that all of the primary stars in binary sequences with inefficient AM transport collapse to form BHs with high spins. In contrast, for all of the other systems with efficient AM transport mechanism, the BH spins are negligible.

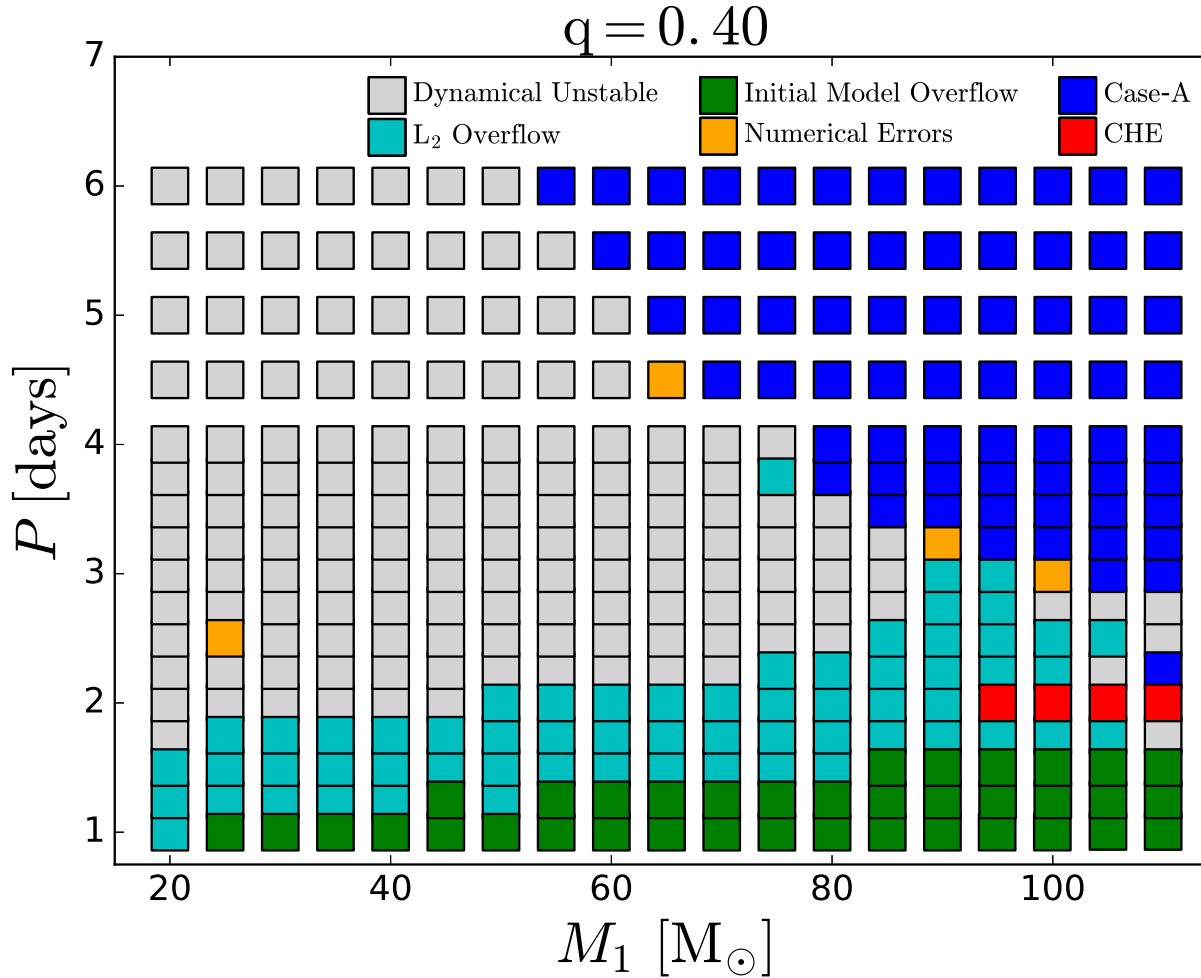


Figure 4.2: Outcomes of binary systems with a fixed mass ratio of $q = 0.4$ and different initial orbital periods and primary star masses. The gray squares represent systems with MT rates higher than $10 M_\odot \text{ yr}^{-1}$, which we consider as dynamically unstable, the cyan squares represent systems that overflow the second Lagrangian point L_2 , and the green squares represent models that are overflowing at the zero-age MS (ZAMS). The blue squares represent systems that undergo the Case-A MT, red squares represent systems that undergo the CHE, and orange squares represent models with numerical errors and where the simulation was not completed.

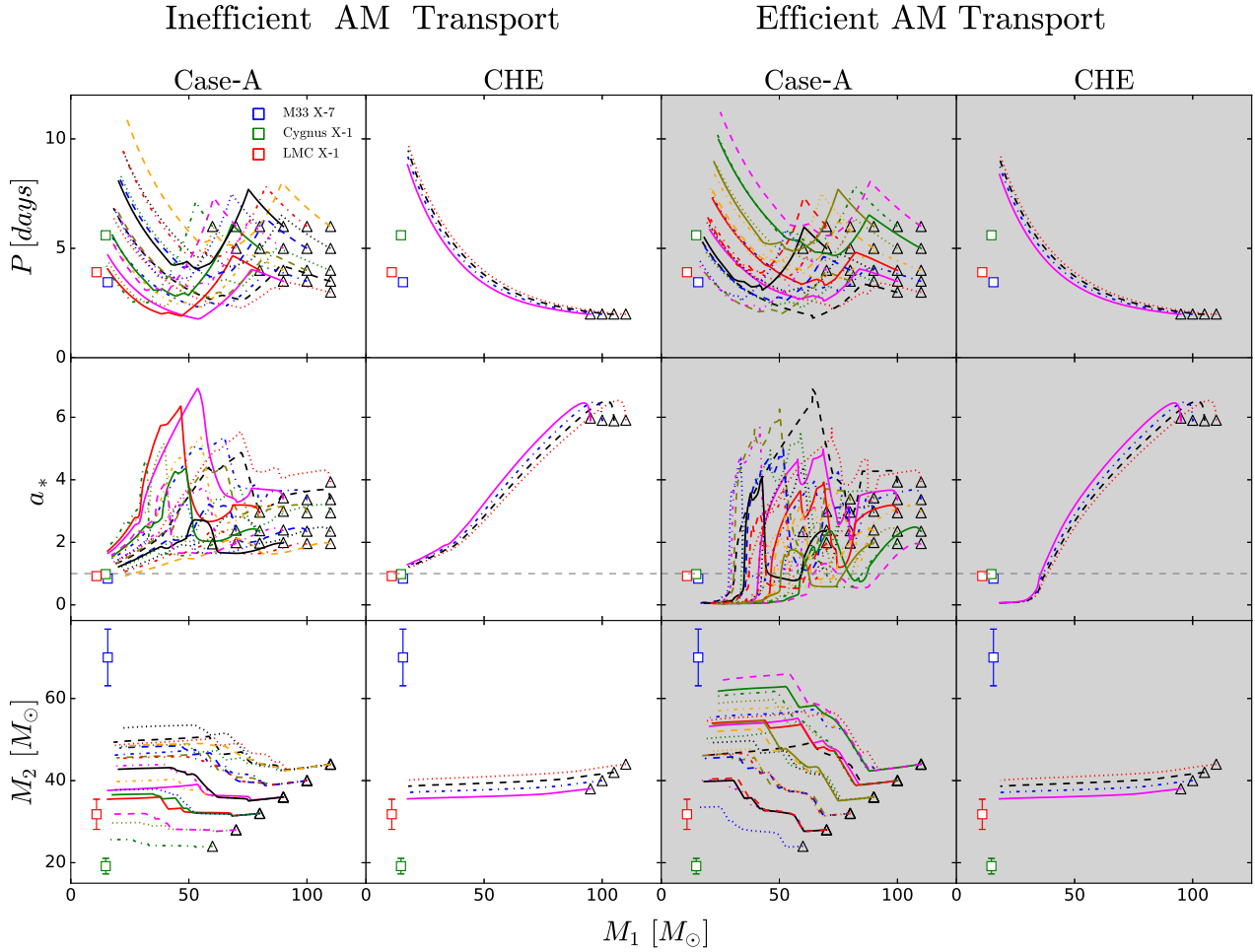


Figure 4.3: Evolution of the orbital period, spin parameter a_* and secondary mass as function of primary mass for inefficient and efficient (namely with Tayler–Spruit dynamo marked by the gray background) AM transport mechanism. The black triangles refer to the initial properties of the binary systems, i.e., masses of two components and orbital period. In each column, one system is marked with the same color and line style. The squares show the properties of HMXBs with measured spins (blue for M33 X-7, green for Cygnus X-1, and red for LMC X-1). In the middle horizontal panels, the horizontal dashed line marks $a_* = 1$.

Finally, in each binary evolution, MT is initially treated as a conservative process. As the BH companion star is spun up, however, it reaches the critical rotation, which stops the accretion onto the secondary star, and the MT become non-conservative. In contrast, when non-conservative MT is initially assumed, a fast-spinning BH can still form, but more mass would be lost during the MT phase, which produces a wider binary system and hence a less massive BH companion. Overall, we expect that non-conservative MT throughout would just shift the properties of the progenitors that successfully match the observed systems.

4.3.3 Enhancements of the nitrogen surface abundance via the Case-A MT channel

We also find that the Case-A MT leaves a distinct observational signature on the companion star, which could potentially allow us to distinguish them from HMXBs formed via the CHE or the classical common envelope evolution channel. In Fig. 4.4, we show the nitrogen surface abundance of the accreting star (which later becomes the donor during the HMXB phase) for the Case-A MT and the CHE sequences discussed in §3.1. For the Case-A MT model, mass is transferred from deep layers of the primary that have been reprocessed from the CNO cycle and are thus nitrogen rich. This greatly enhances the nitrogen on the surface of the accretor (see Langer et al., 2008). When MT stops, the nitrogen abundance drops due to dilution from thermohaline mixing, but its final value is still almost 1 dex above the pre-interaction value. In contrast, in the CHE channel much less important enhancements are reached, with ~ 0.3 dex enhancement shown in Fig. 4.4 arising from a combination of mass loss and mild rotational mixing. In the classical common envelope channel, the two massive hydrogen-rich stars have an initially a wide orbit. When the primary star fills its Roche lobe in its giant phase, MT is dynamically unstable and the system undergoes a common envelope phase, during which the secondary is not expected to accrete any significant amount of mass. Thus, overall, no enhancements in the nitrogen surface abundance is expected. We then expect large (~ 1 dex) enhancements of nitrogen abundance to be a characteristic property of the donor stars in BH HMXBs formed through the Case-A MT.

4.4 Comparison with observations

Overall, Fig. 4.3 shows that the CHE leads to final orbits that are too wide compared to the orbital periods of observed BH HMXBs. Furthermore, the parameter space at which the CHE occurs is very small compared to the parameter space corresponding to the Case-A MT, at least for the metallicities relevant to systems we consider here. For every BH HMXB originating from the CHE channel, one would expect to see many more coming from the Case-A MT. Both of these arguments point to the conclusion that the most likely formation channel for the three observed BH HMXBs with measured BH spins is the Case-A MT channel.

In order to be more quantitative, we searched all of the sequences of our grid to find the ones that most closely resemble the observed properties of Cygnus X-1, LMC X-1, and M33 X-7 (see Table 1). The three best-fit se-

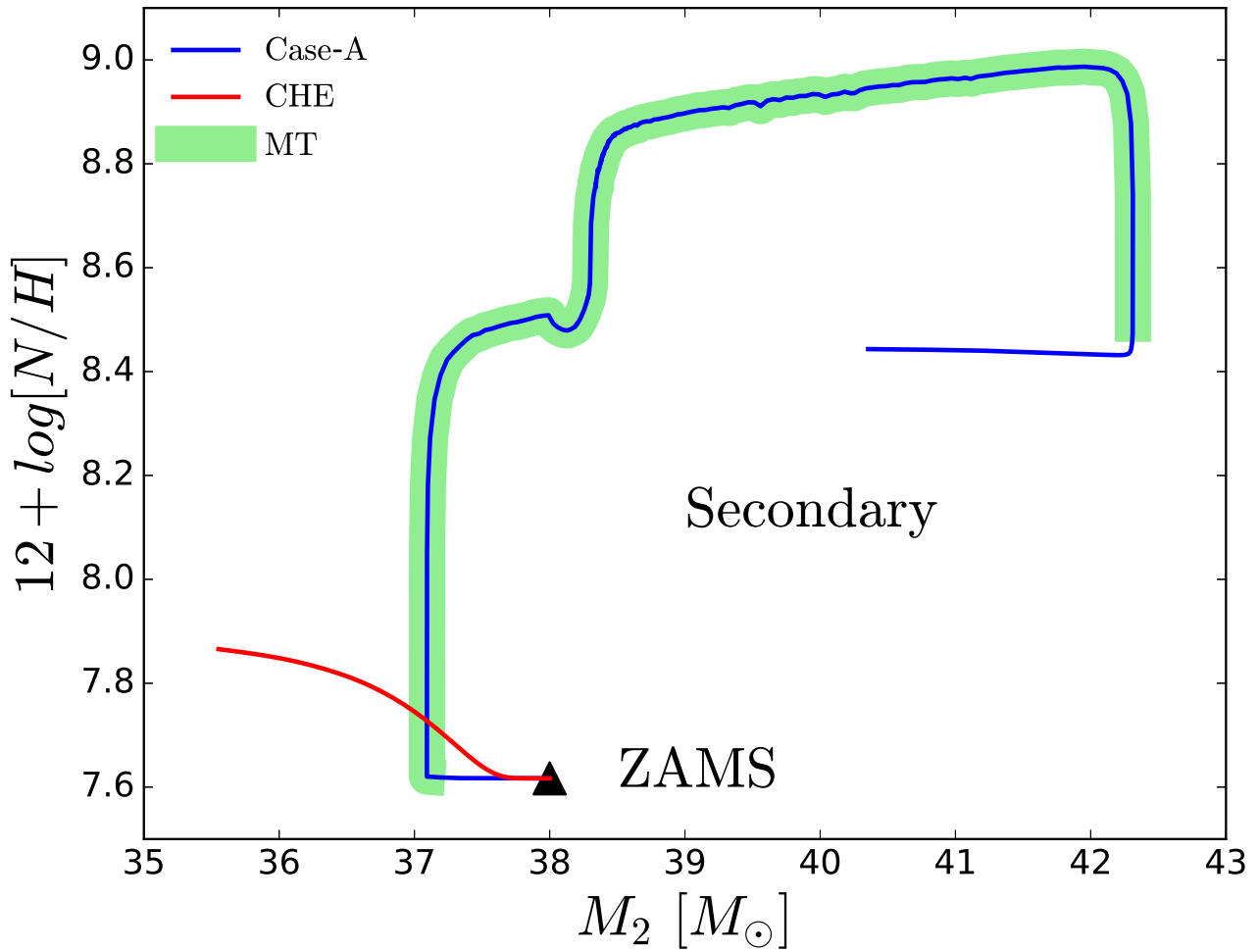


Figure 4.4: Nitrogen surface abundance of secondary as a function of its mass for the Case-A MT (blue solid line) and the CHE (red solid line), respectively. The green shading corresponds to the MT phase, which is same as that shown in Fig. 4.1. The black triangle represents the ZAMS.

quences were selected by applying the minimum χ^2 method to the observed properties (i.e., masses of the BH and its companion as well as the orbital period). For all three HMXBs, 0.5 days (the results are not sensitive to the choice.) is taken as the observational error of the orbital period to obtain the best match. Otherwise, the real observational error of orbital period is so small that its weight dominates the value of χ^2 . Furthermore, we assumed that the BH was formed through a direct collapse, so the mass of the primary at central carbon exhaustion is equal to the mass of the resultant BH, and hence the orbital period remains unchanged after the BH formation.

In Fig. 4.5, we show the three best-fit sequences and one can see that they match the BH masses and periods well. For LMC X-1, the selected sequences are consistent also with the companion mass. For Cygnus X-1, we can see the mass of the companion star is about 1σ higher than the measured mass. A higher resolution of the grid might be required to better match it. Besides, surface abundance anomalies consistent with CNO processed material have already been observed in Cygnus X-1 (Caballero-Nieves et al., 2009), providing additional support to the Case-A MT channel involving stable MT for this particular object. For the best-fit selected sequence of M33 X-7, the mass of the companion star is far below the measured value. This is because for the high initial primary mass and high initial mass ratio that are required in order to produce a system like M33 X-7, the companion star is being spun up due to accreted material, making the MT highly non-conservative. We should stress that although our prescription for the accretion efficiency is physically motivated, it remains approximate and highly uncertain. Had the MT been assumed to be conservative, as in Valsecchi et al. (2010), the mass of the BH companion could reach much higher values.

4.5 Conclusions

In this Letter, we explore different AM transport mechanisms to investigate the AM of the BH progenitor via the Case-A and the CHE channels. We find that the efficiency of the AM transport does not play a crucial role during the MS phase. However, in order to form a fast-rotating BH in HMXB, weak coupling between the core and envelope inside the star after its MS phase is required both for systems evolving along the Case-A and the CHE channel.

The Case-A MT can explain the current properties of Cygnus X-1, LMC X-1, and M33 X-7 well. For the metallicity we have studied ($Z_{\odot}/2$), the CHE forms wider binary systems, which is not consistent with currently observed HMXBs with measured BH spins. The mismatch of the companion mass for M33 X-7 might be due to uncertainties in the prescription used here for the accretion efficiency, which requires further study. Furthermore, the Case-B channel, where MT is initiated after the primary depletes its central hydrogen, would result to an even wider HMXB orbit due to the longer initial period and earlier wind mass loss from the system, which makes such systems relatively dim². In contrast, the Case-A MT channel produces tight BH X-ray binaries with more massive

²Based on the Bondi accretion mechanism (Bondi & Hoyle, 1944), the mean accretion rate was given in Equation (6 of Hurley, Tout, &

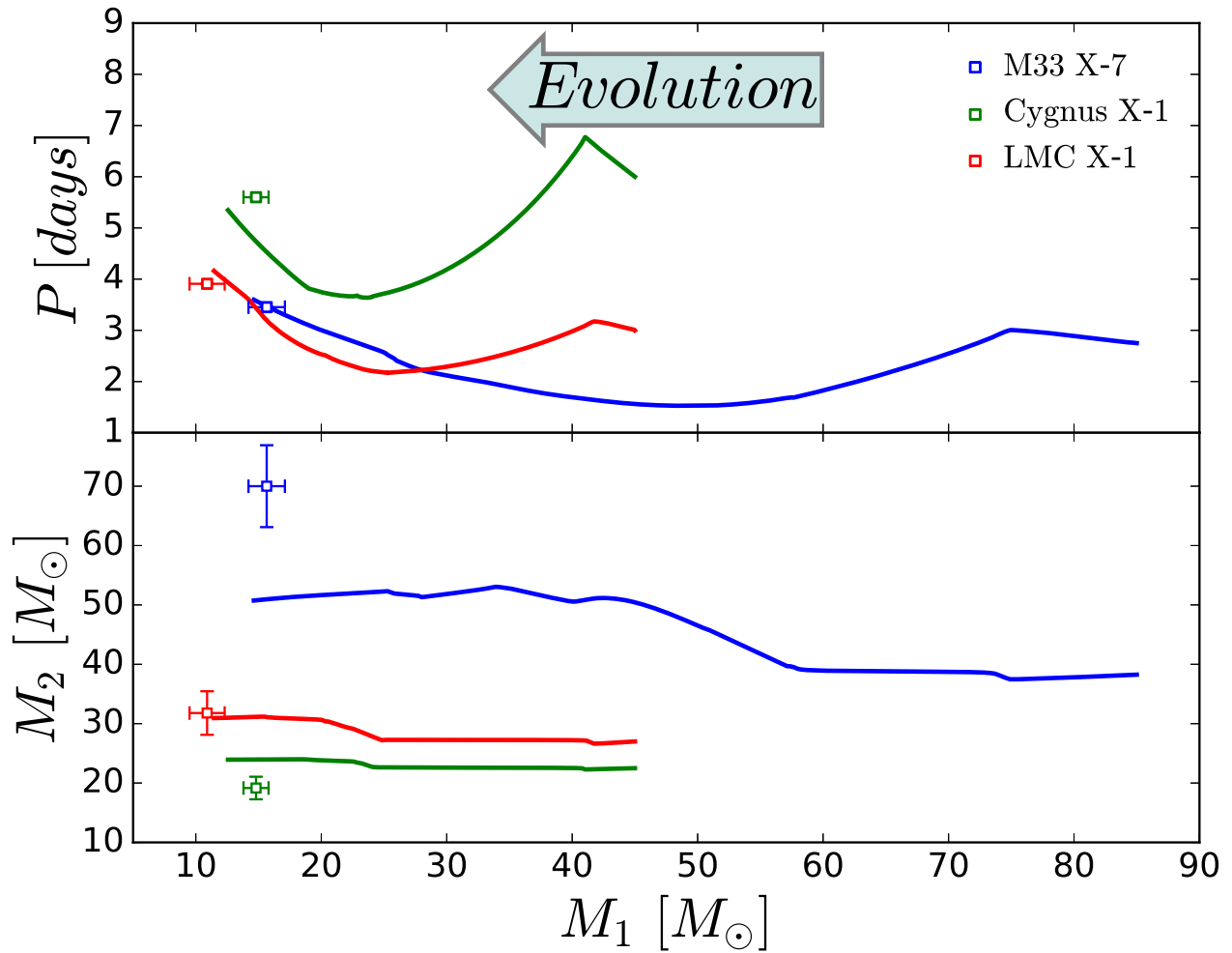


Figure 4.5: Orbital period (top panel) and secondary mass (bottom panel) as a function of primary mass. Blue, green and red solid lines correspond to the "best-fit" binary sequences that reproduce HMXBs that resemble M33 X-7, Cygnus X-1 and LMC X-1, respectively. The properties of the observed systems are marked with blue, red and green squares for M33 X-7, Cygnus X-1 and LMC X-1, respectively. The arrow on the top panel represents the direction of the evolution.

donor stars, which makes such systems significantly bright and most likely to dominate the observed sample of BH wind-fed HMXBs. Quantitative predictions of the relative occurrence of each channel require population synthesis calculation, which will be the topic of a follow-up study.

Significant enhancements of the nitrogen surface abundance of donor stars in HMXBs can be produced in the Case-A MT channel. Thus it can be considered an important auxiliary tool to distinguish the Case-A MT channel from classical common envelope or the CHE channel.

Pols, 2002). For a very wide orbit (i.e., orbital velocity is far smaller when compared to the velocity of the donor's wind), an estimation can be obtained, namely $L_X \propto P_{\text{orb}}^{-4/3}$, where L_X is the luminosity in X-ray phase and P_{orb} is the orbital period. For Case-B or any other possible channels, the P_{orb} in the X-ray phase should be much larger, which results in a much more dimmer L_X .

Chapter 5

On the Conditions of Chemically Homogeneous Evolution

5.1 Introduction

Since the discovery of the first gravitational wave event GW150914 by the AdLIGO, the chemically homogeneous evolution (CHE) has been proposed to be one of the most important formation channels for double BHs. Chemical mixing due to fast rotation can keep massive stars evolving chemically homogeneously (Maeder, 1987). The CHE in binary stars was first investigated in de Mink et al. (2009) and has been recently studied in more details (Yoon, Dierks, & Langer, 2012; de Mink & Mandel, 2016; Mandel & de Mink, 2016; Marchant et al., 2016; Song et al., 2016).

The conditions for triggering the CHE is still unclear. In order to undergo the CHE, stars need to be massive, at a low metallicity, and a fast initial rotation rate. However, a study on how the initial conditions for obtaining a homogeneous evolution depend on the physics of the transport of the angular momentum and of the chemical species has still to be made.

It has been noted that internal magnetic fields play a pivotal role in the stellar evolution. The internal magnetic field can be amplified by differential rotation in the radiative layers and such a dynamo process (*TS* dynamo) was proposed by Spruit (1999, 2002). However, a theoretical debate (Zahn, Brun, & Mathis, 2007) is still ongoing. The observed flat rotation profile of the Sun (Eggenberger, Maeder, & Meynet, 2005), as well as observations of the final rotation of white dwarfs and neutron stars (Heger, Woosley, & Spruit, 2005; Suijs et al., 2008) can be reproduced with *TS* dynamo. But the *TS* dynamo cannot reproduce the asteroseismic constraints for sub-giants and red giants (Gehan et al., 2018; Eggenberger et al., 2019). Such mechanism has been implemented in both **MESA** and **GENEVA**. However, the implementation in both codes is different. Hence here we also investigate the impact of the *TS* dynamo on the conditions for triggering the CHE with both codes.

In this work, we first present in §5.2 a comparison of the CHE for non-rotating models between **MESA** and **GENEVA**. The comparison of the CHE for rotating models are shown in §5.3. Finally, we show our main results and discussions in §5.4.

5.2 Comparison of non-rotating models

In order to have a fair comparison of rotating models between the two codes, we start with non-rotating models in which we do our best to involve the same fundamental model assumptions. In both stellar evolution codes, we model the convection following the standard mixing-length theory (Böhm-Vitense, 1958) with a mixing-length coefficient $\alpha = 1.5$. We adopt Schwarzschild criterion to treat the boundary of the convective cores, and a step overshooting above the Schwarzschild boundary of the convective core with $\alpha_p = 0.1 H_p$, where H_p is the pressure scale height. We use release 10398 of the **MESA** stellar evolution code to perform all the calculations here, while for **GENEVA** code, we refer readers to Eggenberger et al. (2008).

For the comparison of all models (also for rotating models), we consider a low metallicity ($0.01 Z_\odot$, where $Z_\odot = 0.017$). As shown in Fig. 5.1, three models with different initial masses (20, 45 and 60 M_\odot) are computed from zero-age main sequence (ZAMS) to terminal age main sequence (TAMS). We see that the results are consistent.

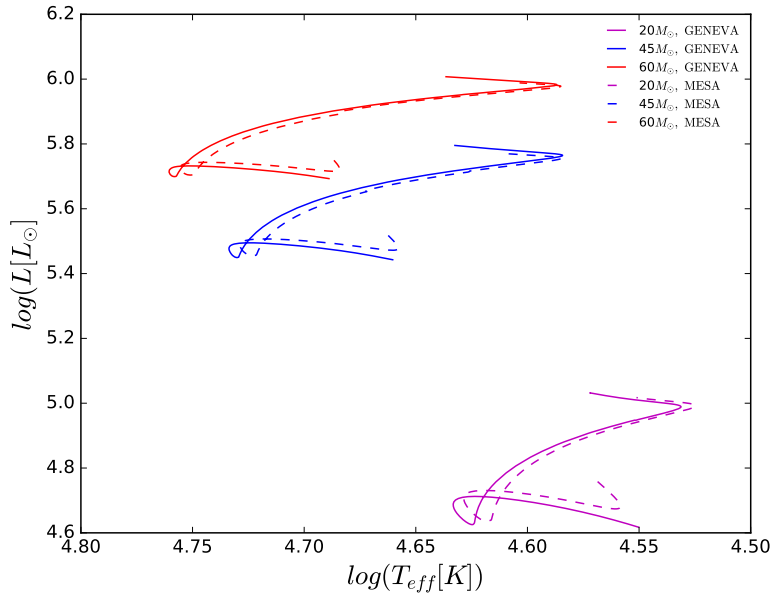


Figure 5.1: Comparison of Hertzsprung-Russell (HR) diagram for non-rotating models between **GENEVA** (solid lines) and **MESA** code (dashed lines). Red: 20 M_\odot , blue: 45 M_\odot , magenta: 60 M_\odot .

5.3 Comparison of the CHE for rotating models

When a star rotates, it will be deformed and cannot simultaneously be in thermal and hydrostatic equilibrium. The rotation produces internal currents, such as meridional (Eddington-Sweet) circulation, which exchanges material between the core and the outer region and hence produces observable enhancements of nitrogen for massive stars. Such circulation is much more efficient when compared to other instabilities for the transport of the angular mo-

mentum. For what concerns the transport of the chemical species, depending on the physics of rotation considered, meridional current can also dominate, or be superseded by shear instabilities. It was pointed out that the Eddington-Sweet circulation depends on the μ gradient (Tassoul & Tassoul, 1984; Lau, Izzard, & Schneider, 2014). In order to evaluate the impact of the sensitivity on spatial and temporal resolution, we carried out for **MESA** models a convergence test of Eddington-Sweet circulation. Our results are presented in Appendix 5.5. The convergence test shows that the dependence of the resolution is not strong and the result are robust.

5.3.1 MESA models

In **MESA** model, we treat rotational mixing and angular momentum transport as diffusive processes (Heger & Langer, 2000), which contain the effects of Eddington-Sweet circulations, the Goldreich-Schubert-Fricke instability, as well as secular and dynamical shear mixing. We also include diffusive element mixing from these processes with an efficiency parameter $f_c = 1/30$ (Chaboyer & Zahn, 1992). Eddington-Sweet circulation is dominant when compared to other rotationally induced mixing processes. Various diffusion coefficients are shown in Fig. 1.1.

A comparison of the HR diagram with different physics and initial conditions is shown in Fig. 5.2. First, it is shown in the top-left panel that the minimum value for stars undergoing the CHE is $0.4 \Omega_{init}/\Omega_{crit}^1$ and this threshold gradually decreases with increasing M_{ZAMS} . Second, it is clear that the condition for triggering stars evolving chemically homogeneously does not depend on how efficient the angular momentum transport is implemented inside the star, i.e., including *TS* dynamo or not. In both cases, the internal rotation will not be far from solid rotation, therefore the two types of models do not differ much during the MS phase. After the MS phase however, depending on whether the models account or not of the *TS* theory makes differences. This is because the two types of models react differently to the build up of the internal chemical composition gradient.

In Fig. 5.3, we show a grid of **MESA** models at a fixed metallicity ($Z = 0.01Z_{\odot}$). It is shown that initial rotation of at least $0.5 \Omega_{init}/\Omega_{crit}$ is required for a $10 M_{\odot}$ stars at ZAMS to evolve chemically homogeneously. This threshold gradually decreases when the initial mass increases from 10 to $30 M_{\odot}$. This is because rotationally instabilities are stronger for more massive stars. A big grid with high resolution needs to be explored to see how sensitive is the threshold for the CHE to different initial conditions, i.e., initial mass, initial rotation rate and initial metallicity. In addition, at lower metallicity the star will lose less angular momentum due to the winds. Therefore stars could keep rotating fast and tend to evolve chemically homogeneously more easily. This investigation of the metallicity dependence is still in preparation.

¹ $\Omega_{crit}^2 = (1 - L/L_{Edd})GM/R^3$, L_{Edd} is the Eddington luminosity.

5.3.2 GENEVA models

The transport of angular momentum and chemical mixing in **GENEVA** is extensively described in (Eggenberger et al., 2008). Here a short introduction is given.

Transport of angular momentum

In **GENEVA** models, the transport of angular momentum is modelled as an advection–diffusion process (Zahn, 1992; Maeder & Zahn, 1998):

$$\rho \frac{d}{dt}(r^2 \Omega)_{M_r} = \frac{1}{5r^2} \frac{\partial}{\partial r}(\rho r^4 \Omega U(r)) + \frac{1}{r^2} \frac{\partial}{\partial r}(\rho D r^4 \frac{\partial \Omega}{\partial r}), \quad (5.1)$$

where r is the radius, ρ the density and $\Omega(r)$ the mean angular velocity at radius r . The two terms on the right-hand side of the equation above are the advection flux and diffusion flux of the angular momentum, respectively. The meridional circulation is treated as a truly advective process (Eggenberger et al., 2008). $U(r)$ is the vertical component of the meridional circulation velocity at a distance r to the centre and colatitude θ :

$$u(r, \theta) = U(r) P_2(\cos \theta), \quad (5.2)$$

where $U(r)$ has the following expression

$$U(r) = \frac{P}{\rho g C_p T [\nabla_{ad} - \nabla + (\varphi/\delta) \nabla_{\mu}]} \left\{ \frac{L}{M} (E_{\Omega} + E_{\mu}) \right\}, \quad (5.3)$$

where P is the pressure, C_p the specific heat. Both φ and δ are given in the equation of state $\frac{d\rho}{\rho} = \alpha \frac{dP}{P} + \varphi \frac{d\mu}{\mu} - \delta \frac{dT}{T}$, E_{Ω} and E_{μ} are terms depending on the distribution of Ω and μ (more details in Maeder & Zahn, 1998). The term D in Eq. 5.1 is the total diffusion coefficients in the vertical direction which contain various instabilities, i.e., convection, semiconvection, and shear turbulence. In convection regions, a large diffusion coefficient implies a rotation that is not far from solid rotation (Eggenberger et al., 2008). While in radiative regions, shear mixing and meridional circulation are considered as extra-convective mixing, and hence $D = D_{shear}$, is given as:

$$D_{shear} = \frac{4(K + D_h)}{[\frac{\varphi}{\delta} \nabla_{\mu} (1 + \frac{K}{D_h}) + (\nabla_{ad} - \nabla_{rad})]} \times \frac{H_p}{g\delta} \left[\frac{\alpha}{4} \left(f \Omega \frac{d \ln \Omega}{d \ln r} \right)^2 - (\nabla' - \nabla) \right], \quad (5.4)$$

where f is a numerical factor (0.8836 is taken), K is the thermal diffusivity and $(\nabla' - \nabla)$ refers to the difference between the internal nonadiabatic gradient and the local gradient (Maeder & Meynet, 2001). D_h is the diffusion coefficient to the viscosity due to horizontal turbulence (Chaboyer & Zahn, 1992). The expression of $U(r)$ involves derivatives up to the third order and hence the solution of Eq. 5.1 that takes into account $U(r)$ and D is of the fourth order.

The magnetic instability is very efficient in transporting angular momentum and leads to a near solid body rotation during the MS phase as in the **MESA** model.

Transport of chemical mixing

It was pointed out by (Chaboyer & Zahn, 1992) that horizontal turbulence can compete with the advective term of meridional circulation for the transport of the chemical species. The resulting transport of chemical species is determined by both meridional circulation and horizontal turbulence, which is treated as a diffusive process with the coefficient D_{eff} :

$$D_{eff} = \frac{1}{30} \frac{|rU(r)|^2}{D_h}. \quad (5.5)$$

The transport of chemical species is determined by the equation (Chaboyer & Zahn, 1992):

$$\rho \frac{dX_i}{dt} = \frac{1}{r^2} \frac{\partial}{\partial r} \left[\rho r^2 (D + D_{eff}) \frac{\partial X_i}{\partial r} \right] + \left(\frac{dX_i}{dt} \right)_{nuc}, \quad (5.6)$$

where D is the same as in Eq. 5.1 and the second term on the right-hands of the equation above is the change in abundances produced by nuclear reactions.

Fig. 5.4 shows the results ² of HR diagram with different physics and initial conditions. First, in the three top panels, the required initial velocity of the threshold of the CHE is $0.6 \Omega_{init}/\Omega_{crit}$ ³ when TS dynamo is included. This is close to the value in **MESA** model and the slight discrepancy is likely due to the definition of the critical velocity (see footnote 3 at the bottom). However, in the bottom panels where the TS dynamo is not included, the results are strikingly different. Due to numerical difficulties some of the models for high rotation did not reach TAMS, we can not exclude CHE at $\Omega_{init}/\Omega_{crit} \geq \sim 0.8 - 0.9$.

5.4 Main results and discussions

The CHE has been considered one of the main formation channels for double BHs, however, the conditions for massive stars evolving chemically homogeneously are still poorly understood. In this work, we study the CHE by investigating different physics processes (with and without TS dynamo) and various initial conditions (initial masses and initial rotation rates).

In models without the TS dynamo, both meridional circulation and shear instability are responsible for the AM transport⁴. The chemical elements in models with no TS dynamo are mainly transported by shear turbulence in the

²In the top middle and right panels, models of 45 and 60 M_{ZAMS} at 0.9 $\Omega_{init}/\Omega_{crit}$ are not finished due to very expensive computations. But this does not affect the result because these two stars were evolving chemically homogeneously. Other models in the bottom panels are not finished due to the difficulty of the computations and the central hydrogen abundance at the termination is shown: 20 M_{ZAMS} at 0.9 $\Omega_{init}/\Omega_{crit}$ ($X_c = 0.30$); 45 M_{ZAMS} at 0.6 $\Omega_{init}/\Omega_{crit}$ ($X_c = 0.12$), 0.7 $\Omega_{init}/\Omega_{crit}$ ($X_c = 0.27$), 0.8 $\Omega_{init}/\Omega_{crit}$ ($X_c = 0.40$) and 0.9 $\Omega_{init}/\Omega_{crit}$ ($X_c = 0.53$); 60 M_{ZAMS} at 0.5 $\Omega_{init}/\Omega_{crit}$ ($X_c = 0.12$), 0.6 $\Omega_{init}/\Omega_{crit}$ ($X_c = 0.26$), 0.7 $\Omega_{init}/\Omega_{crit}$ ($X_c = 0.37$), 0.8 $\Omega_{init}/\Omega_{crit}$ ($X_c = 0.48$), and 0.9 $\Omega_{init}/\Omega_{crit}$ ($X_c = 0.56$)

³In **GENEVA** code, $\Omega_{crit}^2 = GM/R^3$ (Maeder & Meynet, 2000a), however in **MESA**, $\Omega_{crit}^2 = (1 - L/L_{Edd})GM/R^3$, L_{EDD} , L_{EDD} is the Eddington luminosity.

⁴(Actually the meridional current dominates the transport of the angular momentum as in **MESA**)

GENEVA models at least in most of the radiative envelopes. Only in a small region near the convective core where the mean molecular weight gradients are strong, the effective diffusion (D_{eff} above) dominates the transport. This is significantly different with the case of **MESA** models, in which chemical elements are mainly transported by meridional currents but not by shear.

We found that in both **MESA** and **GENEVA** codes the initial conditions for the CHE are similar when there is a strong core-envelope coupling (here the TS dynamo is included). The precise conditions of the CHE depend on the implementation of the meridional circulation. In contrast, when there is an inefficient (without TS dynamo) angular momentum transport, the condition for triggering CHE between the two codes are different. We see that, everything else being kept equal, a higher initial rotation is required when the physics included in the non TS **GENEVA** model is accounted for.

From these numerical experiments we can conclude that when we mention models with rotation it is important to specify the physics that has been used to obtain the rotating models. We see here that depending on the physics significantly different values are obtained for instance for the minimum initial rotation to obtain a homogeneous evolution. This is however important to know this initial value because it will to some extent determine whether homogeneous evolution can be more or less frequent in nature.

We have also to say here that models with the TS theory have some advantages with respect to those that do not account for this theory. As was already indicated above, TS models are more in agreement with the observed rotation rates of white dwarfs and young pulsars.

On the other hand, models with no TS dynamo computed by the **GENEVA** code can reproduce the contrast between the rotation of the core to that of the envelope in Beta Cephei stars that have been analyzed through asteroseismological technics (Ekström et al., 2012; Aerts, 2015).

5.5 Appendix: Convergence test of Eddington-Sweet Circulation

As the Eddington-Sweet circulation was introduced in §1.1.1, we here briefly describe how μ gradient is calculated in **MESA**. The original μ gradient is defined as

$$\nabla_{\mu} = \frac{d \ln \mu}{d \ln P}. \quad (5.7)$$

As described in Paxton et al. (2013), a formally equivalent prescription for composition gradient that is both numerically robust and easier to implement is given by

$$B = -\frac{1}{\chi_T} \frac{\ln P(\rho_k, T_k, \mathbf{X}_{k+1}) - \ln P(\rho_k, T_k, \mathbf{X}_k)}{\ln P_{k+1} - \ln P_k}, \quad (5.8)$$

where $\chi_T \equiv d \ln P / d \ln T|_{\rho}$, \mathbf{X}_k represents composition at cell K . However, the composition gradient has been found to be sensitive to the spatial resolution of stellar structure information (Lau, Izzard, & Schneider, 2014), which

produce numerical noise on the diffusion coefficient $D_{ES}(k)$ around the boundary of the convective core. In order to decrease such influence, we implement a method to smooth the diffusion coefficient $D_{ES}(k)$ for each cell k within the range of $0.1H_p(k)$ (i.e., $|r(k) - r(i)| \leq 0.1H_p(k)$), namely,

$$D_{ES}(k) = \begin{cases} \frac{1}{N_1} \sum_{i=k}^{n_z} D(i), & k = 1, \\ \frac{1}{N_1} \sum_{i=k}^{n_z} D(i) + \frac{1}{N_2} \sum_{i=k-1}^1 D(i), & k \neq 1, \end{cases}$$

where $D(i) = D_{ES}(i)f(i)$, $N_1 = \sum_{i=k}^{n_z} f(i)$, $N_2 = \sum_{i=k-1}^1 f(i)$, and $f(i)$ is the smoothing factor that is defined as,

$$f(i) = \exp \left[- \left(\frac{r(i) - r(k)}{0.1H_p(k)} \right)^2 \right] \times dm(i),$$

where $dm(i)$ corresponds to the mass of cell i .

We carry out the convergence test of HR diagram by using different spatial and temporal resolutions in Fig. 5.5. As mentioned earlier, Eddington-Sweet circulation is stronger than other rotational mixing instabilities, so other instabilities are switched off for simplicity. In addition, since rotationally induced mixing processes work both by transporting angular momentum and mixing chemical elements, we limit the test to the Eddington-Sweet circulation by forcing solid-body rotation and all the models are terminated at TAMS.

It is believed that the Eddington-Sweet circulation is induced by rotation, so we study the convergence test by using different initial rotation rates in the unit of critical rotation (i.e., $\Omega_{init}/\Omega_{crit} = 0.0, 0.1, 0.2, 0.25, 0.30, 0.35, 0.4, 0.7$ and 0.9). In the testing models, the initial mass at ZAMS is $60 M_\odot$ and 0.01 solar metallicity is taken. Our convergence tests are shown in Fig. 5.6. It is clearly shown that stars starting with an initial velocity below $0.3 \Omega_{crit}$ evolve to supergiant phase after the MS, while at an initial rotation rate larger than 0.35 the stars go to blue branch and evolve chemically homogeneously instead. However, we point out that the dependence of resolution (spatial resolution) appears at an initial rotation rate of 0.3 , where CHE is being triggered. The μ gradient could be built up in some layers due to a higher spatial resolution that will boost the diffusion coefficient $D_{ES}(k)$ of Eddington-Sweet circulation. As a result, a larger diffusion coefficient $D_{ES}(k)$ can produce a strong mixing inside the star and bring the hydrogen from the outer layers back into the core. Finally in this test, we found that variations of spatial and temporal resolutions converge to the identical results.

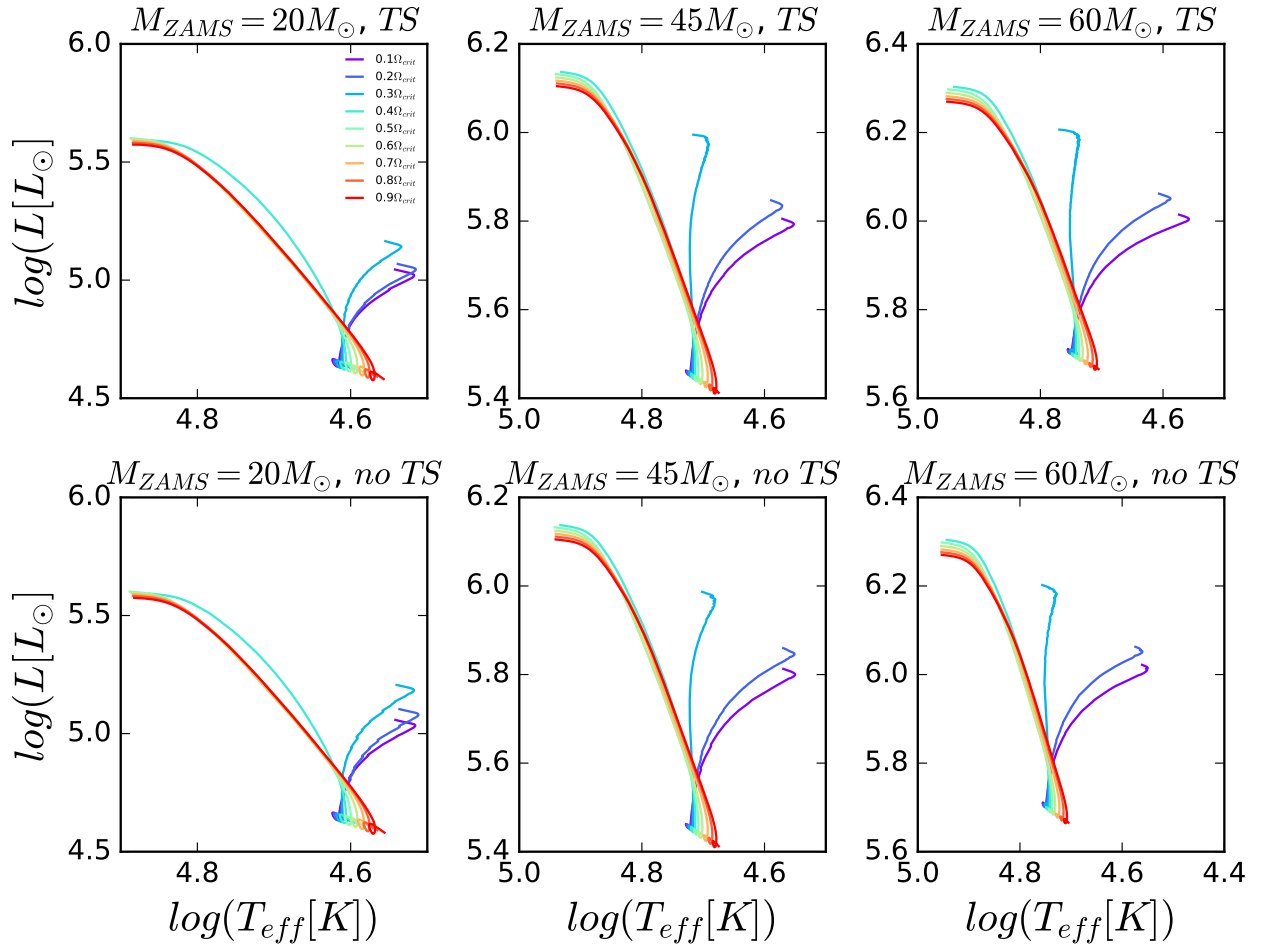


Figure 5.2: HR diagrams of **MESA** models with different initial mass at ZAMS. Top panels are models calculated with *TS* dynamo, while bottom ones are models without *TS* dynamo. The initial masses at ZAMS are marked in the title of each panel. The coloured lines (As shown in the top left panel, the initial velocity increases from purple to red) represent different initial velocities in unit of critical velocity.

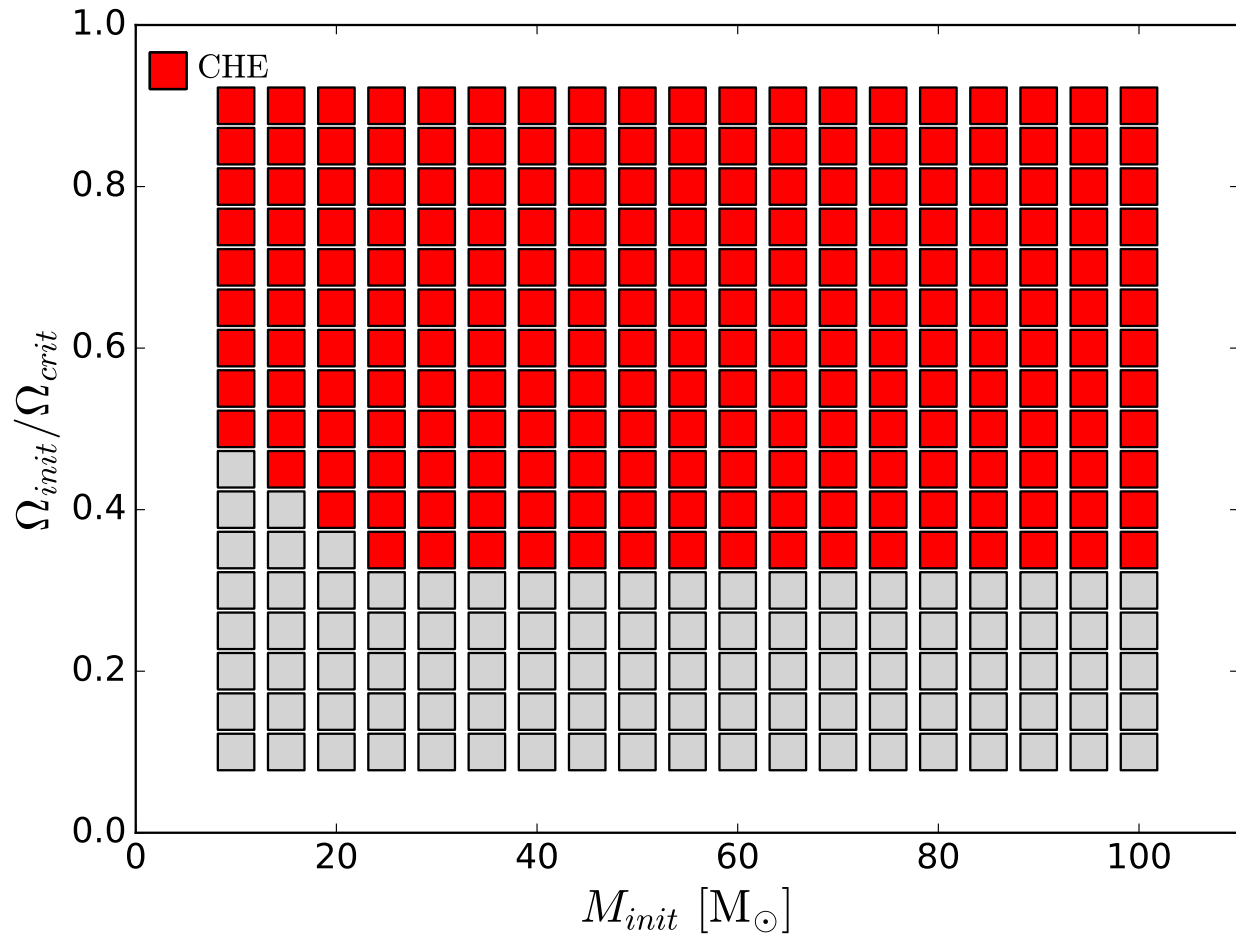


Figure 5.3: Initial velocity as a function of initial masses at ZAMS. Red squares are marked as the systems that have undergone the CHE. Here we define the criterion of the CHE, namely, the difference of helium mass fraction between the surface and center is less than 0.2.

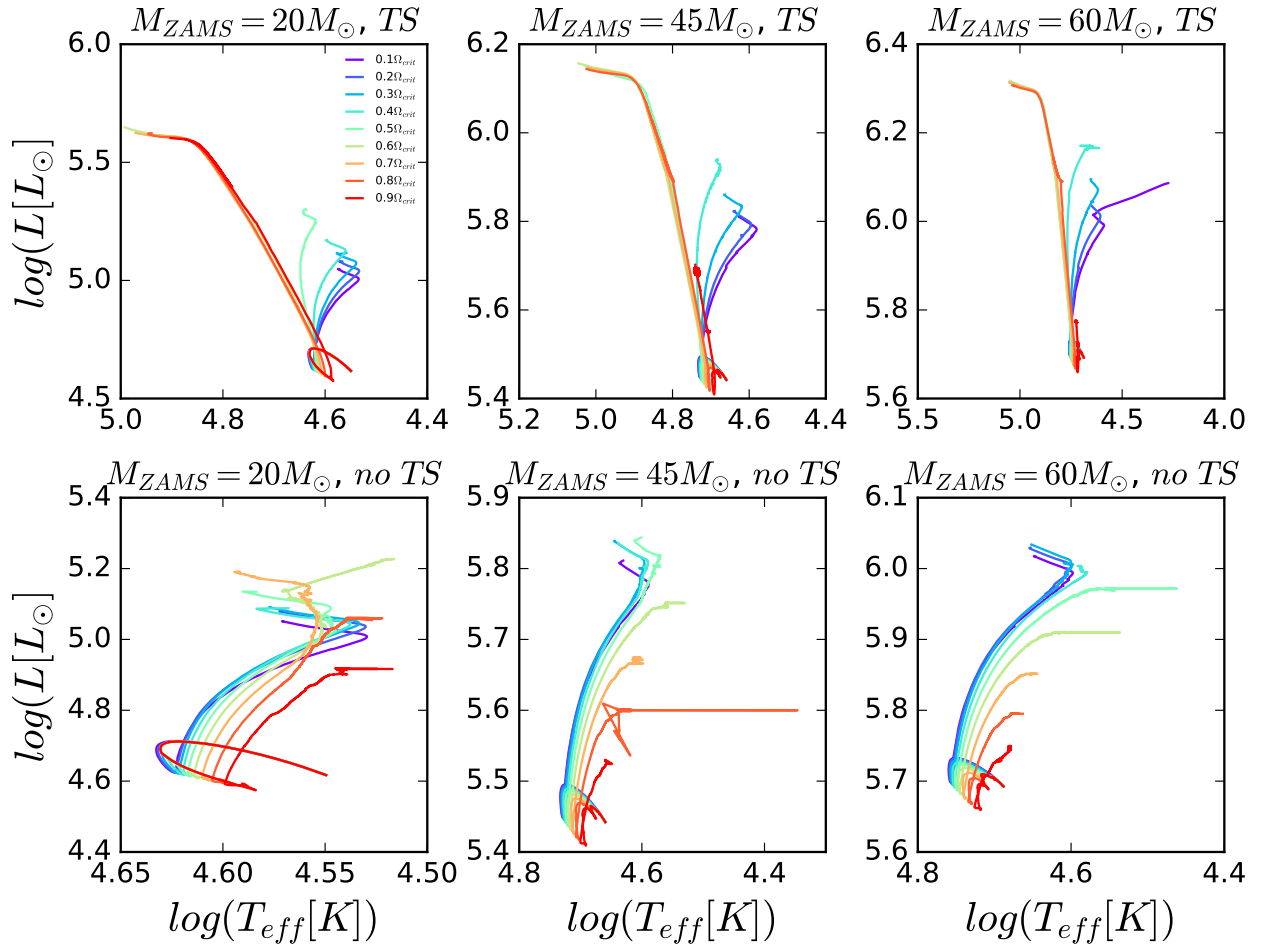


Figure 5.4: Similar to Fig. 5.2, but all of the models are computed with **GENEVA** stellar evolution code.

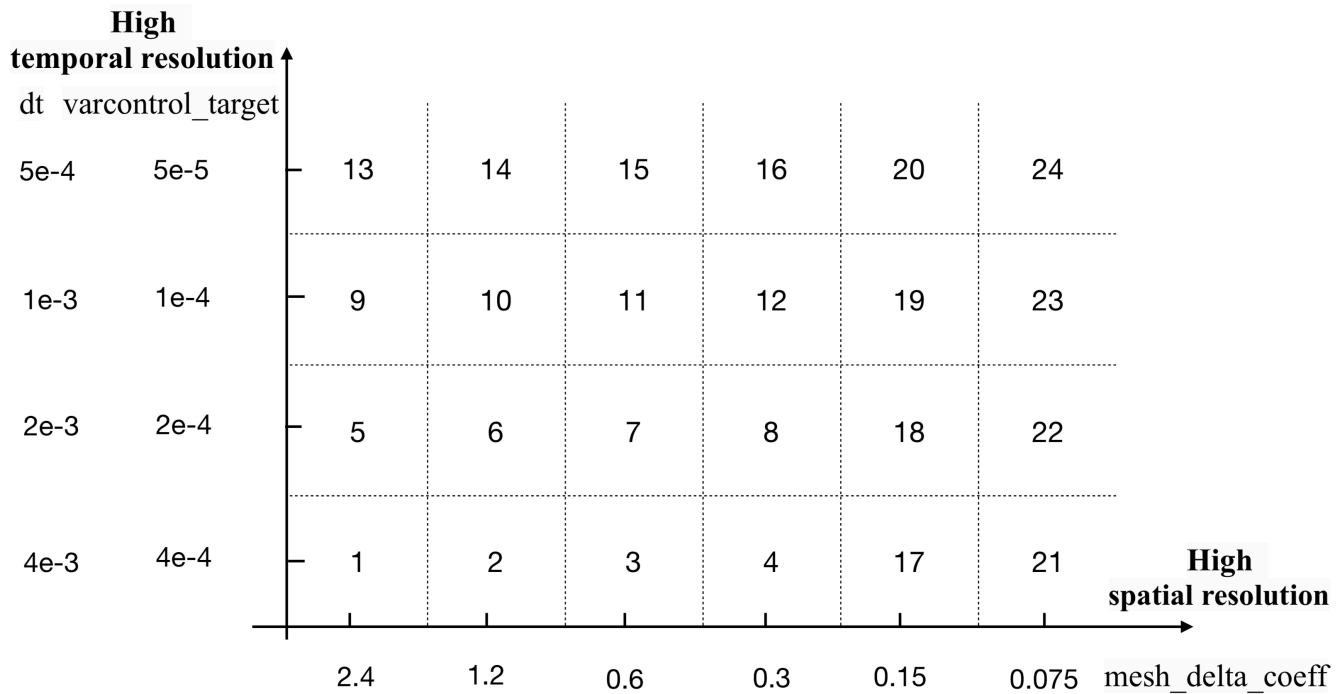
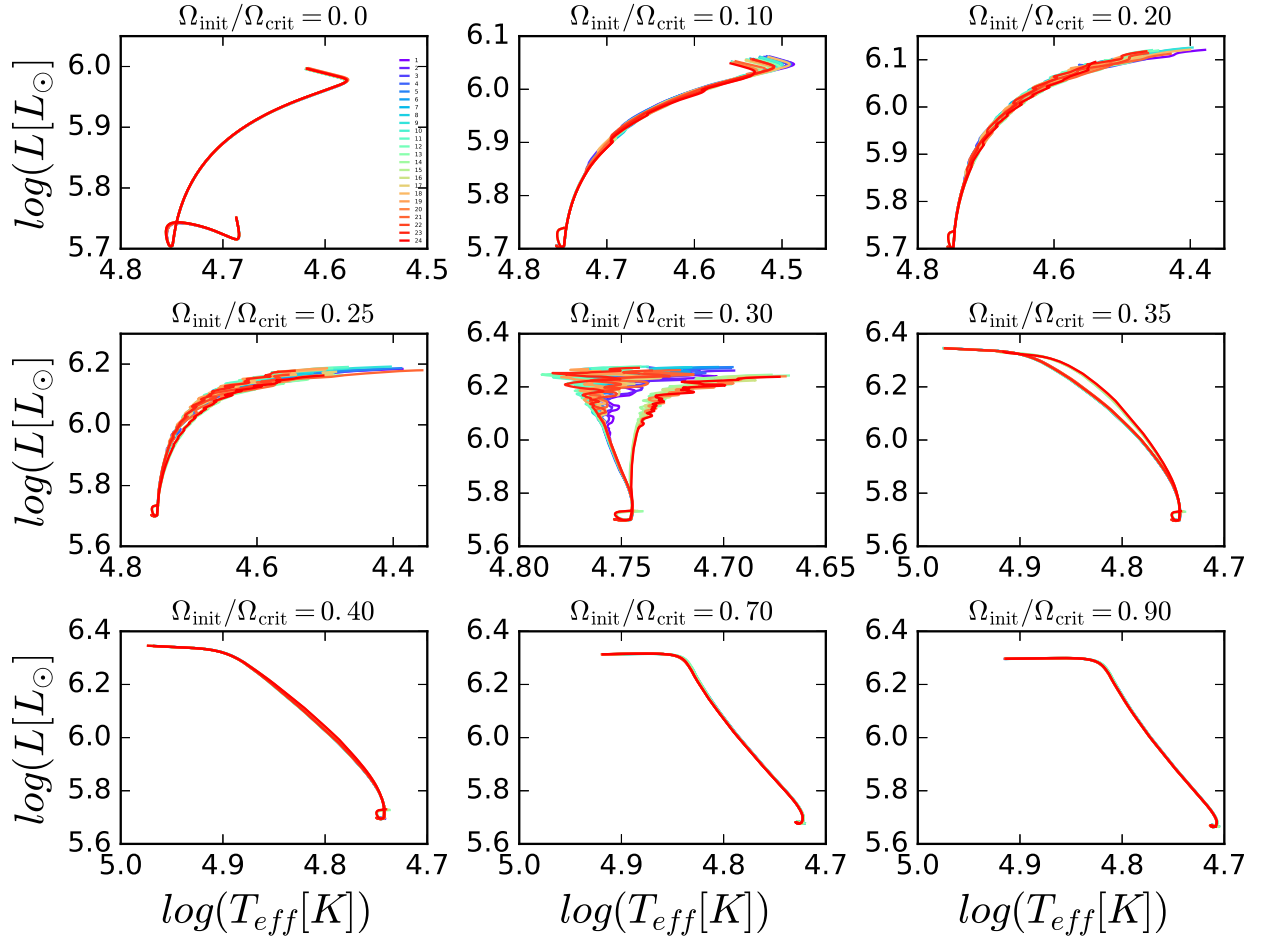


Figure 5.5: Various options for spatial and temporal resolutions. Each number indicates a specific spatial and temporal resolution. We increase spatial resolution by decreasing mesh_delta_coeff (Responsible for a number of grid points, see x axis from 2.4 to 0.075) and max_dq (Max size for cell as fraction of total mass, see x axis from 4e-3 to 1.25e-4). At the same time, we increase temporal resolution by decreasing varcontrol_target (Responsible for timestep adjustment, see y axis from 4e-4 to 1.25e-4) and dt (Reducing dt due to a large change in central hydrogen, helium and carbon, see y axis from 4e-3 to 5e-5).



Chapter 6

Conclusion and Prospect

6.1 Conclusion

During my study, I was working on two different types of BH binaries, i.e., coalescing binary BHs and BH HMXBs. The measured effective inspiral spin parameter χ_{eff} of the former BH binaries is quite low, while the three BH spin measurements in HMXBs show only values near the maximum. My study is focused mainly on the detailed stellar and binary evolution, especially tracking the evolution of angular momentum of the BH progenitor star in BH binaries, by taking into account stellar winds, differential rotation for each stellar component, tidal interaction with its companion, as well as mass transfer (MT) through Roche-lobe overflow of the donor star. More specifically, we systematically studied the origin of the BH spin in these two different BH binaries systems. Furthermore, I have been working on an ongoing project that is related to a detailed comparison of the implementation for chemical mixing and AM transport between two popular stellar evolution codes, namely, **MESA** and **GENEVA** codes. More specifically, we want to understand the minimum rotation required for chemically homogeneous evolution to occur.

6.1.1 The spin of the second-born BH in coalescing binary BHs

Since the first GW event GW150914 (Abbott et al., 2016a) was discovered by the AdLIGO, various double BH formation channels have been proposed, i.e., *common envelope channel*, *chemically homogeneous evolution channel*, and *dynamical formation channel*. In two of these channels, namely the classical isolated binary evolution through the *common envelope channel*, and the massive close evolution through *chemically homogeneous evolution channel*, the immediate progenitor of the binary BH is a close binary system composed of a BH and a helium star.

We focused on this last evolutionary phase and performed detailed stellar structure and binary evolution calculations (Paxton et al., 2011, 2013, 2015, 2018) that take into account mass-loss for helium stars, internal differential rotation, and tidal interactions between the helium and the BH. In the calculation of tides, we calculated the strength of the tides from first principles based on the structure of the helium stars. For the spin of the first-born BH, the

binary star's orbit is rather wide, and tides are not strong enough to synchronize its spin with the orbit. Hence its progenitor evolves almost like a single star throughout its lifetime. We computed the spin of the first-born BH progenitor with different initial conditions, i.e., masses, initial rotation rates at helium stars ZAMS, as well as their different metallicities. Based on the direct core-collapse model (the mass and angular momentum are conserved during the core-collapse), we found that the spin of the first-born BH through the *common envelope channel* is negligible ($a_* \ll 1$). Therefore, the second-born BH's spin dominates the observable effective spin χ_{eff} of double BHs.

As the progenitor of the second-born BH is a helium star, we computed the tidal coefficient E_2 that is based on the structure of the helium star with different initial condition (different helium star masses and metallicities), and then obtained a fitting formula that is useful in the binary evolution community. Due to a large dimensionality of the available initial parameter space of helium star-BH and helium star-NS binaries, it is computationally impractical to cover sufficiently densely the whole available parameter space. Knowing that tides only play a crucial role in close binary systems, we first performed an order-of-magnitude test to identify the part the parameter space where tides are relevant. We argued that tides play a crucial role only when the orbit periods are smaller than 2 days.

After obtaining a qualitative understanding of which physical processes are important for binaries with different initial conditions, as well as a limited part of the parameter space, we then computed grids of detailed calculations of close binaries consisting of a helium star and a BH or NS. Upon core collapse, the helium star produces a BH (the second-born BH in the system) with a spin that can span the entire range from zero to maximally spinning. It was shown that the bimodal distribution of the spin of the second-born BH obtained in recent papers is mainly due to oversimplifying assumptions. We also found an anti-correlation between the merging timescale of the two BHs, T_{merger} and the effective spin χ_{eff} .

The results of currently observed GW events with measurements of M_{chirp} and χ_{eff} can be explained with our detailed binary evolution. We then predicted that, with future improvements to AdLIGO's sensitivity, the sample of merging binary BH systems will show an overdensity of sources with positive but small χ_{eff} originating from lower-mass BH mergers born at low redshift.

In this work, the detailed studies on how the second-born BH can be spun up via tidal interaction have been investigated in detail. We show all of the currently observed GW events can be explained by double BHs through *common envelope channel*. In addition, a full population synthesis calculation (in preparation in Simone et al. 2019) that takes into account the cosmological evolution of star formation rate and metallicity, as well as LIGO selection effects. We find a good agreement between our models and the observed ten O1/O2 AdLIGO observations.

6.1.2 The BH spin of the High-Mass X-Ray Binaries

X-ray binaries (XRBs) have been considered to be ideal astrophysical laboratories for studying one of the most important BHs' properties, namely, spin. BH spins in low-mass X-ray binaries (LMXBs) cover a range of values that can be explained by accretion after BH birth. In contrast, the three High-mass X-ray binaries with spin measurements near the maximum likely have a different origin connected to the BH stellar progenitor.

We explored two possible scenarios to explain the high spins of BHs in the HMXBs, formation in binaries that undergo mass transfer during the main sequence (Case-A MT), alternatively formation in very close binaries undergoing chemically homogeneous evolution (i.e., CHE). We found that the two scenarios are able to produce high-spin BHs if internal angular momentum transport inside the BH progenitor star after its main-sequence evolution is not efficient (i.e., weak coupling between the stellar core and its envelope). The former scenario (i.e., Case-A MT) can not only reproduce consistent results for currently high BH spin, but also provide a good fit for the masses of the two components, as well as the final orbital periods. The other scenario (i.e., CHE) predicts orbital periods that are too large for all three sources. Finally, we predict that the stellar companions of HMXBs formed through the Case-A MT have enhanced nitrogen surface abundances, which can be tested by future observations.

In this work, we found that the angular momentum transport plays a crucial role in understanding the high spins of currently observed three HMXBs.

6.1.3 On the Conditions of Chemically Homogeneous Evolution

As mentioned earlier, CHE has also been proposed as one of the main double BH formation channels. Massive stars at low metallicity tend to have a strong chemical mixing due to fast rotation and hence evolve chemically homogeneously. But the condition for triggering the CHE is unclear. In this work, we explore the CHE with two main physical processes, i.e., Eddington-Sweet circulation and TS dynamo. With different implementation of the Eddington-Sweet circulation, we further compare the threshold for the CHE between the stellar evolution code **MESA** and **GENEVA**. we found the magnetic instability in **GENEVA** code is very efficient in transporting angular momentum and leads to a near solid body rotation during the MS phase as in the **MESA** model.

Finally, from the numerical experiments we can conclude that when we mention models with rotation it is important to specify the physics that has been used to obtain the rotating models. This work is still in preparation.

6.2 Prospect

A global network of interferometers helps scientists pin down the locations of GW sources coming from space. Here I briefly introduce the current operating GW detectors and some others that are currently underway.

Fig. 6.1 shows the network of current ground-based GW detectors. The upgraded LIGO and Virgo, together with GEO600 instrument, started the third observing run “O3” on April 1, 2019. Furthermore, Kamioka Gravitational Wave Detector (KAGRA) in Japan, whose design is similar to Advanced LIGO/Virgo, will be ready to start searching for GWs later in 2019. LIGO-India, which has been approved and is underway, is expected to begin operations in 2024.

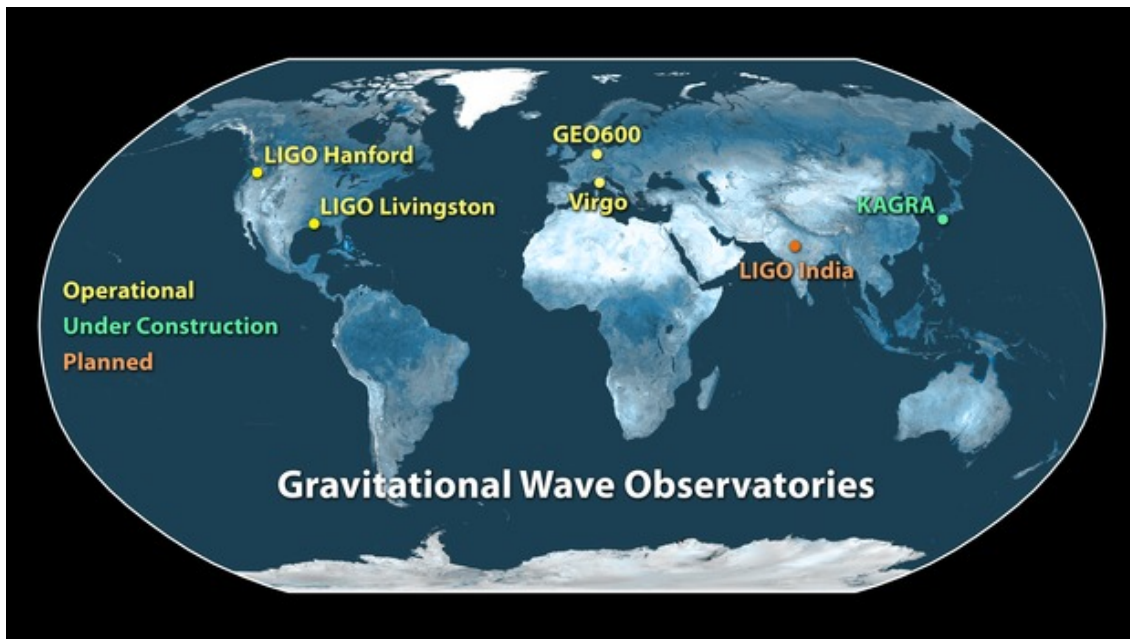


Figure 6.1: Gravitational-Wave Observatories Across the Globe. Credits: <https://www.ligo.caltech.edu>

In addition to ground-based GW detectors, Laser Interferometer Space Antenna (LISA), operates in the low frequency range in Fig. 6.2, between 0.1 mHz and 1 Hz (LIGO’s frequency of 10 Hz to 1000 Hz). It is focused on looking for a much longer wavelength corresponding to objects in wider orbits and heavier than those LIGO’s targets. It would discover include ultra-compact binaries in our Galaxy, supermassive BH merger, and extreme mass ratio inspirals. The LISA is now scheduled to launch in the early 2030s. At the same time, the TianQin Project in China, a proposed space-based GW detector at the frequency of LISA’s sensitivity (0.1 mHz – 1 Hz) consisting of three spacecrafts in Earth orbit, will launch between 2025 and 2030.

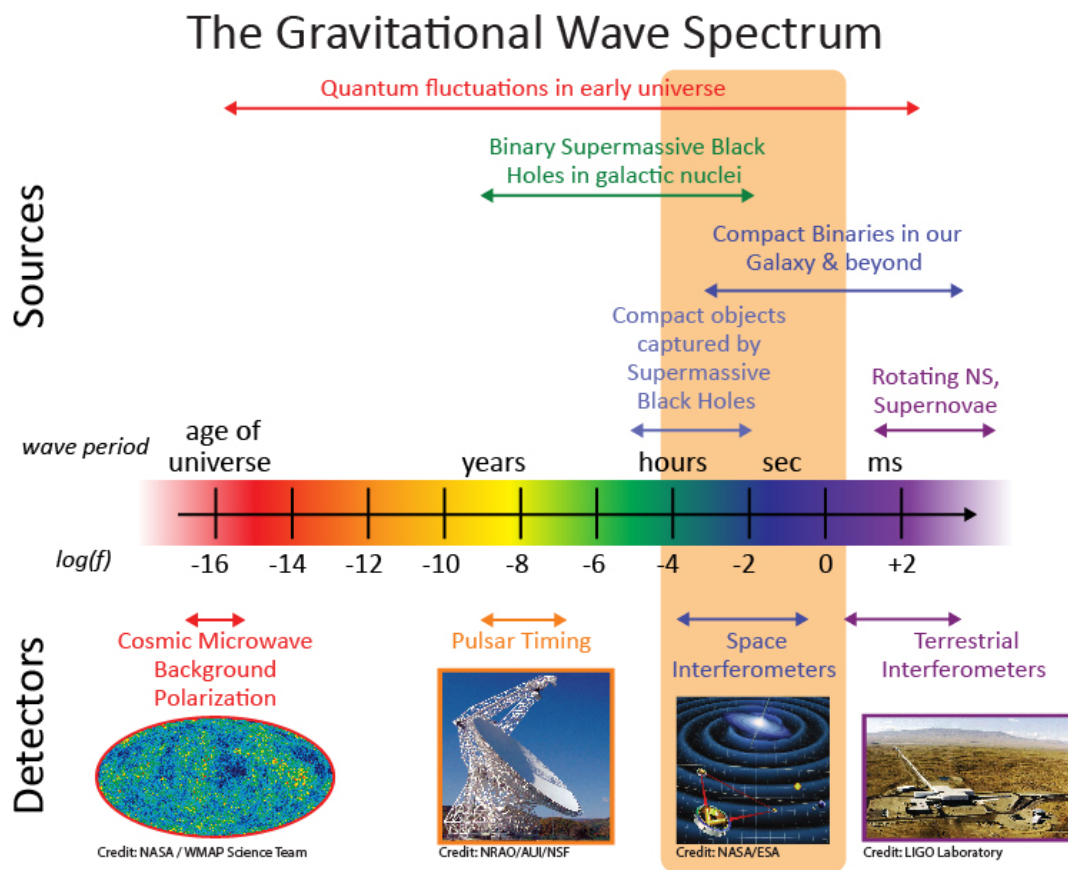


Figure 6.2: Gravitational-Wave spectrum. Credits: <https://lisa.nasa.gov>

Bibliography

- Abbott, B. P., Abbott, R., Abbott, T. D., et al. 2016, *Physical Review Letters*, 116, 061102
- Abbott, B. P., Abbott, R., Abbott, T. D., et al. 2016, *The Astrophysical Journal*, 818, L22
- Abbott, B. P., Abbott, R., Abbott, T. D., et al. 2016, *Physical Review Letters*, 116, 241102
- Abbott, B. P., Abbott, R., Abbott, T. D., et al. 2016, *Physical Review X*, 6, 041015
- Abbott, B. P., Abbott, R., Abbott, T. D., et al. 2016, *Physical Review Letters*, 116, 241103
- Abbott, B. P., Abbott, R., Abbott, T. D., et al. 2016, *The Astrophysical Journal*, 832, L21
- Abbott, B. P., Abbott, R., Abbott, T. D., et al. 2017, *Physical Review Letters*, 119, 161101
- Abbott, B. P., Abbott, R., Abbott, T. D., et al. 2017, *Physical Review Letters*, 119, 141101
- Abbott, B. P., Abbott, R., Abbott, T. D., et al. 2017, *The Astrophysical Journal*, 851, L35
- Abbott, B. P., Abbott, R., Abbott, T. D., et al. 2017, *Physical Review Letters*, 118, 221101
- Ackermann, M., Ajello, M., Albert, A., et al. 2016, *The Astrophysical Journal*, 823, L2
- Aerts, C. 2015, *Astronomische Nachrichten*, 336, 477
- Almeida, L. A., Sana, H., de Mink, S. E., et al. 2015, *The Astrophysical Journal*, 812, 102
- Almeida, L. A., Sana, H., Taylor, W., et al. 2017, *Astronomy and Astrophysics*, 598, A84
- Böhm-Vitense, E. 1958, *Zeitschrift für Astrophysik*, 46, 108
- Bailyn, C. D., Jain, R. K., Coppi, P., & Orosz, J. A. 1998, *The Astrophysical Journal*, 499, 367
- Baker, N., & Kippenhahn, R. 1959, *Zeitschrift für Astrophysik*, 48, 140
- Balbus, S. A., & Hawley, J. F. 1998, *Reviews of Modern Physics*, 70, 1

- Bardeen, J. M., Press, W. H., & Teukolsky, S. A. 1972, *The Astrophysical Journal*, 178, 347
- Barr, P., White, N. E., & Page, C. G. 1985, *Monthly Notices of the Royal Astronomical Society*, 216, 65P
- Batta, A., Ramirez-Ruiz, E., & Fryer, C. 2017, *The Astrophysical Journal*, 846, L15
- Belczynski, K., Klencki, J., Meynet, G., et al. 2017, arXiv e-prints, arXiv:1706.07053
- Belczynski, K., Bulik, T., Fryer, C. L., et al. 2010, *The Astrophysical Journal*, 714, 1217
- Belczynski, K., Holz, D. E., Bulik, T., & O'Shaughnessy, R. 2016, *Nature*, 534, 512
- Belczynski, K., Wiktorowicz, G., Fryer, C. L., Holz, D. E., & Kalogera, V. 2012, *The Astrophysical Journal*, 757, 91
- Blandford, R. D., & Znajek, R. L. 1977, *Monthly Notices of the Royal Astronomical Society*, 179, 433
- Blum, J. L., Miller, J. M., Fabian, A. C., et al. 2009, *The Astrophysical Journal*, 706, 60
- Bondi, H., & Hoyle, F. 1944, *Monthly Notices of the Royal Astronomical Society*, 104, 273
- Braithwaite, J. 2006, *Astronomy and Astrophysics*, 449, 451
- Brott, I., de Mink, S. E., Cantiello, M., et al. 2011, *Astronomy and Astrophysics*, 530, A115
- Brown, G. E., Lee, C.-H., Wijers, R. A. M. J., et al. 2000, *New Astronomy*, 5, 191
- Brown, G. E., & Weingartner, J. C. 1994, *The Astrophysical Journal*, 436, 843
- Bulik, T., Belczynski, K., & Prestwich, A. 2011, *The Astrophysical Journal*, 730, 140
- Caballero-Nieves, S. M., Gies, D. R., Bolton, C. T., et al. 2009, *The Astrophysical Journal*, 701, 1895
- Cantiello, M., Yoon, S.-C., Langer, N., & Livio, M. 2007, *Astronomy and Astrophysics*, 465, L29
- Cantrell, A. G., Bailyn, C. D., Orosz, J. A., et al. 2010, *The Astrophysical Journal*, 710, 1127
- Carroll, B. W., & Ostlie, D. A. 2006, *Institute for Mathematics and Its Applications*,
- Casares, J., & Jonker, P. G. 2014, *Space Science Reviews*, 183, 223
- Casares, J., Jonker, P. G., & Israelian, G. 2017, *Handbook of Supernovae*, 1499
- Chaboyer, B., & Zahn, J.-P. 1992, *Astronomy and Astrophysics*, 253, 173

- Claret, A. 2004, *Astronomy and Astrophysics*, 424, 919
- Claret, A., & Cunha, N. C. S. 1997, *Astronomy and Astrophysics*, 318, 187
- Connaughton, V., Burns, E., Goldstein, A., et al. 2016, *The Astrophysical Journal*, 826, L6
- Crowther, P. A. 2007, *Annual Review of Astronomy and Astrophysics*, 45, 177
- D’Orazio, D. J., & Loeb, A. 2018, *Physical Review D*, 97, 083008
- Darwin, G. H. 1879, *Proceedings of the Royal Society of London Series I*, 29, 168
- Davis, S. W., Blaes, O. M., Hubeny, I., & Turner, N. J. 2005, *The Astrophysical Journal*, 621, 372
- Davis, S. W., & Hubeny, I. 2006, *The Astrophysical Journal Supplement Series*, 164, 530
- de Mink, S. E., Cantiello, M., Langer, N., et al. 2009, *Astronomy and Astrophysics*, 497, 243
- de Mink, S. E., & Mandel, I. 2016, *Monthly Notices of the Royal Astronomical Society*, 460, 3545
- Deheuvels, S., Ballot, J., Beck, P. G., et al. 2015, *Astronomy and Astrophysics*, 580, A96
- Denissenkov, P. A. 2010, *The Astrophysical Journal*, 723, 563
- Detmers, R. G., Langer, N., Podsiadlowski, P., & Izzard, R. G. 2008, *Astronomy and Astrophysics*, 484, 831
- Eggenberger, P., Deheuvels, S., Miglio, A., et al. 2019, *Astronomy and Astrophysics*, 621, A66
- Eggenberger, P., Maeder, A., & Meynet, G. 2005, *Astronomy and Astrophysics*, 440, L9
- Eggenberger, P., Meynet, G., Maeder, A., et al. 2008, *Astrophysics and Space Science*, 316, 43
- Eggenberger, P., Montalbán, J., & Miglio, A. 2012, *Astronomy and Astrophysics*, 544, L4
- Eggleton, P. P. 1983, *The Astrophysical Journal*, 268, 368
- Ekström, S., Georgy, C., Eggenberger, P., et al. 2012, *Astronomy and Astrophysics*, 537, A146
- Eldridge, J. J., & Vink, J. S. 2006, *Astronomy and Astrophysics*, 452, 295
- Eldridge, J. J., Izzard, R. G., & Tout, C. A. 2008, *Monthly Notices of the Royal Astronomical Society*, 384, 1109
- Endal, A. S., & Sofia, S. 1978, *The Astrophysical Journal*, 220, 279
- Evans, C., Hunter, I., Smartt, S., et al. 2008, *The Messenger*, 131, 25

- Fabian, A. C., Rees, M. J., Stella, L., & White, N. E. 1989, *Monthly Notices of the Royal Astronomical Society*, 238, 729
- Fabian, A. C., Zoghbi, A., Wilkins, D., et al. 2012, *Monthly Notices of the Royal Astronomical Society*, 419, 116
- Farr, W. M., Stevenson, S., Miller, M. C., et al. 2017, *Nature*, 548, 426
- Filippenko, A. V. 1997, *Annual Review of Astronomy and Astrophysics*, 35, 309
- Fragos, T., & McClintock, J. E. 2015, *The Astrophysical Journal*, 800, 17
- Fragos, T., Willems, B., Kalogera, V., et al. 2009, *The Astrophysical Journal*, 697, 1057
- Fryer, C. L. 1999, *The Astrophysical Journal*, 522, 413
- Fuller, J., Cantiello, M., Lecoanet, D., & Quataert, E. 2015, *The Astrophysical Journal*, 810, 101
- Gabriel, M., Noels, A., Montalbán, J., & Miglio, A. 2014, *Astronomy and Astrophysics*, 569, A63
- Gaia Collaboration, Brown, A. G. A., Vallenari, A., et al. 2018, *Astronomy and Astrophysics*, 616, A1
- Gehan, C., Mosser, B., Michel, E., Samadi, R., & Kallinger, T. 2018, *Astronomy and Astrophysics*, 616, A24
- Georgy, C., Ekström, S., Meynet, G., et al. 2012, *Astronomy and Astrophysics*, 542, A29
- Georgy, C., Meynet, G., & Maeder, A. 2011, *Astronomy and Astrophysics*, 527, A52
- Georgy, C., Meynet, G., Walder, R., Folini, D., & Maeder, A. 2009, *Astronomy and Astrophysics*, 502, 611
- Glebbeek, E., Gaburov, E., de Mink, S. E., Pols, O. R., & Portegies Zwart, S. F. 2009, *Astronomy and Astrophysics*, 497, 255
- Gou, L., McClintock, J. E., Liu, J., et al. 2009, *The Astrophysical Journal*, 701, 1076
- Gou, L., McClintock, J. E., Reid, M. J., et al. 2011, *The Astrophysical Journal*, 742, 85
- Gou, L., McClintock, J. E., Remillard, R. A., et al. 2014, *The Astrophysical Journal*, 790, 29
- Gou, L., McClintock, J. E., Steiner, J. F., et al. 2010, *The Astrophysical Journal*, 718, L122
- Greene, J., Bailyn, C. D., & Orosz, J. A. 2001, *The Astrophysical Journal*, 554, 1290
- Grevesse, N., Noels, A., & Sauval, A. J. 1996, *Cosmic Abundances*, 99, 117

- Hamann, W.-R., Koesterke, L., & Wessolowski, U. 1995, *Astronomy and Astrophysics*, 299, 151
- Heger, A., Fryer, C. L., Woosley, S. E., Langer, N., & Hartmann, D. H. 2003, *The Astrophysical Journal*, 591, 288
- Heger, A., & Langer, N. 2000, *The Astrophysical Journal*, 544, 1016
- Heger, A., & Langer, N. 1998, *Astronomy and Astrophysics*, 334, 210
- Heger, A., Langer, N., & Woosley, S. E. 2000, *The Astrophysical Journal*, 528, 368
- Heger, A., Woosley, S. E., & Spruit, H. C. 2005, *The Astrophysical Journal*, 626, 350
- Hiemstra, B., Méndez, M., Done, C., et al. 2011, *Monthly Notices of the Royal Astronomical Society*, 411, 137
- Hotokezaka, K., & Piran, T. 2017, arXiv e-prints, arXiv:1707.08978
- Hotokezaka, K., & Piran, T. 2017, *The Astrophysical Journal*, 842, 111
- Howe, R. 2009, *Living Reviews in Solar Physics*, 6, 1
- Hulse, R. A., & Taylor, J. H. 1975, *The Astrophysical Journal*, 195, L51
- Hunter, J. D. 2007, *Computing in Science and Engineering*, 9, 90
- Hurley, J. R., Tout, C. A., & Pols, O. R. 2002, *Monthly Notices of the Royal Astronomical Society*, 329, 897
- Hut, P. 1981, *Astronomy and Astrophysics*, 99, 126
- Inayoshi, K., Hirai, R., Kinugawa, T., & Hotokezaka, K. 2017, *Monthly Notices of the Royal Astronomical Society*, 468, 5020
- Ivanova, N., Justham, S., Chen, X., et al. 2013, *Astronomy and Astrophysics Review*, 21, 59
- Ivanova, N. 2015, *Ecology of Blue Straggler Stars*, 179
- Izzard, R. G., Ramirez-Ruiz, E., & Tout, C. A. 2004, *Monthly Notices of the Royal Astronomical Society*, 348, 1215
- Janka, H.-T., Langanke, K., Marek, A., Martínez-Pinedo, G., & Müller, B. 2007, *Physics Reports*, 442, 38
- Janssen, G. H., Stappers, B. W., Kramer, M., et al. 2008, *Astronomy and Astrophysics*, 490, 753
- Kiminki, D. C., Kobulnicky, H. A., Vargas Álvarez, C. A., Alexander, M. J., & Lundquist, M. J. 2015, *The Astrophysical Journal*, 811, 85

- Kippenhahn, R. 1974, *Late Stages of Stellar Evolution*, 66, 20
- Kippenhahn, R., & Weigert, A. 1967, *Zeitschrift fur Astrophysik*, 65, 251
- Kobulnicky, H. A., Kiminki, D. C., Lundquist, M. J., et al. 2014, *The Astrophysical Journal Supplement Series*, 213, 34
- Kocsis, B., & Levin, J. 2012, *Physical Review D*, 85, 123005
- Kolb, U., & Ritter, H. 1990, *Astronomy and Astrophysics*, 236, 385
- Kushnir, D., Zaldarriaga, M., Kollmeier, J. A., & Waldman, R. 2017, *Monthly Notices of the Royal Astronomical Society*, 467, 2146
- Kushnir, D., Zaldarriaga, M., Kollmeier, J. A., & Waldman, R. 2016, *Monthly Notices of the Royal Astronomical Society*, 462, 844
- Langer, N. 2012, *Annual Review of Astronomy and Astrophysics*, 50, 107
- Langer, N. 1998, *Astronomy and Astrophysics*, 329, 551
- Langer, N. 1997, *Luminous Blue Variables: Massive Stars in Transition*, 120, 83
- Langer, N., Fricke, K. J., & Sugimoto, D. 1983, *Astronomy and Astrophysics*, 126, 207
- Langer, N., Cantiello, M., Yoon, S.-C., et al. 2008, *Massive Stars as Cosmic Engines*, 250, 167
- Lau, H. H. B., Izzard, R. G., & Schneider, F. R. N. 2014, *Astronomy and Astrophysics*, 570, A125
- Laycock, S. G. T., Maccarone, T. J., & Christodoulou, D. M. 2015, *Monthly Notices of the Royal Astronomical Society*, 452, L31
- Li, L.-X., Zimmerman, E. R., Narayan, R., & McClintock, J. E. 2005, *The Astrophysical Journal Supplement Series*, 157, 335
- Li, X.-D. 2015, *New Astronomy Reviews*, 64, 1
- LIGO Scientific Collaboration, Aasi, J., Abbott, B. P., et al. 2015, *Classical and Quantum Gravity*, 32, 074001
- Liu, J., McClintock, J. E., Narayan, R., Davis, S. W., & Orosz, J. A. 2010, *The Astrophysical Journal*, 719, L109
- Liu, J., McClintock, J. E., Narayan, R., Davis, S. W., & Orosz, J. A. 2008, *The Astrophysical Journal*, 679, L37

- Loeb, A. 2016, *The Astrophysical Journal*, 819, L21
- Maeder, A. 1987, *Astronomy and Astrophysics*, 178, 159
- Maeder, A., & Meynet, G. 2005, *Astronomy and Astrophysics*, 440, 1041
- Maeder, A., & Meynet, G. 2001, *Astronomy and Astrophysics*, 373, 555
- Maeder, A., & Meynet, G. 2000, *Astronomy and Astrophysics*, 361, 159
- Maeder, A., & Meynet, G. 2012, *Reviews of Modern Physics*, 84, 25
- Maeder, A., & Meynet, G. 2000, *Annual Review of Astronomy and Astrophysics*, 38, 143
- Maeder, A., & Zahn, J.-P. 1998, *Astronomy and Astrophysics*, 334, 1000
- Mandel, I., & de Mink, S. E. 2016, *Monthly Notices of the Royal Astronomical Society*, 458, 2634
- Mandel, I., & Farmer, A. 2018, arXiv e-prints, arXiv:1806.05820
- Marchant, P., Langer, N., Podsiadlowski, P., et al. 2017, *Astronomy and Astrophysics*, 604, A55
- Marchant, P., Langer, N., Podsiadlowski, P., Tauris, T. M., & Moriya, T. J. 2016, *Astronomy and Astrophysics*, 588, A50
- McClintock, J. E. 2006, *Bulletin of the American Astronomical Society*, 38, 33.01
- McClintock, J. E., Narayan, R., & Steiner, J. F. 2014, *Space Science Reviews*, 183, 295
- McClintock, J. E., Shafee, R., Narayan, R., et al. 2006, *The Astrophysical Journal*, 652, 518
- Mestel, L. 1953, *Monthly Notices of the Royal Astronomical Society*, 113, 716
- Mestel, L. 1952, *Monthly Notices of the Royal Astronomical Society*, 112, 598
- Miller, J. M., Reynolds, C. S., Fabian, A. C., Miniutti, G., & Gallo, L. C. 2009, *The Astrophysical Journal*, 697, 900
- Miller, M. C., & Lauburg, V. M. 2009, *The Astrophysical Journal*, 692, 917
- Miller, M. C., & Miller, J. M. 2015, *Physics Reports*, 548, 1
- Moe, M., & Di Stefano, R. 2017, *The Astrophysical Journal Supplement Series*, 230, 15

- Moreno Méndez, E. 2011, *Monthly Notices of the Royal Astronomical Society*, 413, 183
- Moreno Méndez, E., & Cantiello, M. 2016, *New Astronomy*, 44, 58
- Novikov, I. D., & Thorne, K. S. 1973, *Black Holes (Les Astres Occlus)*, 343
- Nugis, T., & Lamers, H. J. G. L. M. 2000, *Astronomy and Astrophysics*, 360, 227
- O’Leary, R. M., Kocsis, B., & Loeb, A. 2009, *Monthly Notices of the Royal Astronomical Society*, 395, 2127
- Ogilvie, G. I. 2014, *Annual Review of Astronomy and Astrophysics*, 52, 171
- Orosz, J. A. 2003, *A Massive Star Odyssey: From Main Sequence to Supernova*, 212, 365
- Orosz, J. A., McClintock, J. E., Aufdenberg, J. P., et al. 2011, *The Astrophysical Journal*, 742, 84
- Orosz, J. A., McClintock, J. E., Bailyn, C. D., et al. 2007, *The Astronomer’s Telegram*, 977,
- Orosz, J. A., Steeghs, D., McClintock, J. E., et al. 2009, *The Astrophysical Journal*, 697, 573
- Orosz, J. A., Steiner, J. F., McClintock, J. E., et al. 2011, *The Astrophysical Journal*, 730, 75
- Paxton, B., Bildsten, L., Dotter, A., et al. 2011, *The Astrophysical Journal Supplement Series*, 192, 3
- Paxton, B., Cantiello, M., Arras, P., et al. 2013, *The Astrophysical Journal Supplement Series*, 208, 4
- Paxton, B., Marchant, P., Schwab, J., et al. 2015, *The Astrophysical Journal Supplement Series*, 220, 15
- Paxton, B., Schwab, J., Bauer, E. B., et al. 2018, *The Astrophysical Journal Supplement Series*, 234, 34
- Peimbert, M., Luridiana, V., & Peimbert, A. 2007, *The Astrophysical Journal*, 666, 636
- Penna, R. F., McKinney, J. C., Narayan, R., et al. 2010, *Monthly Notices of the Royal Astronomical Society*, 408, 752
- Perna, R., Lazzati, D., & Giacomazzo, B. 2016, *The Astrophysical Journal*, 821, L18
- Peters, P. C. 1964, *Physical Review*, 136, 1224
- Petrovic, J., Langer, N., & van der Hucht, K. A. 2005, *Astronomy and Astrophysics*, 435, 1013
- Petrovich, C., & Antonini, F. 2017, *The Astrophysical Journal*, 846, 146
- Pfahl, E., Rappaport, S., Podsiadlowski, P., & Spruit, H. 2002, *The Astrophysical Journal*, 574, 364

- Phinney, E. S. 1991, *The Astrophysical Journal*, 380, L17
- Pinsonneault, M. H., Kawaler, S. D., Sofia, S., & Demarque, P. 1989, *The Astrophysical Journal*, 338, 424
- Planck Collaboration, Ade, P. A. R., Aghanim, N., et al. 2016, *Astronomy and Astrophysics*, 594, A13
- Podsiadlowski, P., Rappaport, S., & Han, Z. 2003, *Monthly Notices of the Royal Astronomical Society*, 341, 385
- Qin, Y., Fragos, T., Meynet, G., et al. 2018, *Astronomy and Astrophysics*, 616, A28
- Qin, Y., Marchant, P., Fragos, T., Meynet, G., & Kalogera, V. 2019, *The Astrophysical Journal*, 870, L18
- Rasio, F. A., Tout, C. A., Lubow, S. H., & Livio, M. 1996, *The Astrophysical Journal*, 470, 1187
- Reis, R. C., Fabian, A. C., Reynolds, C. S., et al. 2012, *The Astrophysical Journal*, 745, 93
- Reis, R. C., Miller, J. M., & Fabian, A. C. 2009, *Monthly Notices of the Royal Astronomical Society*, 395, L52
- Reis, R. C., Miller, J. M., Fabian, A. C., et al. 2011, *Monthly Notices of the Royal Astronomical Society*, 410, 2497
- Reis, R. C., Miller, J. M., Reynolds, M. T., Fabian, A. C., & Walton, D. J. 2012, *The Astrophysical Journal*, 751, 34
- Remillard, R. A., & McClintock, J. E. 2006, *Annual Review of Astronomy and Astrophysics*, 44, 49
- Repetto, S., Davies, M. B., & Sigurdsson, S. 2012, *Monthly Notices of the Royal Astronomical Society*, 425, 2799
- Repetto, S., & Nelemans, G. 2015, *Monthly Notices of the Royal Astronomical Society*, 453, 3341
- Reynolds, C. S. 2014, *Space Science Reviews*, 183, 277
- Reynolds, C. S., & Fabian, A. C. 2008, *The Astrophysical Journal*, 675, 1048
- Ritter, H. 1988, *Astronomy and Astrophysics*, 202, 93
- Rodriguez, C. L., Haster, C.-J., Chatterjee, S., Kalogera, V., & Rasio, F. A. 2016, *The Astrophysical Journal*, 824, L8
- Rodriguez, C. L., Morscher, M., Pattabiraman, B., et al. 2015, *Physical Review Letters*, 115, 051101
- Rodriguez, C. L., Zevin, M., Pankow, C., Kalogera, V., & Rasio, F. A. 2016, *The Astrophysical Journal*, 832, L2
- Sørensen, M., Fragos, T., Steiner, J. F., et al. 2017, *Astronomy and Astrophysics*, 597, A12

- Sana, H., de Mink, S. E., de Koter, A., et al. 2012, *Science*, 337, 444
- Savchenko, V., Ferrigno, C., Mereghetti, S., et al. 2016, *The Astrophysical Journal*, 820, L36
- Schröder, S. L., Batta, A., & Ramirez-Ruiz, E. 2018, *The Astrophysical Journal*, 862, L3
- Shafee, R., McClintock, J. E., Narayan, R., et al. 2006, *The Astrophysical Journal*, 636, L113
- Shafee, R., McKinney, J. C., Narayan, R., et al. 2008, *The Astrophysical Journal*, 687, L25
- Siess, L., Izzard, R. G., Davis, P. J., & Deschamps, R. 2013, *Astronomy and Astrophysics*, 550, A100
- Sigurdsson, S., & Hernquist, L. 1993, *Nature*, 364, 423
- Soberman, G. E., Phinney, E. S., & van den Heuvel, E. P. J. 1997, *Astronomy and Astrophysics*, 327, 620
- Song, H. F., Maeder, A., Meynet, G., et al. 2013, *Astronomy and Astrophysics*, 556, A100
- Song, H. F., Meynet, G., Maeder, A., Ekström, S., & Eggenberger, P. 2016, *Astronomy and Astrophysics*, 585, A120
- Song, H. F., Meynet, G., Maeder, A., et al. 2018, *Astronomy and Astrophysics*, 609, A3
- Spruit, H. C. 2002, *Astronomy and Astrophysics*, 381, 923
- Spruit, H. C. 1999, *Astronomy and Astrophysics*, 349, 189
- Steeghs, D., McClintock, J. E., Parsons, S. G., et al. 2013, *The Astrophysical Journal*, 768, 185
- Steffen, M. 1990, *Astronomy and Astrophysics*, 239, 443
- Steiner, J. F., McClintock, J. E., & Reid, M. J. 2012, *The Astrophysical Journal*, 745, L7
- Steiner, J. F., Reis, R. C., Fabian, A. C., et al. 2012, *Monthly Notices of the Royal Astronomical Society*, 427, 2552
- Steiner, J. F., Reis, R. C., McClintock, J. E., et al. 2011, *Monthly Notices of the Royal Astronomical Society*, 416, 941
- Suijs, M. P. L., Langer, N., Poelarends, A.-J., et al. 2008, *Astronomy and Astrophysics*, 481, L87
- Sukhbold, T., Ertl, T., Woosley, S. E., Brown, J. M., & Janka, H.-T. 2016, *The Astrophysical Journal*, 821, 38
- Tassoul, M., & Tassoul, J.-L. 1984, *The Astrophysical Journal*, 279, 384

- Tauris, T. M., & van den Heuvel, E. P. J. 2006, Compact stellar X-ray sources, 39, 623
- Taylor, J. H., & Weisberg, J. M. 1982, The Astrophysical Journal, 253, 908
- The LIGO Scientific Collaboration, the Virgo Collaboration, Abbott, B. P., et al. 2018, arXiv e-prints, arXiv:1811.12907
- Thorne, K. S. 1974, The Astrophysical Journal, 191, 507
- Toledano, O., Moreno, E., Koenigsberger, G., Detmers, R., & Langer, N. 2007, Astronomy and Astrophysics, 461, 1057
- Tutukov, A., & Yungelson, L. 1973, Nauchnye Informatsii, 27, 70
- Tutukov, A. V., & Cherepashchuk, A. M. 2017, Astronomy Reports, 61, 833
- Tutukov, A. V., & Yungelson, L. R. 1993, Monthly Notices of the Royal Astronomical Society, 260, 675
- Valsecchi, F., Glebbeek, E., Farr, W. M., et al. 2010, Nature, 468, 77
- van den Heuvel, E. P. J., Portegies Zwart, S. F., & de Mink, S. E. 2017, Monthly Notices of the Royal Astronomical Society, 471, 4256
- van den Heuvel, E. P. J., & Yoon, S.-C. 2007, Astrophysics and Space Science, 311, 177
- van den Heuvel, E. P. J. 2019, arXiv e-prints, arXiv:1901.06939
- van Oijen, J. G. J. 1989, Astronomy and Astrophysics, 217, 115
- van Paradijs, J. 1998, NATO Advanced Science Institutes (ASI) Series C, 515, 279
- Vink, J. S., de Koter, A., & Lamers, H. J. G. L. M. 2001, Astronomy and Astrophysics, 369, 574
- Vink, J. S., Muijres, L. E., Anthonisse, B., et al. 2011, Astronomy and Astrophysics, 531, A132
- von Zeipel, H. 1924, Monthly Notices of the Royal Astronomical Society, 84, 665
- von Zeipel, H. 1924, Monthly Notices of the Royal Astronomical Society, 84, 684
- Willems, B., Henninger, M., Levin, T., et al. 2005, The Astrophysical Journal, 625, 324
- Wong, T.-W., Valsecchi, F., Ansari, A., et al. 2014, The Astrophysical Journal, 790, 119
- Wong, T.-W., Valsecchi, F., Fragos, T., & Kalogera, V. 2012, The Astrophysical Journal, 747, 111

- Woosley, S. E. 2016, *The Astrophysical Journal*, 824, L10
- Woosley, S. E. 1993, *Bulletin of the American Astronomical Society*, 25, 55.05
- Woosley, S. E., & Bloom, J. S. 2006, *Annual Review of Astronomy and Astrophysics*, 44, 507
- Wu, X.-F., Hou, S.-J., & Lei, W.-H. 2013, *The Astrophysical Journal*, 767, L36
- Yoon, S.-C., Dierks, A., & Langer, N. 2012, *Astronomy and Astrophysics*, 542, A113
- Yoon, S.-C., Langer, N., & Norman, C. 2006, *Astronomy and Astrophysics*, 460, 199
- Yoon, S.-C., Woosley, S. E., & Langer, N. 2010, *The Astrophysical Journal*, 725, 940
- Zahid, H. J., Dima, G. I., Kudritzki, R.-P., et al. 2014, *The Astrophysical Journal*, 791, 130
- Zahn, J. P. 1970, *Astronomy and Astrophysics*, 4, 452
- Zahn, J.-P. 1992, *Astronomy and Astrophysics*, 265, 115
- Zahn, J.-P. 1977, *Astronomy and Astrophysics*, 57, 383
- Zahn, J.-P. 1975, *Astronomy and Astrophysics*, 41, 329
- Zahn, J.-P., Brun, A. S., & Mathis, S. 2007, *Astronomy and Astrophysics*, 474, 145
- Zaldarriaga, M., Kushnir, D., & Kollmeier, J. A. 2018, *Monthly Notices of the Royal Astronomical Society*, 473, 4174
- Zhang, S. N., Cui, W., & Chen, W. 1997, *The Astrophysical Journal*, 482, L155
- Zhu, Y., Davis, S. W., Narayan, R., et al. 2012, *Monthly Notices of the Royal Astronomical Society*, 424, 2504
- Ziółkowski, J. 2014, *Monthly Notices of the Royal Astronomical Society*, 440, L61
- Zou, W. Z., Hobbs, G., Wang, N., et al. 2005, *Monthly Notices of the Royal Astronomical Society*, 362, 1189